ABSTRACT

STUDY OF STRESS IN MICROELECTRONIC MATERIALS BY PHOTOELASTICITY

by
Hancheng Liang

The study of stress is playing an important role in microelectronic technology. In comparison with other techniques, the photoelasticity technique has the advantages of having high spatial resolution and high sensitivity. It can be used in qualitative observation in real-time and quantitative determination of stress distribution in the microelectronic materials and devices.

This dissertation presents a systematic study of photoelastic stress analysis in microelectronic materials and devices, ranged from theoretical study to practical system setup, from measurement methods to their applications. At first, based on the detailed survey on the piezo-optic properties of the crystals used in microelectronics, we apply the stress-optic law of engineering mechanics to study the stress in crystals, such as silicon, gallium arsenide, and diamond. We, for the first time, derive the relationship between the stress ellipsoid and the refractive index ellipsoid, and, derive the matrix forms of piezo-optic coefficient tensor for several commonly used coordinates. These theoretical results have laid a firm ground for the photoelastic stress analysis of microelectronic materials and devices. Second, based on exclusive experiments, we develop several effective methods of photoelastic analysis to determine the stress state in the samples. Some of them are successfully borrowed from the classic photoelastic mechanics, such as the Semarmont compensation which is used to determine the decimal fringe of the isochromatic line, and the shearing stress difference method which is used to separate two principal stresses and obtain the stress distribution of a sample. We also provide our origination to the photoelastic techniques, such as the three-direction observation method which is used to

abstract the principal stresses from the secondary principal stresses; the Fourier analysis method and the intensity analysis method, both of which are especially suitable for precisely and automatically determining the principal stress distribution in a large area. Combining computer and digital image processing techniques with photoelastic techniques, we set up a photoelastic measurement system, which has the capability of qualitative observation of the photoelastic patterns and quantitative measurement of the stress distribution.

We apply the photoelasticity principles and methods to investigate the stress state in microelectronic materials, including developing a series of feasible methods to measure the stress distribution of the microelectronic materials and devices, investigating the mechanisms of stress induction and stress change. For example, we investigate the stress distribution of a synthetic diamond substrate, study the stress induced during the typical impurity diffusion processes for manufacturing power diodes, and analyze the stress induced in the thin film/substrate structures. We also develop some models to explain the measurement results and provide theoretical discussions of the results.

STUDY OF STRESS IN MICROELECTRONIC MATERIALS BY PHOTOELASTICITY

by
Hancheng Liang

A Dissertation
Submitted to the Faculty of
New Jersey Institute of Technology
in Partial Fulfillment of the Requirements for the Degree of
Doctor of Philosophy

Department of Electrical and Computer Engineering

January 1996

APPROVAL PAGE

STUDY OF STRESS IN MICROELECTRONIC MATERIALS BY PHOTOELASTICITY

Hancheng Liang

Dr. Ken K. Chin, Dissertation Adviser Professor of Physics, NJIT	Date
Dr. John C. Hensel, Committee Member Distinguished Research Professor of Physics, NJIT	Date
Dr. Robert B. Marcus, Committee Member Research Professor of Electrical and Computer Engineering, NJIT	Date
Dr. William N. Carr, Committee Member Professor of Electrical and Computer Engineering, NJIT Professor of Physics, NJIT	Date
Dr. Yun-Qing Shi, Committee Member Associate Professor of Electrical and Computer Engineering, NJIT	Date

BIOGRAPHICAL SKETCH

Author: Hancheng Liang

Degree: Doctor of Philosophy in Electrical Engineering

Date: January 1996

Education:

- Doctor of Philosophy in Electrical Engineering
  New Jersey Institute of Technology, Newark, New Jersey, 1996
- Master of Science in Applied Physics
  South China Institute of Technology, Guangzhou, P. R. China, 1985
- Diploma of Electrical Engineering
  South China Institute of Technology, Guangzhou, P. R. China, 1980

Major: Electrical Engineering

Presentations and Publications:

Hancheng Liang, Yongxiong Pan, Shounan Zhao, Ganming Qin, and K. Ken Chin, "Two-Dimensional State of Stress in a Silicon Wafer", *J. Appl. Phys.* **71** (1992): 2863-2870.

Hancheng Liang, Shounan Zhao, and K. Ken Chin, "A New Method of Determining the Stress State in Microelectronic Materials", *Measurement Science and Technology*, **6** (1995): 1-4.

Hancheng Liang, Shounan Zhao, Ganming Qin, and K. Ken Chin, "Thin Film-induced Stress in Substrate/Thin Film Structure", *Procedings of the Fourth International Conference on Solid-State and Integrated-Circuit Technology*, Publishing House of the Electronics Industry, Beijing (1995): 272-274.

Hancheng Liang, Andrei Vescan, Erhard Kohn, and K. Ken Chin, "Measurement of Stress in a Synthetic Diamond Substrate by Using Photoelastic Method", *The Sixth European Conference on Diamond, Diamond-Like and Related Materials*, Barcelona, Spain, 1995. Also accepted for publication in *Diamond and Related Materials*.

To my beloved family

ACKNOWLEDGMENT

The author wishes to express his sincere gratitude to his advisor, Dr. Ken K. Chin, for his encouragement, guidance and help throughout the course of this work.

Thanks are given to Dr. John C. Hensel for his friendly and technical support for my research work.

Special thanks go to professors Ken K. Chin, John. C. Hensel, Dr. Robert B. Marcus, Dr. William N. Carr, and Dr. Yun-Qing Shi for serving as members of the committee. Thanks should be given to them for advice and discussions about my research projects.

The author appreciates the help and suggestions from Prof. Shounan Zhao, Prof. Erhard Kohn, Prof. Yuan Yan, Prof. Guanhua Feng, and Mr. Ganming Qin.

TABLE OF CONTENTS

TABLE OF CONTENTS
(Continued)

TABLE OF CONTENTS
(Continued)

LIST OF FIGURES

LIST OF FIGURES
(Continued)

LIST OF TABLES

CHAPTER 1

INTRODUCTION

In this chapter we introduce some background information, including the significance of stress study in microelectronics and the methods of measuring stress in microelectronic materials and device structures. We will briefly review the previous research on photoelastic stress analysis. Finally, we will introduce the research work we have done about the subject.

1.1 Background Information

1.1.1 Importance of Stress Study in Microelectronics

The study of stress plays an important role in microelectronic technology. The presence of stress will affect the performance and reliability of the device. For example, the mechanical stress in deposited thin films has been found to be the main cause of the problems of film cracking, delamination or void formation. Even some of the more subtle problems, such as junction leakage and parametric shifts, may be partially caused by stress [1]. The stress generated during the stripe fabrication of a InGaAsP ridge-waveguide laser changes the waveguide properties of the laser [2]. With stress, the current-voltage characteristic in a Schottky diode deteriorates due to the change of both the shunt resistance and the effective Richardson constant of the Schottky diode [3]. Semiconductor structures containing strain layers have formed the basis of a new class of semiconducting materials and devices, but the presence of strain may also lead to a greater likelihood of dislocation nucleation and, therefore, to an accelerated degradation of the devices [4].

Almost every step of microelectronic processing, such as grinding, polishing, epitaxy, oxidation, metallization, diffusion, ion-implantation, and packaging, may

introduce a drastic change of the stress state in a device or integrated circuit. Stress in a semiconductor crystal may come from the damage of surface during crystal surface processing, or may originate from the internal stress due to dislocations, excess vacancies, and impurities with different atomic radii from the semiconductor crystal. Stress also arises from the thermal gradient during crystal growth. Vapor disposed thin film on a semiconductor wafer will induce strong internal stress during deposition [5]. In brief, there are various sources of stress. Stress is closely related with the defects in the crystal. The stress and the defects in crystal always interact with each other. We regard the stress field in microelectronic materials as somewhat continuous and changeable *generalized defect*. It is an important subject in microelectronic technology to investigate the mechanisms of origin, evolution and elimination of stress and to understand the effect of stress on the performance of material and device as well as to control the stress in device structures.

1.1.2 A Survey of Stress Measurement Methods

Stress and strain may be determined by surveying the change of crystal lattice, by measuring the curvature of a wafer sample, or by studying the birefringence. A commonly used method of determining change of the crystal lattice constant is *X*-ray diffraction [6]. The presence of strain in a semiconductor crystal will result in the change of the lattice constant of the crystal. Bragg law describes the relation between the Bragg angle and the distance of two neighbor crystal planes [7],

$$n\lambda = 2d\sin\theta \tag{1.1}$$

where θ is the Bragg angle, λ the wavelength of *X*-ray, n the diffraction order, and d the distance of the neighbor crystal planes. With stress, the change of d in crystal will result in the change of θ. Once d is determined, the strain e in this region of the crystal can be determined by

$$e = \frac{d_{stress-free} - d_{stressed}}{d_{stress-free}} \tag{1.2}$$

Then based on Hooke's law we can calculate the stress.

The stress state in a wafer can also be estimated by measuring the wafer curvature [8]. For example, in the case of a thin film/substrate structure, the internal biaxial stress in the thin films causes the wafers to bow. The stress-induced radius of curvature R is related with the strain e resulted from the lattice-mismatch by the relation:

$$\frac{1}{R} = \frac{6(1-\nu_s)}{(1-\nu_f)} \frac{E_f}{E_s} \frac{t_f}{t_s^2} e \tag{1.3}$$

and independently measured by reflection of a laser beam from the wafer surface. In (1.3) the subscripts s and f refer to the substrate and the thin film, respectively. E is the Young's modulus, ν the Poisson's ratio, and t the thickness. Thus, from the measured radius of curvature, we can calculate the lattice strain by using (1.3).

The radius of curvature of a thin film/substrate structure can also be determined by the X-ray diffraction method [9]. If θ_n is the Bragg angle at point n, θ_{n+1} is the Bragg angle at point $n+1$, and Δs is the distance between points n and $n+1$, the radius of curvature between points n and $n+1$ is given as

$$R = \frac{\Delta s}{\theta_{n+1} - \theta_n} \tag{1.4}$$

The method based on measuring the change of crystal lattice, although complicated and involving expensive X-ray diffraction equipment, only provides the lattice constants of a local region of the materials, and cannot offer the information of stress distribution in microelectronic materials under measurement. On the other hand, the method based on measuring the wafer curvature by using an X-ray or a laser beam, although being widely used, is limited to the measurement of average stress of a wafer.

Photoelasticity is an optical method of stress analysis, which based upon the phenomenon of *double refraction*, or *birefringence* [10]. When a polarized light passes through an unstressed sample, it will suffer a reduction in velocity according to the refractive index, but otherwise remain unchanged. If a stressed sample is placed in the polarized light field, within the sample, the light is resolved into two components which

oscillate in planes at right angles to one another (see Figure 1.1). Further, the two components of light travel at slightly different speed in the two planes, depending on the stress conditions. Therefore, when they emerge from the sample, there is a difference in phase between the two waves that is proportional to the thickness of the sample traversed by the light. The lag of one component behind the other is the *birefringence phase difference* δ (or measured in terms of length, the *optical path difference*). For normal incidence on a sample subjected to plane stress within the elastic limit, the transmission of light obeys the following *stress-optic law* which forms the basis of photoelastic stress analysis: *the difference of the two principal stresses is proportional to the birefringence phase difference induced by the presence of the stress.* By deducing the birefringence phase difference it is possible to evaluate the stress within the sample. The advantages of the photoelasticity method owe to the fact that it is non-destructive, convenient, and accurate. It can offer real-time qualitative observation as well as quantitative determination of stress distribution in a sample.

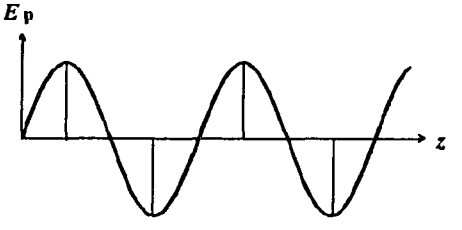

(a)Before entering the sample

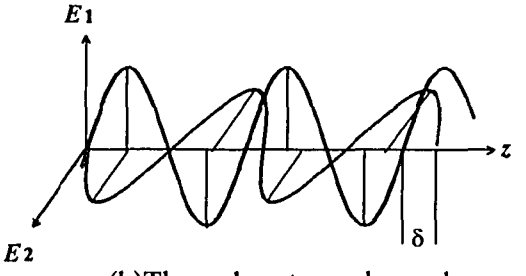

(b)Through a stressed sample

Figure 1.1 Propagation of linearly polarized light.

1.2 A Review on the Study of Stress by Using Photoelasticity

1.2.1 Previous Work

The phenomenon of artificial-birefringence was discovered in 1816 by Sir David Brewster. During the nineteenth century, the underlying theory was well developed by investigators such as Neumann, Maxwell, Wertheim, and other noted physicists who formulated the concept that the optical retardation producing the photoelastic effect is proportional to the difference of the principal stresses existing in an isotropic material. By the middle of the twentieth century, since the laser, electronic, and computer techniques greatly promoted the development of photoelasticity technology, photoelastic experiments entered their mature stage. Photoelasticity technology permeated various fields of application, including microelectronics. Stress study of silicon crystals using photoelasticity was started in 1956 by W. L. Bond and J. Andrus [11]. They first observed the photoelastic pattern of a stress field around single edge dislocation in silicon single crystal by using infrared polarized light. In 1959, J. Hornstra and P. Penning studied the birefringence phenomenon during rapidly cooling of a silicon crystal [12]. They determined the relative stress-optic coefficient by balancing the internal stress with an externally applied force on the sample. In 1971, R. O. DeNicola and R. N. Tauber applied the infrared photoelasticity method to study the effect of growth conditions of Czochralski-grown silicon crystal on the stress and dislocation density [13]. They also applied the Tardy compensation method to describe the distribution of stress in the sample. In 1977, Shin Takasu *et alii* first applied the photoelasticity method to observe the stress state in device processing [14], and hence made a significant progress in application of photoelasticity technique in microelectronics. In 1980, H. Kotate and Shin Takasu first semi-quantitatively measured and calculated the stress in silicon devices [15]. They calculated the piezo-optic coefficients in some coordinate systems for observation. By counting the isochromatic lines, they estimated the

stress distribution in a mounted silicon pellet. The first order of the isochromatic lines they observed corresponds to a discernible stress of 8.5×10^7 dyn/cm^2. In 1989, T. Iwaki and T. Koizumi first proposed the general stress-optic law in a single crystal plate under plane stress state, and discussed the possibility of its application to photoelastically anisotropic crystals [16].

In the past decade, besides silicon, photoelasticity technology also was utilized to study the stress of various materials, especially, III-V semiconductor materials. For example, Albert Feldman and Roy M. Waxler studied the piezobirefringence of GaAs due to strain-dependent lattice effects [17]. They measured the piezobirefringence of GaAs over the wavelength range 3.5-10.6μm. Aloke K. Dutta, *et al.*, simulated the dark-field image of a diametrically compressed GaAs disk, and compared it with that obtained from their experiment [18]. Sadao Adachi and Kunishige Oe studied the internal strain and photoelastic effect in $Ga_{1-x}Al_xAs/GaAs$ and $In_{1-x}Ga_xAs_yP_{1-y}/InP$ materials [19]. They presented the wavelength dispersion of the photoelastic coefficients in these materials.

After years of our study of the stress using photoelasticity, we have solved a series of fundamental problems encountered in photoelastic stress analysis of microelectronic materials [20][21]. In the similitude of isotropic mediums, we utilized a relative stress-optic coefficient to relate the birefringence phase difference with the principal stress difference in a crystal material. For some specific geometrical configurations, we obtained the values of the relative stress-optic coefficient for silicon wafer samples. We, for the first time, applied the Senarmont compensation method to determine the fractional fringe order of isochromatic lines of silicon wafer samples, and applied the nail-compression method to determine the tensile or compressive stress state at the boundary of a sample. A measurement system was established by employing a silicon vidicon as detector, which was of a spatial resolution of $100\mu m$. The technique was applied to study the stress in semiconductor materials and devices, such as Czochralski-grown silicon single crystal ingots, oxidized silicon wafers, and ion-implanted silicon wafers [22][23].

1.2.2 New Problems Solved in This Dissertation

However, some problems remain to be solved in the photoelastic stress analysis of microelectronic materials. The first problem is that in previous work the photoelastic anisotropy of crystals has not been fully taken into account. We ignored that for crystal materials, the axes of the principal stress ellipsoid do not coincide with the principal axes of the refractive index ellipsoid. Generally, the stress-optic law for isotropic material cannot be directly applied to study the stress. Suitable forms of the stress-optic law must be developed to extend to the range of the anisotropic properties of crystals. On the other hand, in previous work, when we employed the Senarmont compensation method to measure the fractional order fringe of photoelastic patterns [21][23], we had to achieve the complete extinction of transmitted light by rotating the analyzer and measuring the azimuth of the transmitting axis of the analyzer. Evidently, while it is feasible to measure a single point of a sample, it is impractical to measure the stress distribution of a sample with large area, since it is inconvenient to repeat rotating the polarizer to achieve extinction at every point of the sample. Therefore, the second problem is to seek some effective methods of measuring the fractional order fringe over the entire wafer sample. Besides, when a light beam transmits through the stressed sample, only the stresses perpendicular to the incident beam cause an optical effect, while the stresses in the incident direction do not. In measuring the stress in a wafer sample, we usually employed the flank-observation scheme. The stresses directly measured are in fact not the principal stresses, but the secondary principal stresses normal to the incident direction. Consequently, the third problem is to develop a method to abstract the principal stresses from the secondary principal stresses. Furthermore, our previous experiments represented the best result of $100\mu m$ of spatial resolution in stress distribution, and about $10^8 dyn/cm^2$ of minimum detectable stress for a silicon wafer sample. To improve both the spatial resolution and the detection sensitivity, it is necessary to develop a measurement system with the help of the image sensing and computer techniques.

1.3 Scope of Our Research Work

The purpose of our research work is to find solutions to the problems mentioned in Section 1.2.2. The research project includes: (1) investigating the anisotropic property of the photoelastic effect for some semiconductor crystals, and in different coordinates deriving the suitable forms of stress-optic law for these anisotropic materials; (2) exploring some effective methods to measure the photoelastic parameters, and determining the direction of principal stresses from secondary stresses, calculate the distribution of the principal stresses in a sample; (3) establishing a photoelastic system, which includes the capability of qualitative observation of the photoelastic patterns and quantitative measurement of the stress distribution; (4) applying above research results to study the stress state in microelectronic materials.

1.3.1 Stress-Optic Law of Photoelastically Anisotropic Materials

We know that for the crystals of diamond structure or zincblende structure, the physical properties of the crystals described by a fourth-rank tensor are not isotropic, such as piezo-optic coefficient tensor, which relates a second-rank stress tensor with a second-rank dielectric impermeability tensor. A crystal will lose its original lattice symmetry when stressed, and hence exhibits mechanical anisotropic property. For crystals, the principal axes of the stress ellipsoid do not coincide with the principal axes of the refractive index ellipsoid. Therefore, the crystals with diamond or zincblende structures, when suffered from internal or external stress, will become photoelastically anisotropic. The stress-optic law for isotropic materials is no longer valid for such crystal materials.

In this dissertation, the photoelastic anisotropy of cubic crystals is investigated. The matrix forms of the piezo-optic coefficient tensor for various coordinate configurations are derived. The relationship of the principal axes of the stress ellipsoid and the principal axes of the refractive index ellipsoid for arbitrary crystallographic directions and observation

direction is studied. Suitable forms of stress-optic law for anisotropic materials are derived in several commonly used coordinate configurations.

1.3.2 Methods of Photoelastic Stress Analysis

The purpose of stress analysis is to obtain the stress distribution in a sample from given boundary conditions. In order to apply stress-optic law to calculate principal stress difference, one needs to know the photoelastic parameters (*i.e.*, the birefringence phase difference δ and the birefringence angle ϕ, which will be defined in Chapter 2).

In traditional photoelastic experiments, a common method of determining these two parameters is to analyze the isochromatic lines and the isoclinic lines of the photoelastic patterns. However, for most situations in the application of microelectronic materials, since the order of the isochromatic line is less than one, which corresponds to the stress less than $10^8 dyn/cm^2$, it is necessary to determine these two parameters by analyzing the fractional order of isochromatic lines. Senarmont compensation is a useful method of determining the birefringence phase difference with fractional order of isochromatic line. However, since Senarmont compensation method is a point-by-point method, it can measure only one point of the sample at a time. In this dissertation, we discuss the Fourier analysis method and the intensity analysis method we developed, which are suitable for measuring the whole area of the sample at one time. We present the principles and applications of these two methods. We also discuss the three-direction observation method that is used to calculate the principal stresses from the secondary principal stresses, and the shearing stress difference method which is utilized to separate two principal stresses and to determine the distribution of two principal stresses.

1.3.3 Stress-Measurement System

Our previous experiments exhibited the best result of $100\mu m$ of spatial resolution in stress distribution, and about $10^8 dyn/cm^2$ of minimum detectable stress for a silicon wafer

sample. The fact the continuous reduction of the dimension of microelectronic devices requires better spatial resolution of measurement, and better sensitivity of measuring stress state of device structures.

A photoelastic stress measurement system typically consists of light source, polarizer, analyzer, quarter waveplates, and detector. In our experiment, the detector is either a photomultiplier or a *CCD* camera. With the help of the image sensing and computer techniques, we develop an automatic measurement system, in which a *CCD* camera is employed as detecting device. Owing to its characteristic of high dynamic range and low noise, both very weak and strong signals can be detected in a single frame, which is important in improving the detecting sensitivity of the system. And fast digitization rate makes it possible to observe the stress patterns in real time, which is of significance in the application of microelectronic production.

1.3.4 Study of Stress in Microelectronic Materials

As the examples of application, we illustrate stress measurement in some microelectronic materials with photoelasticity principles and methods. Experiments include studying the stress distribution in a diamond substrate, studying stress in thin film/substrate structures, and studying diffusion-related stress in silicon wafers.

The residual stress in a synthetic diamond substrate is analyzed by using the automatic data acquisition and analysis system. The digital image processing techniques are applied to improve the quality of the sensed images, to reduce noise and to determine the boundary of the measured samples. The intensity analysis method and the Fourier analysis method is used to determine the photoelastic parameters; and the shearing stress difference method is applied to calculate the two-dimensional stress distribution in the sample. The thin film on a semiconductor substrate and its discontinuity will give rise to a stress field in the substrate. The stress introduced in substrate/thin film structures, including the stress induced by oxide film, the stress induced by discontinuity of thin film,

and the stress induced by metal films, is investigated with the Senarmont compensation method and the Fourier analysis method. Finally, we discuss the study of stress distributions in silicon wafers after various diffusion processes. We discuss our experimental results and present our mathematics models for explaining the results.

CHAPTER 2

PHOTOELASTIC EFFECT IN CUBIC CRYSTALS

In order to apply the photoelasticity method to study the stress in microelectronic materials, it is required to perceive the form of stress-optic law of these photoelastically anisotropic materials. In this chapter, the phenomenon of *birefringence* produced by stress (photoelastic effect) is studied. The anisotropic property of photoelastic effect for crystals with cubic symmetry is investigated. The relationship between the principal axes of the stress ellipsoid and those of the refractive index ellipsoid is analyzed. For some commonly used coordinate configurations, matrix forms of the piezo-optic coefficient are derived, and analytical expressions of the stress-optic law in various coordinate configurations are obtained.

2.1 Birefringence

2.1.1 Monochromatic Plane Waves in Crystals

In a transparent and non-magnetic medium, if there is no free charge, the fundamental equations of the electromagnetic field, *i.e.*, the differential form of *Maxwell's equations* can be written as [24]

$$\nabla \times \boldsymbol{H} = \frac{\partial \boldsymbol{D}}{\partial t}$$

$$\nabla \times \boldsymbol{E} = -\frac{\partial \boldsymbol{B}}{\partial t}$$

$$\nabla \cdot \boldsymbol{H} = 0$$

$$\nabla \cdot \boldsymbol{D} = 0 \qquad (2.1)$$

where $\boldsymbol{E}$ is the electric field intensity, $\boldsymbol{D}$ the electric flux density, and $\boldsymbol{H}$ the magnetic field intensity, $\boldsymbol{B}$ the magnetic flux density. From the first two equations of (2.1), yields

$$\nabla \times \nabla \times \boldsymbol{E} = -\nabla \times \frac{\partial \boldsymbol{B}}{\partial t} = -\mu \frac{\partial}{\partial t}(\nabla \times \boldsymbol{H}) = -\mu \frac{\partial^2 \boldsymbol{D}}{\partial t^2} \tag{2.2}$$

where the *constitutive relation* $\boldsymbol{B}=\mu\boldsymbol{H}$ is utilized. From the vector identity

$$\nabla \times \nabla \times \boldsymbol{E} = \nabla(\nabla \cdot \boldsymbol{E}) - \nabla^2 \boldsymbol{E} \tag{2.3}$$

Eq.(2.2) may be rewritten as

$$\nabla(\nabla \cdot \boldsymbol{E}) - \nabla^2 \boldsymbol{E} = -\mu \frac{\partial^2 \boldsymbol{D}}{\partial t^2} \tag{2.4}$$

which is recognized as the *wave equation*.

We wish to examine the properties of plane waves traveling through a crystal. We therefore try as a solution to the wave equation (2.4) and the Maxwell equations (2.1):

$$\begin{aligned} \boldsymbol{E} &= \boldsymbol{E}_0 \exp[i(\omega t - \boldsymbol{k} \cdot \boldsymbol{r})] \\ \boldsymbol{D} &= \boldsymbol{D}_0 \exp[i(\omega t - \boldsymbol{k} \cdot \boldsymbol{r})] \\ \boldsymbol{H} &= \boldsymbol{H}_0 \exp[i(\omega t - \boldsymbol{k} \cdot \boldsymbol{r})] \\ \boldsymbol{B} &= \boldsymbol{B}_0 \exp[i(\omega t - \boldsymbol{k} \cdot \boldsymbol{r})] \end{aligned} \tag{2.5}$$

where $\boldsymbol{E}_0$, $\boldsymbol{D}_0$, $\boldsymbol{H}_0$, and $\boldsymbol{B}_0$ are constant vectors, $\boldsymbol{k}$ is a wave vector normal to the *equiphase planes*, and $[i(\omega t - \boldsymbol{k} \cdot \boldsymbol{r})]$ is the phase of the monochromatic plane wave. By substituting the plane wave solutions (2.5) into Maxwell's equations (2.1), we have

$$\begin{aligned} \omega \boldsymbol{D} &= -\boldsymbol{k} \times \boldsymbol{H} \\ \omega \boldsymbol{B} &= \boldsymbol{k} \times \boldsymbol{E} \\ \boldsymbol{k} \cdot \boldsymbol{D} &= 0 \\ \boldsymbol{k} \cdot \boldsymbol{H} &= 0 \end{aligned} \tag{2.6}$$

By inspecting Eqs.(2.6), we can reach the following conclusions: (*a*) In an isotropic medium, with $\boldsymbol{D}=\varepsilon_0\varepsilon\boldsymbol{E}$, the three vectors ($\boldsymbol{k}$, $\boldsymbol{E}$, and $\boldsymbol{H}$) are orthogonal with each other, as shown in Figure 2.1. The electric and magnetic vectors ($\boldsymbol{E}$, and $\boldsymbol{H}$) of the plane wave, propagating along the wave normal line direction $\boldsymbol{k}$, are perpendicular to the vector $\boldsymbol{k}$. (*b*) In an anisotropic crystal, in general, since the relative dielectric constant is a second-rank tensor, or $D_i=\varepsilon_0\varepsilon_{ij}E_j$, the directions of $\boldsymbol{E}$ and $\boldsymbol{D}$ are not identical. From the first equation and the last two equations of (2.6), it can be seen that the three vectors $\boldsymbol{D}$, $\boldsymbol{H}$, and $\boldsymbol{k}$ are

perpendicular to each other, as shown in Figure 2.2. The electric oscillation vector of the plane wave with the wave vector k is D instead of E.

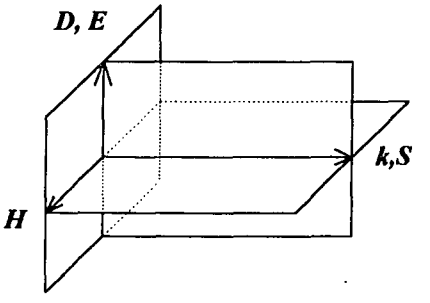

Figure 2.1 Vector relation for a monochromatic plane wave in an isotropic medium.

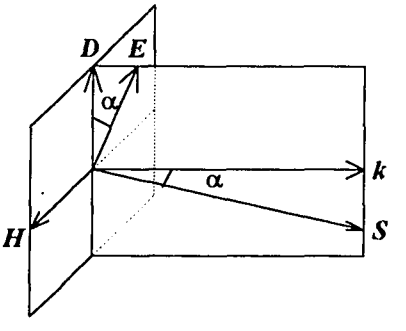

Figure 2.2 Relationship between vectors for a monochromatic plane wave in an anisotropic crystal.

The Poynting vector S is defined as

$$S = E \times H \tag{2.7}$$

This indicates the vectors E, H, and S constitute another orthogonal group, as shown in Figure 2.2. All of the vectors D, E, k, and S locate within the same plane perpendicular to the vector H. Since the directions of E and D are in general not identical, the directions of S and k do not coincide with each other.

2.1.2 A General Description of Birefringence Effect

The plane wave solution (2.5) leads to

$$\nabla (\nabla \cdot \boldsymbol{E}) = -\boldsymbol{k} (\boldsymbol{k} \cdot \boldsymbol{E}) \tag{2.8}$$

$$\nabla^2 \boldsymbol{E} = \nabla \cdot (\nabla \boldsymbol{E}) = -i\,\boldsymbol{k} \cdot (-i\,\boldsymbol{k}\,\boldsymbol{E}) = -\boldsymbol{k} \cdot (\boldsymbol{k}\,\boldsymbol{E}) = -k^2\,\boldsymbol{E} \tag{2.9}$$

$$\frac{\partial^2 \boldsymbol{D}}{\partial t^2} = -\omega^2 \boldsymbol{D} \tag{2.10}$$

By substituting Eqs(2.8)~(2.10) into the wave equation (2.4), we have

$$\mu\omega^2 \boldsymbol{D} = k^2\,\boldsymbol{E} - \boldsymbol{k} (\boldsymbol{k} \cdot \boldsymbol{E}) \tag{2.11}$$

By introducing a unit wave vector $\boldsymbol{K}$

$$\boldsymbol{K} = \frac{\boldsymbol{k}}{k} \tag{2.12}$$

and using the relation

$$k = \frac{2\pi}{\lambda} = \frac{n\omega}{c} \tag{2.13}$$

where λ is the wavelength of the monochromatic plane wave, n the refractive index, Eq.(2.11) can be rewritten as

$$\mu c \boldsymbol{D} = n^2 [\boldsymbol{E} - \boldsymbol{K}(\boldsymbol{E} \cdot \boldsymbol{K})] \tag{2.14}$$

We now assume that $\boldsymbol{D}$ and $\boldsymbol{E}$ are connected by the permittivity tensor. When referred to the principal axes of the permittivity tensor, so that

$$D_i = \varepsilon_0 \varepsilon_i E_i = \varepsilon_0 n_i^2 E_i \quad (i=1, 2, 3) \tag{2.15}$$

where ε_0 is the permittivity of a vacuum, and ε_i (i=1,2,3) the principal values of the relative permittivity tensor of the medium, Eq.(2.14) becomes

$$n_i^2 E_i = n^2 [E_i - K_i (\boldsymbol{E} \cdot \boldsymbol{K})] \quad (i=1, 2, 3) \tag{2.16}$$

which describes generally the birefringence in a crystal. For a homogeneous linear equation to have non-zero solution, its coefficient determinant must be equal to zero,

$$\begin{vmatrix} n_1^2 - (1 - K_1^2) n^2 & n^2 K_1 K_2 & n^2 K_1 K_3 \\ n^2 K_2 K_1 & n_2^2 - (1 - K_2^2) n^2 & n^2 K_2 K_3 \\ n^2 K_3 K_1 & n^2 K_3 K_2 & n_3^2 - (1 - K_3^2) n^2 \end{vmatrix} = 0 \tag{2.17}$$

which can be expanded as

$$n^4(n_1^2K_1^2+n_2^2K_2^2+n_3^2K_3^2)-n^2[n_2^2n_3^2(K_2^2+K_3^2)+n_3^2n_1^2(K_3^2+K_1^2)$$
$$+n_1^2n_2^2(K_1^2+K_2^2)]+n_1^2n_2^2n_3^2=0 \qquad (2.18)$$

where the relation $K_1^2+K_2^2+K_3^2=1$ is used. Eq.(2.18) expresses the relationship between the direction of wave vector $\boldsymbol{k}$ and the square of refractive index (n^2). If the wave vector $\boldsymbol{k}$ is given, from (2.18) we can solve for two real roots n'^2 and n''^2. By putting them back to (2.16), we can determine two sets of electric field intensities $(E_1':E_2':E_3')$ and $(E_1'':E_2'':E_3'')$, from which two linearly polarized directions $(D_1':D_2':D_3')$ and $(D_1'':D_2'':D_3'')$ are obtained by using (2.15). Any linearly polarized plane wave normally incident on the surface of a crystal must be decomposed into these two directions, in which the two components can propagate with different velocities c/n' and c/n''.

2.1.3 The Indicatrix (Refractive Index Ellipsoid) [25]

The conclusion reached in Section 2.1.2 can be visualized by introducing the *indicatrix* (*refractive index ellipsoid*). The refractive indices, n' and n'', of the two waves, as functions of the direction of their common wave normal, can be obtained by drawing an ellipsoid known as indicatrix, as shown in Figure 2.3.

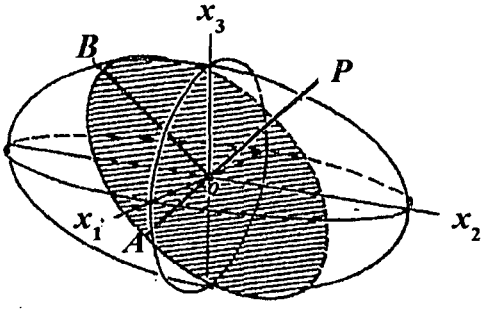

Figure 2.3 Representation of the indicatrix [25]

If x_1, x_2, x_3 are the principal axes of the permittivity (or dielectric impermeability) tensor, the indicatrix (or refractive index ellipsoid) is defined by the equation

$$\frac{x_1^2}{n_1^2}+\frac{x_2^2}{n_2^2}+\frac{x_3^2}{n_3^2}=1, \tag{2.19}$$

or

$$\beta_1 x_1^2 + \beta_2 x_2^2 + \beta_3 x_3^2 = 1 \tag{2.20}$$

where β_k (k=1,2,3) are the principal values of the relative dielectric impermeability tensorβ_{ij}, which is the inverse of the relative permittivity tensor ε_{ij}; n_k (k=1,2,3) are known as the *principal refractive indices.*

Let ***K*** be in *OP* direction, and the central section of the indicatrix perpendicular to *OP* will be an ellipse. Then the two wave fronts normal to *OP* that may be propagated through the crystal have refractive indices equal to the semi-axes, *OA* and *OB*, of this ellipse. The electric flux density ***D*** in the linearly polarized wave with refractive index equal to *OA* oscillates parallel to *OA*. Similarly, the displacement vector in the wave with refractive index equal to *OB* oscillates parallel to *OB*. From this it follows, as a special case, that the two possible waves with wave normal in direction x_1 have refractive indices n_2 and n_3; and ***D*** in the two waves is parallel to x_2 and x_3 respectively. Similar conclusions can be reached for the waves in the x_2 and x_3 directions. For this reason n_1, n_2, n_3 are called the *principal refractive indices.*

2.1.4 Birefringence in Various Classes of Crystals

2.1.4.1 Isotropic Materials and Cubic Classes For an isotropic medium, in any three mutually perpendicular directions, $n_1 = n_2 = n_3 = n_0$. From (2.18) we have $(n^2 - n_0^2)^2 = 0$. Thus, we can obtain two identical roots: $n'^2 = n''^2 = n_0^2$. This result indicates that for any propagating direction of the plane wave, the refractive indices are identical. By putting $n'^2 = n''^2 = n_0^2$ into (2.16), we have $\boldsymbol{K}\cdot\boldsymbol{E}$=0. Thus (2.15) becomes $\boldsymbol{D}$=$\varepsilon_0 n_0^2 \boldsymbol{E}$, which denotes no birefringence in an isotropic medium. For a crystal with cubic symmetry, the same conclusion can be reached, since $n_1 = n_2 = n_3 = n_0$ in the directions of the cubic symmetry. Therefore, like isotropic mediums, cubic crystals are called *optically isotropic*

crystals. The indicatrix for an optically isotropic medium is a sphere, which is shown in Figure 2.4.

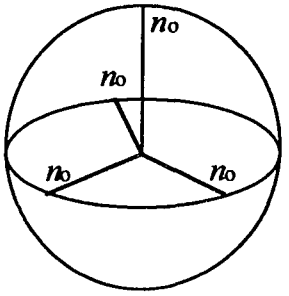

Figure 2.4 Indicatrix of an optically isotropic crystal.

2.1.4.2 Hexagonal, Tetragonal and Trigonal Crystals For *hexagonal*, *tetragonal* and *trigonal* crystals the indicatrix is necessarily an ellipsoid of revolution about the principal symmetry axis (see Figure 2.5). Assume x_3 as this axis the equation is written as

$$\frac{x_1^2}{n_0^2}+\frac{x_2^2}{n_0^2}+\frac{x_3^2}{n_e^2}=1 \tag{2.21}$$

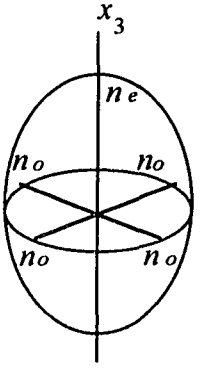

Figure 2.5 Indicatrix of a uniaxial crystal.

The central section perpendicular to the principal axis x_3, and only this central section, is a circle (radius n_0). Hence, only when the wave travels along the principal axis, there is no double refraction. The principal axis is called the *optic axis*, and the crystals are said to be *uniaxial*. n_0 and n_e are called the ordinary refractive index and the extraordinary refractive index, respectively. The crystal is said to be positive when $(n_e\text{-}n_0)$ is positive, and negative when $(n_e\text{-}n_0)$ is negative.

Since for the principal axis x_3, the dielectric constant tensor has rotational symmetry, the other two principal axes x_1 and x_2 may be arbitrarily chosen. Assume that the normal direction of the plane wave is (see Figure 2.6)

$$\boldsymbol{K}(K_1, K_2, K_3) = \boldsymbol{K}(0, \sin\theta, \cos\theta) \tag{2.22}$$

that is, $\boldsymbol{K}$ lies within the x_2x_3 plane and intersects the axis x_3 with an angle of θ. From (2.22) and let $n_1 = n_2 = n_0$, and $n_3 = n_e$, (2.18) becomes

$$(n^2 - n_0^2)[n^2(n_0^2 \sin^2\theta + n_e^2 \cos^2\theta) - n_0^2 n_e^2] = 0 \tag{2.23}$$

Solving (2.23) leads to

$$n'^2 = n_0^2, \quad \text{and} \quad n''^2 = \frac{n_0^2 n_e^2}{n_0^2 \sin^2\theta + n_e^2 \cos^2\theta} \tag{2.24}$$

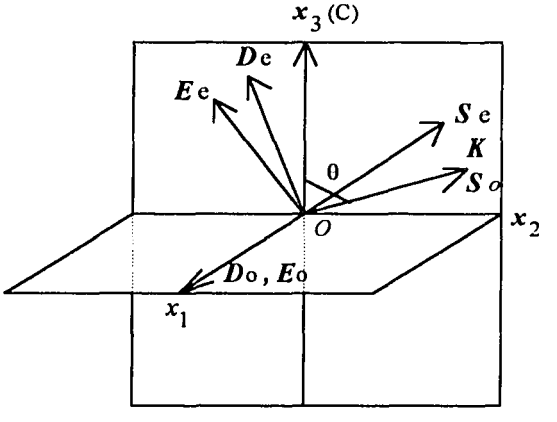

Figure 2.6 Relationship between various vectors in a uniaxial crystal.

which indicates that for given wave normal line direction $\boldsymbol{K}$, there exist two waves with different refractive index. For one wave, the refractive index does not change with the direction of $\boldsymbol{K}$; for the another wave, the refractive index is related with the direction of $\boldsymbol{K}$. When $\theta=0$, $n''=n_0$; when $\theta=90°$, $n''=n_e$; when θ takes other values, n'' will change between n_e and n_0. The plane wave with refractive index n_0 is a linearly polarized wave, its $\boldsymbol{E}$ vector is parallel with the $\boldsymbol{D}$ vector. Another plane wave with refractive index n_e is also a linearly polarized wave, but its $\boldsymbol{E}$ vector is not parallel with the $\boldsymbol{D}$ vector.

2.1.4.3 Orthorhombic, Monoclinic and Triclinic Crystals For the other three remaining crystal systems, the *orthorhombic*, *monoclinic* and *triclinic*, the indicatrix is a triaxial ellipsoid. There are two circular sections, and hence two privileged waves normal directions for which there is no double refraction. These two directions are called the *primary optic axes*, or the *optic axes*, and the crystals are said to be *biaxial*.

2.2 Photoelastic Effect

2.2.1 Number of Independent Photoelastic Coefficients [25]

The permittivity, and hence the refractive index, are, in general, functions of the stress on the crystal. The change of refractive index caused by stress is called the *photoelastic effect*. As discussed in Section 2.1.3, the refractive index of a crystal is specified by the indicatrix, which is an ellipsoid whose coefficients are the components of the relative dielectric impermeability tensor β_{ij} at optical frequency, namely,

$$\beta_{ij} x_i x_j = 1. \tag{2.25}$$

(By definition, $\beta_{ij}=\varepsilon_0 \partial E_i / \partial D_j$). Thus, in general, the small change of refractive index produced by stress is a small change in the *shape*, *size* and *orientation* of the indicatrix. This change is most conveniently specified by giving the small changes in the coefficients

β_{ij}. If we neglect higher-order terms in the stresses, the changes $\Delta\beta_{ij}$ in the coefficients, under an applied stress σ_{kl}, are given by

$$\Delta\beta_{ij}=\pi_{ijkl}\,\sigma_{kl} \tag{2.26}$$

where π_{ijkl}, a fourth-rank tensor, called the *piezo-optic coefficient tensor*. Since β_{ij} is a symmetric tensor, in (2.26), $\Delta\beta_{ij} = \Delta\beta_{ji}$ for all σ_{kl}, we have

$$\pi_{ijkl} = \pi_{jikl} \tag{2.27}$$

Furthermore, since $\sigma_{kl} = \sigma_{lk}$ if we ignore body-torque, we may put

$$\pi_{ijkl} = \pi_{ijlk} \tag{2.28}$$

The relations of (2.27) and (2.28) reduce the number of independent coefficients from 3^4=81 to 36.

The suffixes in $\Delta\beta_{ij}$ and σ_{kl} may be abbreviated by

$$\begin{pmatrix} \Delta\beta_{11} & \Delta\beta_{12} & \Delta\beta_{13} \\ \Delta\beta_{21} & \Delta\beta_{22} & \Delta\beta_{23} \\ \Delta\beta_{31} & \Delta\beta_{32} & \Delta\beta_{33} \end{pmatrix} \Rightarrow \begin{pmatrix} \Delta\beta_1 & \Delta\beta_6 & \Delta\beta_5 \\ \Delta\beta_6 & \Delta\beta_2 & \Delta\beta_4 \\ \Delta\beta_5 & \Delta\beta_4 & \Delta\beta_3 \end{pmatrix} \Rightarrow \begin{pmatrix} \Delta\beta_1 \\ \Delta\beta_2 \\ \Delta\beta_3 \\ \Delta\beta_4 \\ \Delta\beta_5 \\ \Delta\beta_6 \end{pmatrix}$$

$$\begin{pmatrix} \sigma_{11} & \sigma_{12} & \sigma_{13} \\ \sigma_{21} & \sigma_{22} & \sigma_{23} \\ \sigma_{31} & \sigma_{32} & \sigma_{33} \end{pmatrix} \Rightarrow \begin{pmatrix} \sigma_1 & \sigma_6 & \sigma_5 \\ \sigma_6 & \sigma_2 & \sigma_4 \\ \sigma_5 & \sigma_4 & \sigma_3 \end{pmatrix} \Rightarrow \begin{pmatrix} \sigma_1 \\ \sigma_2 \\ \sigma_3 \\ \sigma_4 \\ \sigma_5 \\ \sigma_6 \end{pmatrix}$$

We then have

$$\Delta\beta_m = \pi_{mn}\sigma_n \qquad (m, n = 1, 2, \ldots, 6) \tag{2.29}$$

where π_{mn} is a 6×6 matrix related to π_{ijkl} by the rules:

$$\pi_{mn}=\pi_{ijkl}, \quad \text{when } n = 1, 2, \text{ or } 3;$$

$$\pi_{mn}= 2\pi_{ijkl}, \quad \text{when } n = 4, 5, \text{ or } 6. \tag{2.30}$$

The factor of 2 appears because of the pairing of the shear stress terms in (2.26).

Notice that in general $\pi_{mn} \neq \pi_{mn}$. Thus, the number of independent π_{mn} for the *triclinic* classes remains 36. The number of independent π_{mn} for other classes reduces as a result of symmetry. For examples, for *isotropic medium*, such as epoxy resin, the most commonly used material for model made in conventional photoelasticity study, π_{mn} has two independent components [25]:

$$\begin{pmatrix} \pi_{11} & \pi_{12} & \pi_{12} & 0 & 0 & 0 \\ \pi_{12} & \pi_{11} & \pi_{12} & 0 & 0 & 0 \\ \pi_{12} & \pi_{12} & \pi_{11} & 0 & 0 & 0 \\ 0 & 0 & 0 & \pi_{11}-\pi_{12} & 0 & 0 \\ 0 & 0 & 0 & 0 & \pi_{11}-\pi_{12} & 0 \\ 0 & 0 & 0 & 0 & 0 & \pi_{11}-\pi_{12} \end{pmatrix}. \tag{2.31}$$

For the classes of $\bar{4}32$, *432*, and *m3m* of cubic symmetry, where the cube axes are tetrads, such as silicon, GaAs, and diamond, the number of independent π_{mn} is 3 [25]:

$$\begin{pmatrix} \pi_{11} & \pi_{12} & \pi_{12} & 0 & 0 & 0 \\ \pi_{12} & \pi_{11} & \pi_{12} & 0 & 0 & 0 \\ \pi_{12} & \pi_{12} & \pi_{11} & 0 & 0 & 0 \\ 0 & 0 & 0 & \pi_{44} & 0 & 0 \\ 0 & 0 & 0 & 0 & \pi_{44} & 0 \\ 0 & 0 & 0 & 0 & 0 & \pi_{44} \end{pmatrix} \tag{2.32}$$

The other two classes, *23* and *m3*, where the cube axes are diads, such as potassium alum and barium nitrate, need 4 coefficients [25]:

$$\begin{pmatrix} \pi_{11} & \pi_{12} & \pi_{13} & 0 & 0 & 0 \\ \pi_{13} & \pi_{11} & \pi_{12} & 0 & 0 & 0 \\ \pi_{12} & \pi_{13} & \pi_{11} & 0 & 0 & 0 \\ 0 & 0 & 0 & \pi_{44} & 0 & 0 \\ 0 & 0 & 0 & 0 & \pi_{44} & 0 \\ 0 & 0 & 0 & 0 & 0 & \pi_{44} \end{pmatrix} \tag{2.33}$$

Some measured values of π_{ij} for several microelectronic materials are given in Table 2.1. The values are usually dependent on the wavelength of the light.

Table 2.1 Values of components of piezo-optic coefficients of some materials ($\times 10^{-14} cm^2/dyn$)

Crystal	Point group	Wavelength	$\pi_{11}-\pi_{12}$	π_{44}
silicon [26]	*m3m*	1.15μm	-12.22	-6.50
germanium [27]	*m3m*	3.39μm	-2.8	-10.5
GaAs [28]	$\bar{4}32$	1.15μm	-5.4	-10.0
diamond [29]	*m3m*	0.589μm	-8.0	-2.7

2.2.2 Photoelasticity of Isotropic Media

For an *isotropic* material, if the directions of the principal stresses are chosen as the reference axes (x_1, x_2, x_3), the matrix equation (2.29), when written out in full, is

$$\begin{pmatrix}\Delta\beta_1\\ \Delta\beta_2\\ \Delta\beta_3\\ \Delta\beta_4\\ \Delta\beta_5\\ \Delta\beta_6\end{pmatrix} = \begin{pmatrix}\pi_{11} & \pi_{12} & \pi_{12} & 0 & 0 & 0\\ \pi_{12} & \pi_{11} & \pi_{12} & 0 & 0 & 0\\ \pi_{12} & \pi_{12} & \pi_{11} & 0 & 0 & 0\\ 0 & 0 & 0 & \pi_{11}-\pi_{12} & 0 & 0\\ 0 & 0 & 0 & 0 & \pi_{11}-\pi_{12} & 0\\ 0 & 0 & 0 & 0 & 0 & \pi_{11}-\pi_{12}\end{pmatrix}\begin{pmatrix}\sigma_1\\ \sigma_2\\ \sigma_3\\ 0\\ 0\\ 0\end{pmatrix}$$

$$= \begin{pmatrix}\pi_{11}\sigma_1+\pi_{12}\sigma_2+\pi_{12}\sigma_3\\ \pi_{12}\sigma_1+\pi_{11}\sigma_2+\pi_{12}\sigma_3\\ \pi_{12}\sigma_1+\pi_{12}\sigma_2+\pi_{11}\sigma_3\\ 0\\ 0\\ 0\end{pmatrix} \qquad (2.34)$$

Since $\beta_4=\beta_5=\beta_6=0$, the axes of the indicatrix are simply x_1, x_2 and x_3, that means the indicatrix takes the same orientation as the stress ellipsoid. To obtain the changes in the three principal refractive indices we write $\beta_1 = 1/n_1^2$. Hence, $\Delta\beta_1 = -(2/n_1^3)\Delta n_1$. To a sufficient approximation we may replace n_1 by n_0 and obtain

$$\Delta n_1 = -\frac{1}{2}(n_0)^3\Delta\beta_1 = -\frac{1}{2}(n_0)(\pi_{11}\sigma_1+\pi_{12}\sigma_2+\pi_{12}\sigma_3) \qquad (2.35)$$

Similarly,

$$\Delta n_2 = -\frac{1}{2}(n_0)^3(\pi_{12}\sigma_1 + \pi_{11}\sigma_2 + \pi_{12}\sigma_3) \tag{2.36}$$

$$\Delta n_3 = -\frac{1}{2}(n_0)^3(\pi_{12}\sigma_1 + \pi_{12}\sigma_2 + \pi_{11}\sigma_3) \tag{2.37}$$

Therefore, an isotropic medium when under stress, in general, will behave like an optically biaxial material. From Eqs.(2.35), (2.36) and (2.37), the birefringence for light traveling along x_1 is evidently

$$\Delta n_2 - \Delta n_3 = -\frac{1}{2}(n_0)^3(\pi_{11} - \pi_{12})(\sigma_2 - \sigma_3) \tag{2.38}$$

and, for light traveling along x_2,

$$\Delta n_3 - \Delta n_1 = -\frac{1}{2}(n_0)^3(\pi_{11} - \pi_{12})(\sigma_3 - \sigma_1) \tag{2.39}$$

and, for light traveling along x_3,

$$\Delta n_1 - \Delta n_2 = -\frac{1}{2}(n_0)^3(\pi_{11} - \pi_{12})(\sigma_1 - \sigma_2) \tag{2.40}$$

Eqs.(2.38), (2.39) and (2.40) can be rewritten as

$$\begin{aligned} n_2 - n_3 &= C(\sigma_2 - \sigma_3) \\ n_3 - n_1 &= C(\sigma_3 - \sigma_1) \\ n_1 - n_2 &= C(\sigma_1 - \sigma_2) \end{aligned} \tag{2.41}$$

where n_1, n_2, and n_3 are the principal refractive indices; σ_1, σ_2, and σ_3 are the principal stresses; C is known as the *relative stress-optic coefficient*. Eq.(2.41) is the well-known *stress-optic law* that is used to the case of an isotropic medium. From analysis above, it is obvious that for an isotropic medium, the principal axes of the refractive index ellipsoid at any point, representing the local optical properties of the material, coincide with the principal axes of the stress ellipsoid at that point.

2.2.3 Photoelasticity of Cubic Crystals

It is of interest to examine analytically a few special cases of cubic crystals under stress. Consider a cubic crystal of class *23* or *m3* under a uniaxial tensile stress σ applied parallel

to a cube axis. Let x_1 be the direction of the stress, and let x_2, x_3 be the other two axes. Before the stress is put on, the indicatrix is a sphere,

$$\beta_0(x_1^2 + x_2^2 + x_3^2) = 1 \tag{2.42}$$

and the refractive index is given by $\beta_0 = 1/(n_0)^2$. Under the stress the indicatrix becomes

$$\beta_1 x_1{}^2 + \beta_2 x_2{}^2 + \beta_3 x_3{}^2 + 2\beta_4 x_2 x_3 + 2\beta_5 x_1 x_3 + 2\beta_6 x_1 x_2 = 1 \tag{2.43}$$

The matrix equation of (2.29), when written out in full for this case, is

$$\begin{pmatrix} \Delta\beta_1 \\ \Delta\beta_2 \\ \Delta\beta_3 \\ \Delta\beta_4 \\ \Delta\beta_5 \\ \Delta\beta_6 \end{pmatrix} = \begin{pmatrix} \pi_{11} & \pi_{12} & \pi_{13} & 0 & 0 & 0 \\ \pi_{13} & \pi_{11} & \pi_{12} & 0 & 0 & 0 \\ \pi_{12} & \pi_{13} & \pi_{11} & 0 & 0 & 0 \\ 0 & 0 & 0 & \pi_{44} & 0 & 0 \\ 0 & 0 & 0 & 0 & \pi_{44} & 0 \\ 0 & 0 & 0 & 0 & 0 & \pi_{44} \end{pmatrix} \begin{pmatrix} \sigma \\ 0 \\ 0 \\ 0 \\ 0 \\ 0 \end{pmatrix} = \begin{pmatrix} \pi_{11}\sigma \\ \pi_{13}\sigma \\ \pi_{12}\sigma \\ 0 \\ 0 \\ 0 \end{pmatrix} \tag{2.44}$$

Since $\beta_4 = \beta_5 = \beta_6 = 0$ the axes of the indicatrix are simply x_1, x_2 and x_3. To obtain the changes in the three principal refractive indices we write $\beta_1 = 1/n_1^2$. Hence, $\Delta\beta_1 = -(2/n_1^3)\Delta n_1$. To a sufficient approximation we may replace n_1 by n_0 and obtain

$$\Delta n_1 = -\frac{1}{2}(n_0)^3 \Delta\beta_1 = -\frac{1}{2}(n_0)^3 \pi_{11}\sigma \tag{2.45}$$

Similarly,

$$\Delta n_2 = -\frac{1}{2}(n_0)^3 \pi_{13}\sigma \tag{2.46}$$

$$\Delta n_3 = -\frac{1}{2}(n_0)^3 \pi_{12}\sigma \tag{2.47}$$

The crystal therefore becomes biaxial. In a crystal belonging to one of the other three cubic classes($\bar{4}3m, 432, m3m$) it has been seen that $\pi_{12} = \pi_{13}$. Hence, in this case, $\Delta n_2 = \Delta n_3$ and the crystal is uniaxial. From Eqs.(2.45) and (2.47) the birefringence for light traveling along x_2 is evidently

$$\Delta n_1 - \Delta n_3 = -\frac{1}{2}(n_0)^3(\pi_{11} - \pi_{12})\sigma \tag{2.48}$$

and, for light traveling along x_3,

$$\Delta n_1 - \Delta n_2 = -\frac{1}{2}(n_0)^3(\pi_{11} - \pi_{13})\sigma \tag{2.49}$$

Formulae (2.48) and (2.49) refer to a cubic crystal under uniaxial tension parallel to a cube axis. They give the birefringence along the other two cube axes. In these cases, the directions of the principal stresses and the directions of the principal refractive indices are identical.

2.3 Piezo-Optic Coefficient Tensor π

2.3.1 Transformation Law for Fourth-Rank Tensor

The relation between the new coordinate axes (x'_1, x'_2, x'_3) and the old coordinate axes (x_1, x_2, x_3) is given by

$$x'_i = A\, x_i \qquad (i=1,2,3) \tag{2.50}$$

where A is the transformation matrix of the coordinate axes, which is expressed with the direction cosines (l, m, n) by

$$A=\begin{pmatrix} l_1 & m_1 & n_1 \\ l_2 & m_2 & n_2 \\ l_3 & m_3 & n_3 \end{pmatrix} \tag{2.51}$$

Since the matrix form of photoelastic law is frequently used for convenience, it is necessary to derive the transformation law for the fourth-rank tensor in matrix form. Assume the matrix form of transformation law of second-rank tensor take the following forms:

$$\sigma' = B_\sigma \sigma \tag{2.52}$$

$$\Delta\beta' = B_\sigma \Delta\beta \tag{2.53}$$

where σ, β and σ', β' are the second-rank stress tensors and second-rank dielectric impermeability tensors in old and new coordinate systems, respectively, which are expressed as 1×6 matrices. B_σ is the coordinate transformation matrix for σ and $\Delta\beta$, which is a 6×6 matrix. If the transformation matrix for the coordinate axes is given by (2.51), it is readily to obtain the 6×6 matrix of B_σ [30]:

$$B_\sigma=\begin{pmatrix} l_1^2 & m_1^2 & n_1^2 & 2m_1n_1 & 2n_1l_1 & 2l_1m_1 \\ l_2^2 & m_2^2 & n_2^2 & 2m_2n_2 & 2n_2l_2 & 2l_2m_2 \\ l_3^2 & m_3^2 & n_3^2 & 2m_3n_3 & 2n_3l_3 & 2l_3m_3 \\ l_2l_3 & m_2m_3 & n_2n_3 & m_2n_3+m_3n_2 & n_2l_3+n_3l_2 & l_2m_3+l_3m_2 \\ l_3l_1 & m_3m_1 & n_3n_1 & m_3n_1+m_1n_3 & n_3l_1+n_1l_3 & l_3m_1+l_1m_3 \\ l_1l_2 & m_1m_2 & n_1n_2 & m_1n_2+m_2n_1 & n_1l_2+n_2l_1 & l_1m_2+l_2m_1 \end{pmatrix} \tag{2.54}$$

From Eqs.(2.52) and (2.53), we have

$$\begin{aligned} \Delta\beta' &= B_\sigma \Delta\beta \\ &= B_\sigma \pi B_\sigma^{-1} \sigma' \\ &= \pi'\sigma' \end{aligned} \tag{2.55}$$

Thus, the transformation law for piezo-optic coefficient matrix is given as

$$\pi' = B_\sigma \pi B_\sigma^{-1} \tag{2.56}$$

where both π' and π are 6×6 matrices, B_σ^{-1} is the inverse matrix of B_σ. Eq.(2.56) is known as *the transformation law for fourth-rank tensor in matrix form.* If the transformation matrix of coordinate axes is known, B_σ and B_σ^{-1} can be calculated from (2.54), and the transformation of π' and π can be performed by using (2.56). In the following sections, we shall use (2.56) to derive the matrix forms of π for the cubic classes of $\bar{4}3m$, *432*, *m3m* in two commonly used coordinate systems.

2.3.2 Matrix Forms of π in the [110][$\bar{1}$10][001]Coordinate System

[100], [010], and [001] are chosen as the original coordinate axes, and the coordinate axes of new coordinate system are in the [110], [$\bar{1}$10], and [001] directions, respectively. The transformation matrix A of the coordinate system is given by

$$A=\begin{pmatrix} \frac{\sqrt{2}}{2} & \frac{\sqrt{2}}{2} & 0 \\ -\frac{\sqrt{2}}{2} & \frac{\sqrt{2}}{2} & 0 \\ 0 & 0 & 1 \end{pmatrix} \tag{2.57}$$

By substituting the components of the matrix A of (2.57) into (2.54), the matrix of B_σ and its inverse B_σ^{-1} are written as

$$B_\sigma = \begin{pmatrix} \frac{1}{2} & \frac{1}{2} & 0 & 0 & 0 & 1 \\ \frac{1}{2} & \frac{1}{2} & 0 & 0 & 0 & -1 \\ 0 & 0 & 1 & 0 & 0 & 0 \\ 0 & 0 & 0 & \frac{1}{\sqrt{2}} & -\frac{1}{\sqrt{2}} & 0 \\ 0 & 0 & 0 & \frac{1}{\sqrt{2}} & \frac{1}{\sqrt{2}} & 0 \\ -\frac{1}{2} & \frac{1}{2} & 0 & 0 & 0 & 0 \end{pmatrix} \tag{2.58}$$

and

$$B_\sigma^{-1} = \begin{pmatrix} \frac{1}{2} & \frac{1}{2} & 0 & 0 & 0 & -1 \\ \frac{1}{2} & \frac{1}{2} & 0 & 0 & 0 & 1 \\ 0 & 0 & 1 & 0 & 0 & 0 \\ 0 & 0 & 0 & \frac{1}{\sqrt{2}} & \frac{1}{\sqrt{2}} & 0 \\ 0 & 0 & 0 & -\frac{1}{\sqrt{2}} & \frac{1}{\sqrt{2}} & 0 \\ \frac{1}{2} & -\frac{1}{2} & 0 & 0 & 0 & 0 \end{pmatrix} \tag{2.59}$$

By substituting Eqs.(2.58), (2.59) and (2.32) into (2.56), we obtain the piezo-optic coefficient matrix in the [110][$\bar{1}$10][001] coordinate system:

$$\pi' = \begin{pmatrix} \frac{1}{2}(\pi_{11}+\pi_{12}+\pi_{44}) & \frac{1}{2}(\pi_{11}+\pi_{12}-\pi_{44}) & \pi_{12} & 0 & 0 & 0 \\ \frac{1}{2}(\pi_{11}+\pi_{12}-\pi_{44}) & \frac{1}{2}(\pi_{11}+\pi_{12}+\pi_{44}) & \pi_{12} & 0 & 0 & 0 \\ \pi_{12} & \pi_{12} & \pi_{11} & 0 & 0 & 0 \\ 0 & 0 & 0 & \pi_{44} & 0 & 0 \\ 0 & 0 & 0 & 0 & \pi_{44} & 0 \\ 0 & 0 & 0 & 0 & 0 & \pi_{11}-\pi_{12} \end{pmatrix} \tag{2.60}$$

2.3.3 Matrix Forms of π in the [112][$\bar{1}$10][$\bar{1}\bar{1}$1] Coordinate System

If the original coordinate axes are in the [100], [010], and [001] directions and the new coordinate axes are chosen in the [112], [$\bar{1}$10], and [$\bar{1}\bar{1}$1] directions, the transformation matrix of the coordinate axes is expressed by

$$A = \frac{1}{\sqrt{6}} \begin{pmatrix} 1 & 1 & 2 \\ -\sqrt{3} & \sqrt{3} & 0 \\ -\sqrt{2} & -\sqrt{2} & \sqrt{2} \end{pmatrix} \tag{2.61}$$

From (2.61) and (2.54), we can calculate the matrix of B_σ and its inverse B_σ^{-1}:

$$B_\sigma = \frac{1}{6}\begin{pmatrix} 1 & 1 & 4 & 4 & 4 & 2 \\ 3 & 3 & 0 & 0 & 0 & -6 \\ 2 & 2 & 2 & -4 & -4 & 4 \\ \sqrt{6} & -\sqrt{6} & 0 & \sqrt{6} & -\sqrt{6} & 0 \\ -\sqrt{2} & -\sqrt{2} & 2\sqrt{2} & -\sqrt{2} & -\sqrt{2} & -2\sqrt{2} \\ -\sqrt{3} & \sqrt{3} & 0 & 2\sqrt{3} & -2\sqrt{3} & 0 \end{pmatrix} \tag{2.62}$$

and

$$B_\sigma^{-1} = \frac{1}{6}\begin{pmatrix} 1 & 3 & 2 & 2\sqrt{6} & -2\sqrt{2} & -2\sqrt{3} \\ 1 & 3 & 2 & -2\sqrt{6} & -2\sqrt{2} & 2\sqrt{3} \\ 4 & 0 & 2 & 0 & 4\sqrt{2} & 0 \\ 2 & 0 & -2 & \sqrt{6} & -\sqrt{2} & 2\sqrt{3} \\ 2 & 0 & -2 & -\sqrt{6} & -\sqrt{2} & -2\sqrt{3} \\ 1 & -3 & 2 & 0 & -2\sqrt{2} & 0 \end{pmatrix} \tag{2.63}$$

By substituting Eqs.(2.62), (2.63) and (2.32) into (2.56), we obtain the piezo-optic coefficient matrix in the $[112][\bar{1}10][\bar{1}\bar{1}1]$ coordinate system, that is

$$\pi' = \begin{pmatrix} 18(\pi_{11}+\pi_{12}+\pi_{44}) & 6(\pi_{11}+5\pi_{12}-\pi_{44}) & 12(\pi_{11}+2\pi_{12}-\pi_{44}) \\ 6(\pi_{11}+5\pi_{12}-\pi_{44}) & 18(\pi_{11}+\pi_{12}+\pi_{44}) & 12(\pi_{11}+2\pi_{12}-\pi_{44}) \\ 12(\pi_{11}+2\pi_{12}-\pi_{44}) & 12(\pi_{11}+2\pi_{12}-\pi_{44}) & 12(\pi_{11}+2\pi_{12}+2\pi_{44}) \\ 0 & 0 & 0 \\ 6\sqrt{2}(\pi_{11}-\pi_{12}-\pi_{44}) & -6\sqrt{2}(\pi_{11}-5\pi_{12}-\pi_{44}) & 0 \\ 0 & 0 & 0 \end{pmatrix}$$

$$\begin{pmatrix} 0 & 12\sqrt{2}(\pi_{11}-\pi_{12}-\pi_{44}) & 0 \\ 0 & -12\sqrt{2}(\pi_{11}-\pi_{12}-\pi_{44}) & 0 \\ 0 & 0 & 0 \\ 12(2\pi_{11}-2\pi_{12}+\pi_{44}) & 0 & -4\sqrt{8}(\pi_{11}-\pi_{12}-\pi_{44}) \\ 0 & 12(2\pi_{11}-2\pi_{12}+\pi_{44}) & 0 \\ -4\sqrt{8}(\pi_{11}-\pi_{12}-\pi_{44}) & 0 & 12(\pi_{11}-\pi_{12}+2\pi_{44}) \end{pmatrix} \tag{2.64}$$

2.3.4 Piezo-Optic Coefficients for Arbitrarily Orientation

In some applications, it is required to know the piezo-optic coefficients in certain reference axes that are intersected above coordinates with an angle φ. In this section, we only concern with the cases of the classes of $\bar{4}32$, *432*, and *m3m* of the cubic symmetry. With the piezo-optic coefficients of (2.60) and (2.64), we select a new coordinate system, which is formed by rotating the old coordinate system around the [001] axis for (100) wafers (or the $[\bar{1}\bar{1}1]$ axis for (111) wafers) with an angle φ. The transformation matrix of the rotation is expressed as

$$A=\begin{pmatrix} \cos\varphi & \sin\varphi & 0 \\ -\sin\varphi & \cos\varphi & 0 \\ 0 & 0 & 1 \end{pmatrix} \tag{2.65}$$

From Eqs.(2.65) and (2.54), we can calculate the corresponding matrix B_σ and its unverse matrix B_σ^{-1}. From Eqs.(2.32) and (2.56), we can obtain $\pi(\varphi)$ in the new coordinate system.

In a (001) wafer, [110], $[\bar{1}10]$, and [001] are adopted as the original coordinate axes, and [001] is chosen as the rotating axis. The general form of the 6×6 matrix $\pi(\varphi)$ in the new coordinate system is obtained as

$$\pi(\varphi)=\begin{pmatrix} \frac{1}{2}(\pi_{11}+\pi_{12}+\pi_{44})+\frac{1}{2}(\pi_{11}-\pi_{12}-\pi_{44})\sin^2 2\varphi & \frac{1}{2}(\pi_{11}+\pi_{12}-\pi_{44})-\frac{1}{2}(\pi_{11}-\pi_{12}-\pi_{44})\sin^2 2\varphi & \pi_{12} & 0 & 0 & \frac{1}{4}(\pi_{11}-\pi_{12}-\pi_{44})\sin 4\varphi \\ \frac{1}{2}(\pi_{11}+\pi_{12}-\pi_{44})-\frac{1}{2}(\pi_{11}-\pi_{12}-\pi_{44})\sin^2 2\varphi & \frac{1}{2}(\pi_{11}+\pi_{12}+\pi_{44})+\frac{1}{2}(\pi_{11}-\pi_{12}-\pi_{44})\sin^2 2\varphi & \pi_{12} & 0 & 0 & -\frac{1}{4}(\pi_{11}-\pi_{12}-\pi_{44})\sin 4\varphi \end{pmatrix}$$

$$\begin{pmatrix}
\pi_{12} & 0 & 0 & \frac{1}{2}(\pi_{11}-\pi_{12}-\pi_{44})\sin 4\varphi \\
\pi_{12} & 0 & 0 & -\frac{1}{2}(\pi_{11}-\pi_{12}-\pi_{44})\sin 4\varphi \\
\pi_{11} & 0 & 0 & 0 \\
0 & \pi_{44} & 0 & 0 \\
0 & 0 & \pi_{44} & 0 \\
0 & 0 & 0 & \pi_{44}\sin^2 2\varphi+(\pi_{11}-\pi_{12})\cos^2 2\varphi
\end{pmatrix} \tag{2.66}$$

where φ is the angle between the [110] direction and new axis.

In a (111) wafer, the original coordinate axes are [112], $[\bar{1}10]$, and $[\bar{1}\bar{1}1]$, and $[\bar{1}\bar{1}1]$ is chosen as the rotating axis. The general form of the 6×6 matrix $\pi(\varphi)$ the new coordinate system is:

$$\begin{pmatrix}
\frac{1}{2}(\pi_{11}+\pi_{12}+\pi_{44}) & \frac{1}{6}(\pi_{11}+5\pi_{12}-\pi_{44}) \\
\frac{1}{6}(\pi_{11}+5\pi_{12}-\pi_{44}) & \frac{1}{2}(\pi_{11}+\pi_{12}+\pi_{44}) \\
\frac{1}{3}(\pi_{11}+2\pi_{12}-\pi_{44}) & \frac{1}{3}(\pi_{11}+2\pi_{12}-\pi_{44}) \\
\frac{\sqrt{2}}{6}(\pi_{11}+\pi_{12}+\pi_{44})\cos 3\varphi & -\frac{\sqrt{2}}{6}(\pi_{11}+\pi_{12}+\pi_{44})\cos 3\varphi \\
\frac{\sqrt{2}}{6}(\pi_{11}+\pi_{12}+\pi_{44})\sin 3\varphi & -\frac{\sqrt{2}}{6}(\pi_{11}+\pi_{12}+\pi_{44})\sin 3\varphi \\
0 & 0
\end{pmatrix}$$

$$\begin{pmatrix}
\frac{1}{3}(\pi_{11}+2\pi_{12}-\pi_{44}) & \frac{\sqrt{2}}{3}(\pi_{11}-\pi_{12}-\pi_{44})\cos 3\varphi \\
\frac{1}{3}(\pi_{11}+2\pi_{12}-\pi_{44}) & -\frac{\sqrt{2}}{3}(\pi_{11}-\pi_{12}-\pi_{44})\cos 3\varphi \\
\frac{1}{3}(\pi_{11}+2\pi_{12}+2\pi_{44}) & 0 \\
0 & \frac{1}{3}(\pi_{11}-2\pi_{12}+\pi_{44}) \\
0 & 0 \\
0 & -\frac{\sqrt{2}}{3}(\pi_{11}-\pi_{12}-\pi_{44})\sin 3\varphi
\end{pmatrix}$$

$$\begin{pmatrix}
\frac{\sqrt{2}}{3}(\pi_{11}-\pi_{12}-\pi_{44})\sin 3\varphi & 0 \\
-\frac{\sqrt{2}}{3}(\pi_{11}-\pi_{12}-\pi_{44})\sin 3\varphi & 0 \\
0 & 0 \\
0 & -\frac{\sqrt{2}}{3}(\pi_{11}-\pi_{12}-\pi_{44})\sin 3\varphi \\
\frac{1}{3}(2\pi_{11}-2\pi_{12}+\pi_{44}) & \frac{\sqrt{2}}{3}(\pi_{11}-\pi_{12}-\pi_{44})\cos 3\varphi \\
\frac{\sqrt{2}}{3}(\pi_{11}-\pi_{12}-\pi_{44})\cos 3\varphi & \frac{1}{3}(\pi_{11}-2\pi_{12}+\pi_{44})
\end{pmatrix} \tag{2.67}$$

where φ is the angle between the [112] direction and new axis.

2.4 Stress-Optic Law in Crystals

2.4.1 General Form of the Stress-Optic Law

While free from stress, the indicatrix of a crystal is expressed by (2.20). Notice that for an isotropic medium or a cubic crystal, the indicatrix is a sphere. When stressed, the refractive index ellipsoid of the crystal will be distorted. If the principal stress directions are chosen as the axial directions of the coordinate system (x_1', x_2', x_3'), the equation of the refractive index ellipsoid takes the form:

$$\beta_1 x_1'^2 + \beta_2 x_2'^2 + \beta_3 x_3'^2 + 2\beta_4 x_2' x_3' + 2\beta_5 x_1' x_3' + 2\beta_6 x_1' x_2' = 1 \qquad (2.68)$$

where β_i (i=1, 2, ..., 6) are the components of the dielectric impermeability tensor. Note here β_1, β_2, and β_3 are not necessarily the principal dielectric impermeabilities. We will illustrate the relation between the principal stress directions and the principal refractive index directions, by considering two-dimensional case. If an observation is made along the x_3' axis, *i.e.*, the wave vector $\boldsymbol{k}$ is in the direction of x_3', and the directions of two principal stresses σ_1 and σ_2 are along x_1' and x_2' respectively, the central section of the refractive index ellipsoid normal to the x_3' direction has the form:

$$\beta_1 x_1'^2 + \beta_2 x_2'^2 + 2\beta_6 x_1' x_2' = 1 \qquad (2.69)$$

We shall discuss the photoelastic effect in two cases of β_6 as follows.

(*a*) $\beta_6=0$, denoting that in the (x_1', x_2', x_3') coordinate system, the principal semi-axes of the refractive index ellipse coincide with the coordinate axes x_1' and x_2' (see Figure 2.7). The polarization directions of the two polarized components propagating along the x_3' direction coincide with the directions of two principal stresses. The corresponding refractive indices are given by

$$n_1 = 1/\sqrt{\beta_1}$$
$$n_2 = 1/\sqrt{\beta_2} \qquad (2.70)$$

This is similar to the case of the isotropic material. The difference (β_1- β_2) directly reflects the birefringence index.

(*b*) $\beta_6 \neq 0$, in which case, the principal axes of the central section ellipse of the refractive index ellipsoid do not coincide with the coordinate axes x_1' and x_2'. That is, the vibration directions, y_1 and y_2, of the two polarized lights propagating along the x_3' direction does not coincide with the directions of two principal stresses (see Figure 2.8). Eq.(2.70) for principal refractive indices is no longer valid. β_1-β_2 does not represent the birefringence index.

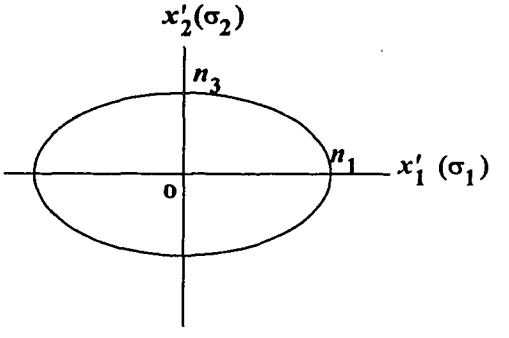

Figure 2.7 Central section ellipse of refractive index ellipsoid when $\beta_6=0$.

The angle α between the polarization directions of the two polarized lights and the directions of the two principal stresses can be expressed by

$$\tan 2\alpha = \frac{2\beta_6}{\beta_1 - \beta_2} \tag{2.71}$$

For the unstressed cubic crystals, in a rectangular coordinate system, $\beta_1^0 = \beta_2^0 = \beta_3^0 = 1/n_0^2$ and $\beta_4^0 = \beta_5^0 = \beta_6^0 = 0$, n_0 is the refractive index while unstressed. Let $\Delta\beta_i = \beta_i - \beta_i^0$ (i = 1, 2, ..., 6). Thus, (2.71) can be rewritten as

$$\tan 2\alpha = \frac{2\Delta\beta_6}{\Delta\beta_1 - \Delta\beta_2} \tag{2.72}$$

In order to study the *birefringence index*, *i.e.*, the length difference of long semi-axis and short semi-axis of a refractive index ellipse, choose the directions of the long axis and the short axis of the refractive index ellipse, *i.e.*, the oscillation directions of the two

polarized lights, as the axial directions of the new coordinate system, as shown in Figure 2.8. In the new coordinate system, the refractive index ellipse is expressed as

$$\beta_1' y_1^2 + \beta_2' y_2^2 = 1 \tag{2.73}$$

where y_1 and y_2 are the directions of the principal refractive indices. The principal refractive indices, *i.e.*, the two semi-axes of the refractive index ellipse, are expressed by

$$n_1 = \frac{1}{\sqrt{\beta_1'}}$$

$$n_2 = \frac{1}{\sqrt{\beta_2'}} \tag{2.74}$$

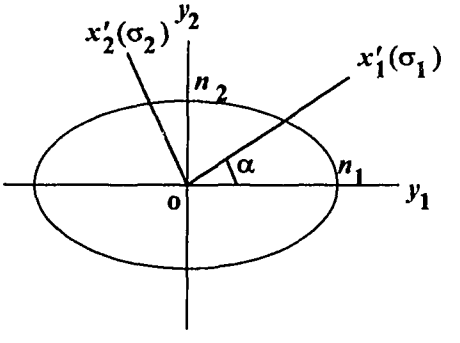

Figure 2.8 Central section ellipse of refractive index ellipsoid when $\beta_6 \neq 0$.

The relation between (β_1', β_2') and $(\beta_1, \beta_2, \beta_6)$ are

$$\beta_1' = \beta_1 \cos^2\alpha + \beta_2 \sin^2\alpha + \beta_6 \sin 2\alpha$$

$$\beta_2' = \beta_1 \sin^2\alpha + \beta_2 \cos^2\alpha - \beta_6 \sin 2\alpha \tag{2.75}$$

From Eqs.(2.71) and (2.75), the birefringence index $\beta_1' - \beta_3'$ can be expressed in the form:

$$\beta_1' - \beta_2' = \sqrt{(\beta_1 - \beta_2)^2 + 4\beta_6^2} \tag{2.76}$$

In the linear range of stress, the relation between the birefringence phase difference δ and the birefringence index is given by [31]

$$\delta = \frac{\pi d n_0^3}{\lambda}(\beta_1' - \beta_2')$$

$$= \frac{\pi d n_0^3}{\lambda}\sqrt{(\beta_1-\beta_2)^2+4\beta_6{}^2} \tag{2.77}$$

where d is the thickness of sample, λ the wavelength of light. Solving Eqs.(2.72) and (2.77), yields [31]

$$\Delta\beta_1 - \Delta\beta_2 = \pm\frac{\lambda\delta}{\pi d n_0^3}\cos 2\alpha$$

$$2\Delta\beta_6 = \pm\frac{\lambda\delta}{\pi d n_0^3}\sin 2\alpha \tag{2.78}$$

This is the *general form of the stress-optic law* [31], which includes the effect of the anisotropic property of photoelasticity in a crystal. Due to the anisotropic property of the crystal, the angle α is generally not equal to zero. Consequently, the directions of principal stresses do not coincide with the directions of principal refractive indices. The relation between the directions of principal stress σ_1 and principal refractive index n_1 is shown in Figure 2.9, where ϕ is the angle between principal refractive index n_1 and reference axis x, θ is the angle between principal stress σ_1 and reference axis x, α is the angle between principal refractive index n_1 and principal stress σ_1. That is

$$\theta = \alpha + \phi \tag{2.79}$$

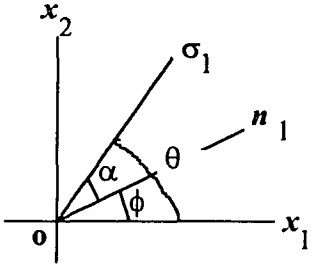

Figure 2.9 Relation of α, θ and ϕ.

If we have the knowledge of the relation between the change of the relative dielectric impermeability tensor and the stress tensor as well as the birefringence phase difference δ, we can determine the principal stress difference and the directions of

principal refractive indices by using stress-optic law of (2.78). Then, we can decide the directions of the principal stresses from (2.79). In the following sections, we shall study the relation between the change of the relative dielectric impermeability tensor and the stress tensor for cubic crystals of classes $\bar{4}32$, *432*, and *m3m*, and derive the analytical expressions of stress-optic law for some commonly used coordinate systems.

2.4.2 Application in the [112][$\bar{1}$10][$\bar{1}\bar{1}$1] Coordinate System

2.4.2.1 Observation Made along the [$\bar{1}\bar{1}$1] Direction The original coordinate axes (x_1, x_2, and x_3) are chosen in the [112], [$\bar{1}$10], and [$\bar{1}\bar{1}$1] directions, as shown in Figure 2.10. We define a new coordinate system (x_1',x_2',x_3), where x_1' and x_2' are in the directions of the principal stresses, and within the x_1-x_2 plane. x_1' and x_1 (also x_2' and x_2) constitute an angle of φ, as shown in Figure 2.10.

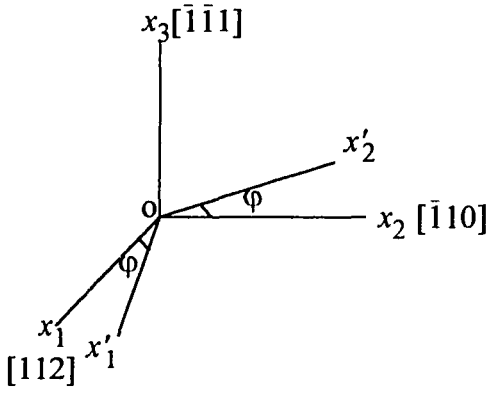

Figure 2.10 Relation between coordinates of (x_1,x_2,x_3) and (x_1',x_2',x_3) in the [112][$\bar{1}$10][$\bar{1}\bar{1}$1] coordinate system.

The central section of the refractive index ellipsoid, normal to x_3 direction, is given by (2.69). The angle α between the oscillation direction of the polarized light, y_1 or y_2, and the direction of the principal stress, x_1' or x_2', as shown in Figure 2.11, is given by (2.72). Here we have

$$\Delta\beta_1 = \frac{1}{2}(\pi_{11} + \pi_{12} + \pi_{44})\sigma_1 + \frac{1}{6}(\pi_{11} + 5\pi_{12} - \pi_{44})\sigma_2$$
$$\Delta\beta_2 = \frac{1}{6}(\pi_{11} + 5\pi_{12} - \pi_{44})\sigma_1 + \frac{1}{2}(\pi_{11} + \pi_{12} + \pi_{44})\sigma_2$$
$$\Delta\beta_6 = \frac{1}{3}(\pi_{11} - \pi_{12} + 2\pi_{44})\sigma_6 \qquad (2.80)$$

Substituting (2.80) into (2.78) and (2.72) yields

$$\frac{1}{3}(\pi_{11} - \pi_{12} + 2\pi_{44})(\sigma_1 - \sigma_2) = \pm\frac{\lambda\delta}{\pi d n_0^3}\cos 2\alpha$$
$$\frac{2}{3}(\pi_{11} - \pi_{12} + 2\pi_{44})\sigma_6 = \pm\frac{\lambda\delta}{\pi d n_0^3}\sin 2\alpha$$

and

$$\tan 2\alpha = \frac{2\sigma_6}{\sigma_1 - \sigma_2}. \qquad (2.81)$$

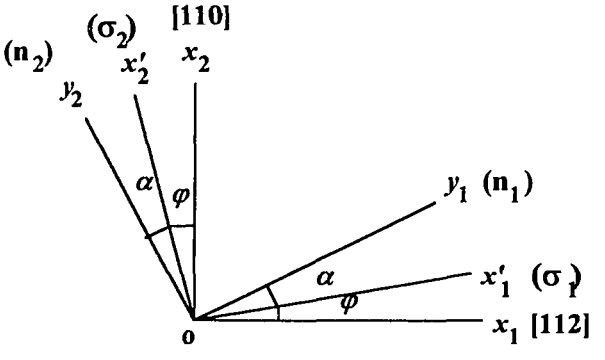

Figure 2.11 Relation between directions of principal stress and principal index when observation made along the $[\bar{1}\bar{1}1]$ direction.

From the assumption that the two principal stresses are in x_1' and x_2' directions, the stress component σ_6 is equal to zero, and the angle α is equal to zero, indicating that the principal axes of the stress ellipse coincide with those of the refractive ellipse. Thus, the principal stresses can be expressed in a simple form:

$$\frac{1}{3}(\pi_{11} - \pi_{12} + 2\pi_{44})(\sigma_1 - \sigma_2) = \pm\frac{\lambda\delta}{\pi d n_0^3} \qquad (2.82)$$

Based on this equation, we can calculate the principal stress difference σ_1-σ_2, with the given values of λ, δ, d, and n_0.

2.4.2.2 Observation Made along any Direction within the [112]-[$\bar{1}$10] Plane The original coordinate axes (x_1, x_2, and x_3) are chosen in the [112], [$\bar{1}$10], and [$\bar{1}\bar{1}$1] directions, as the same as that shown in Figure 2.10. When an observation is made along the x_1' direction, which is within the x_1-x_2 plane, and x_1' and x_1 constitutes an angle of φ, as shown in Figure 2.10. Assume the principal stresses to be in the x_2'-x_3 plane. In the new coordinate system (x_1', x_2', x_3), the central section of the refractive index ellipsoid, normal to the x_1' directions, is expressed by

$$\beta_2 x_2'^2 + \beta_3 x_3^2 + 2\beta_4 x_2' x_3 = 1 \tag{2.83}$$

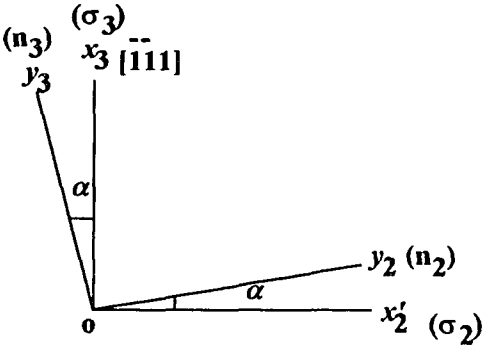

Figure 2.12 Relation between directions of principal stress and principal index when observation made along any direction within the [112]-[$\bar{1}$10] plane.

The angle α between the oscillation direction of the polarized light, y_2 or y_3, and the direction of the principal stress, x_2' or x_3, as shown in Figure 2.12, now becomes

$$\tan 2\alpha = \frac{2\Delta\beta_4}{\Delta\beta_2 - \Delta\beta_3} \tag{2.84}$$

where,

$$\Delta\beta_2 = \frac{1}{2}(\pi_{11}+\pi_{12}+\pi_{44})\sigma_2 + \frac{1}{3}(\pi_{11}+2\pi_{12}-\pi_{44})\sigma_3 - \frac{\sqrt{2}}{3}(\pi_{11}-\pi_{12}-\pi_{44})\cos 3\varphi\ \sigma_4$$

$$\Delta\beta_3 = \frac{1}{3}(\pi_{11}+2\pi_{12}-\pi_{44})\sigma_2 + \frac{1}{3}(\pi_{11}+2\pi_{12}+2\pi_{44})\sigma_3$$

$$\Delta\beta_4 = -\frac{\sqrt{2}}{6}(\pi_{11}-\pi_{12}-\pi_{44})\cos 3\varphi\ \sigma_2 + \frac{1}{3}(2\pi_{11}-2\pi_{12}+\pi_{44})\sigma_4 \qquad (2.85)$$

If the two principal stresses are in the directions of x_2' and x_3, we have $\sigma_4=0$. Thus, from (2.84) and (2.85), we have

$$\frac{1}{6}(\pi_{11}-\pi_{12}+5\pi_{44})\sigma_2 - \pi_{44}\sigma_3 = \pm\frac{\lambda\delta}{\pi d n_0^3}\cos 2\alpha$$

$$-\frac{\sqrt{2}}{3}(\pi_{11}-\pi_{12}-\pi_{44})\cos 3\varphi\ \sigma_2 = \pm\frac{\lambda\delta}{\pi d n_0^3}\sin 2\alpha \qquad (2.86)$$

And the angle α is given by

$$\tan 2\alpha = -\frac{2\sqrt{2}(\pi_{11}-\pi_{12}-\pi_{44})\cos 3\varphi\ \sigma_2}{(\pi_{11}-\pi_{12}+5\pi_{44})\sigma_2 - 6\pi_{44}\sigma_3} \qquad (2.87)$$

From (2.87), the angle α depends on the observation direction φ and the magnitude of the principal stresses. If the observation is made in some special directions such that $\cos 3\varphi=0$, the angle α equals zero. In such situations, the principal axes of the stress ellipse coincide with the principal axes of the refractive index ellipse. When $(\pi_{11}-\pi_{12}+5\pi_{44})\sigma_2=\pm 6\pi_{44}\sigma_3$, the angle α reaches its maximum values 45°.

Generally, three unknown parameters (σ_2, σ_3, and α) can not be solely determined from the two independent equations (2.86) and (2.87). However, under certain practical situations, Eqs.(2.86) and (2.87) can be simplified. For example, for a thin (111) wafer, if observed along its flank side normal to the x_1' direction, the only non-zero stress component is σ_2. Thus, we have

$$\frac{1}{6}(\pi_{11}-\pi_{12}+5\pi_{44})\sigma_2 = \pm\frac{\lambda\delta}{\pi d n_0^3}\cos 2\alpha \qquad (2.88)$$

$$\tan 2\alpha = -2\sqrt{2}(\pi_{11}-\pi_{12}-\pi_{44})\cos 3\varphi\ /(\pi_{11}-\pi_{12}+5\pi_{44}) \qquad (2.89)$$

In such case, the angle α is determined by the observation direction. Figure 2.13 shows the relation between the angle α and the observation direction φ for silicon wafer with (111) when observation is made along its flank side, where the values of π_{11}, π_{12},

and π_{44} from Table 2.1 are used. If k is any integer, it is obvious from Figure 2.13, that when $\varphi=k\pi/3+\pi/6$, *i.e.*, observation is made along the <112> directions, $\alpha=0$. The principal axes of projection ellipse of refractive index ellipsoid are identical with the directions of principal stresses. When $\varphi=k\pi/3$, *i.e.*, observation is made along the <110> direction, the orientation deviation between the projection ellipse of refractive index ellipsoid and the stress ellipse becomes a maximum, *i.e.*, $\alpha = 9.94°$.

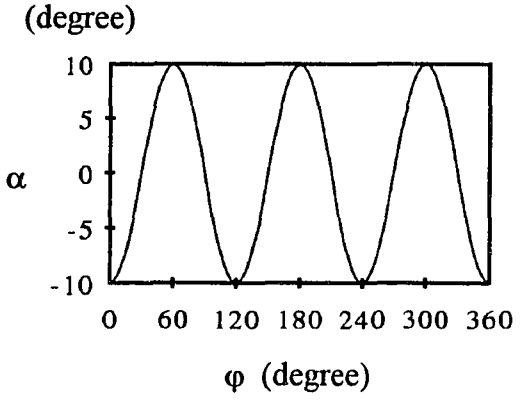

Figure 2.13 The angle α as a function of the observation direction φ for a (111) silicon wafer when observation is made along the flank side.

2.4.3 Application in the [110][$\bar{1}$10][001] Coordinate System

2.4.3.1 Observation Made along the [001] Direction The axes of [110], [$\bar{1}$10], and [001] are chosen as the coordinate axes (x_1, x_2, x_3) of the original coordinate system, as shown in Figure 2.14. Defined a new coordinate system (x_1', x_2', x_3), where, x_1' and x_2' are in the x_1-x_2 plane, and x_1' and x_1 constitute an angle of φ, as shown in Figure 2.13. The central section equation is given as (2.69). The relation between the directions of principal stress and principal refractive index is shown in Figure 2.15. The angle α between the oscillation directions of the two polarized lights and the directions of the two principal stresses is given as (2.72). Here we have

$$\Delta\beta_1 - \Delta\beta_2 = [\pi_{44} + (\pi_{11}-\pi_{12}-\pi_{44})\sin^2 2\varphi](\sigma_1 - \sigma_2) + (\pi_{11}-\pi_{12}-\pi_{44})\sin 4\varphi\,\sigma_6$$

$$\Delta\beta_6 = \frac{1}{4}(\pi_{11}-\pi_{12}-\pi_{44})\sin 4\varphi\,(\sigma_1 - \sigma_2) + [\pi_{44}\sin^2 2\varphi + (\pi_{11}-\pi_{12})\cos^2 2\varphi]\sigma_6 \quad (2.90)$$

If the directions of the two principal stresses are in the directions of x_1' and x_2', we have that $\sigma_6=0$, Eqs. (2.90) are rewritten as

$$\Delta\beta_1 - \Delta\beta_2 = [\pi_{44} + (\pi_{11}-\pi_{12}-\pi_{44})\sin^2 2\varphi](\sigma_1 - \sigma_2) = \pm\frac{\lambda\delta}{\pi d n_0^3}\cos 2\alpha$$

$$2\Delta\beta_6 = \frac{1}{2}(\pi_{11}-\pi_{12}-\pi_{44})\sin 4\varphi](\sigma_1 - \sigma_2) = \pm\frac{\lambda\delta}{\pi d n_0^3}\sin 2\alpha \quad (2.91)$$

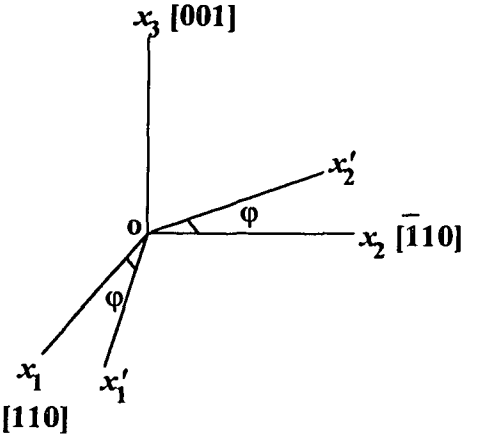

Figure 2.14 Relation between coordinates of (x_1,x_2,x_3) and (x_1',x_2',x_3) in the [110][$\bar{1}$10][001] coordinate system.

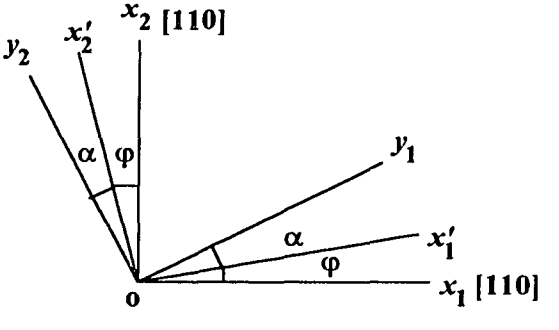

Figure 2.15 Relation between directions of principal stress and principal index when observation made along the [001] direction.

And the angle α is given by

$$\tan 2\alpha = \frac{(\pi_{11} - \pi_{12} - \pi_{44})\sin 4\varphi}{2\pi_{44} + 2(\pi_{11} - \pi_{12} - \pi_{44})\sin^2 2\varphi} \tag{2.92}$$

The angle α can be readily calculated by (2.92) when the principal stress direction φ is known. Figure 2.16 shows the angle α as a function of the principal stress direction φ for a (001) silicon wafer, where the data of π_{11}, π_{12}, and π_{44} from Table 2.1 are used. It is obvious that when φ=0, α=0; and when φ=22.5°, the angle α reaches its maximum 8.3°.

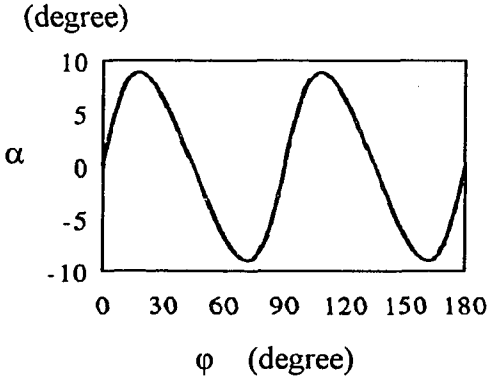

Figure 2.16 The angle α as a function of the principal stress direction φ for a (001) silicon wafer when viewed from the [001] direction.

2.4.3.2 Observation Made along any Direction within the [110]-[$\bar{1}$10] Plane The coordinate systems are chosen as shown in Figure 2.14. Observation is made in the x_1' direction within the x_1-x_2 plane, and x_1' and x_1 constitute an angle of φ, as shown in Figure 2.17. The directions of the two principal stresses are assumed in the x_2' and x_3 directions. In the coordinate system (x_1', x_2', x_3), the central section equation of the refractive index ellipsoid is given in (2.83). Similarly, we have

$$\Delta\beta_2 = [\frac{1}{2}(\pi_{11}+\pi_{12}+\pi_{44}) + \frac{1}{2}(\pi_{11}-\pi_{12}-\pi_{44})\sin^2 2\varphi]\sigma_2 + \pi_{12}\sigma_3$$

$$\Delta\beta_3 = \pi_{12}\sigma_2 + \pi_{11}\sigma_3$$

$$\Delta\beta_4 = \pi_{44}\sigma_4 \tag{2.93}$$

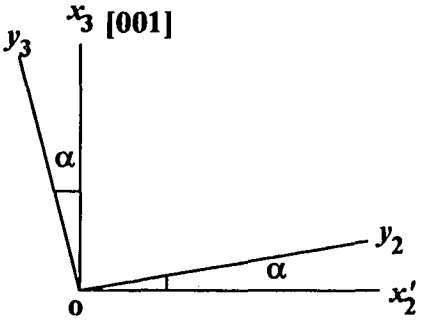

Figure 2.17 Relation between directions of principal stress and principal index when observation made along any direction within the [$\bar{1}$10]-[110] plane.

Since the principal stresses are in the x_2' direction and the x_3 direction, then $\sigma_4=0$, thus

$$\alpha=0 \tag{2.94}$$

and

$$\frac{1}{2}[(\pi_{11}-\pi_{12}+\pi_{44})+(\pi_{11}-\pi_{12}-\pi_{44})\sin^2 2\varphi]\sigma_2-(\pi_{11}-\pi_{12})\sigma_3=\pm\frac{\lambda\delta}{\pi d n_0^3} \tag{2.95}$$

Notice that we are still unable to solve two unknown stresses σ_2 and σ_3 by using (2.95). However, for the thin wafer of (100) plane, when observed from flank side, the only unknown stress is σ_2, which can be calculated by using (2.95), that is

$$\frac{1}{2}[(\pi_{11}-\pi_{12}+\pi_{44}) + (\pi_{11}- \pi_{12}-\pi_{44})\sin^2 2\varphi]\sigma_2 = \pm\frac{\lambda\delta}{\pi d n_0^3} \tag{2.96}$$

2.5. Summary

In this chapter, we study the birefringence in various crystals. The anisotropy of the photoelastic effect in the crystals with cubic symmetry is investigated in detail. The matrix forms of the piezo-optic coefficient tensor are derived for various coordinate configurations. For crystal materials of diamond structure or zincblende structure, in general, the orientation of the stress ellipsoid does not coincide with that of the refractive

index ellipsoid. For a two-dimensional situation, the relationship between the principal axes of the stress ellipsoid and those of the refractive index ellipsoid is analyzed.

In a crystal situation, the stress-optic law of isotropic medium is no longer valid. Instead, we have derived the analytical expressions of the stress-optic law for some commonly used coordinate configurations. In order to derive a stress-optic law in different coordinate configurations, we should know the matrix forms of piezo-optic coefficients in the coordinate configurations. Taking into account the anisotropy of photoelasticity in a cubic crystal, according to the transformation law for fourth-rank tensor in matrix form, we obtain piezo-optic coefficient matrices in the $[110][\bar{1}10][001]$ coordinate system and in the $[112][\bar{1}10][\bar{1}\bar{1}1]$ coordinate system. The discussion presented in this chapter forms the major theoretical part for our research projects of stress study in microelectronic materials with photoelasticity.

CHAPTER 3

METHODOLOGY OF PHOTOELASTIC STRESS ANALYSIS

In photoelastic stress analysis, in order to apply the stress-optic law derived in Chapter 2 to calculate the distributions of the principal stresses, it is necessary to determine the two photoelastic parameters: the *birefringence phase difference* δ and *the birefringence angle* ϕ, with which we can solve for the magnitudes and the directions of the principal stresses. In this chapter, we will discuss some methods of measuring these two parameters. These methods are the Senarmont compensation method, the Fourier analysis method, and the intensity analysis method. We will discuss the measurement arrangements, the principles of operation and the errors for these methods. Finally, in Section 3.4, we will introduce the three-direction observation method of determining the principal stresses from three secondary principal stresses.

3.1 Senarmont Compensation Method

3.1.1 Concept of Operation

In conventional photoelastic experiments, the two parameters δ and ϕ are determined by analyzing the isochromatic lines and the isoclinic lines of photoelastic patterns. However, when applying photoelasticity to microelectronic materials, we are dealing with samples with thickness in the order of $0.5mm$, the birefringence phase difference accumulated through the optical path is typically less than π, which corresponds to the stress less than $10^8 dyn/cm^2$. Therefore, it is necessary to find effective methods to determine the fractional order of isochromatic line. Senarmont compensation [32] is a useful method of determining the birefringence phase difference with a fractional order of isochromatic line.

It has been successfully applied to determine the stress in silicon wafers after various device processes [33][34].

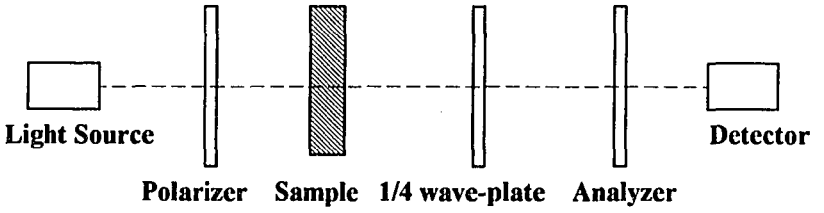

Figure 3.1 Schematic diagram of measurement configuration for Senarmont compensation.

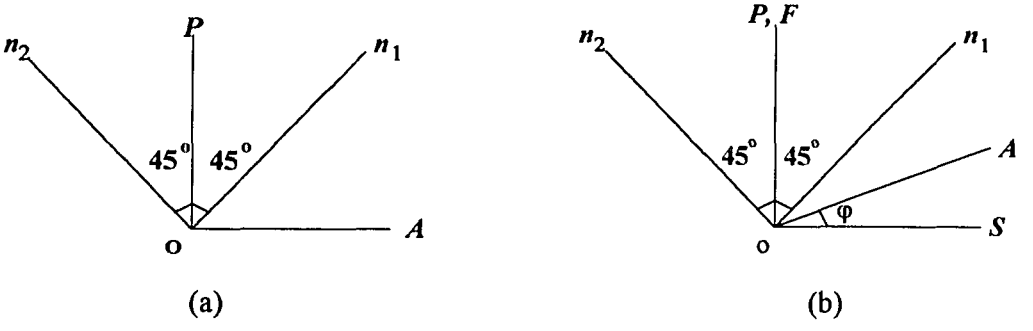

Figure 3.2 Schematic representation the directions of polarization and stresses.

The schematic diagram of measurement configuration of Senarmont compensation is shown in Figure 3.1, which consists of a light source, a polarizer and an analyzer, a sample, a quarter wave-plate and a detector. First, by rotating the aligned polarizer and analyzer together, we can find the principal directions of the refractive index ellipse. When a linearly polarized light beam goes through the sample, the detector output reaches maximum if the polarization direction coincides with one of the principal direction of the

refractive index ellipse. Then the polarization axes of the polarizer P and the analyzer A are made at 45° with respect to the principal refractive index direction of the sample, as shown in Figure 3.2(a). A quarter wave-plate is placed between the sample and the analyzer, with its fast and slow axes parallel to the polarization axes, as shown in Figure 3.2(b). The analyzer is rotated until the nearest n-th order fringe moves to the measured point, as shown in Figure 3.2(b), where φ is the rotated angle, with which we can determine the birefringence phase difference δ.

3.1.2 Principle of Compensation [32]

After transmitted through the polarizer, the monochromatic light becomes linearly polarized:

$$E_p = a_1 \sin\omega t \tag{3.1}$$

When the polarized light arrives at sample, it decomposes into two components along the directions of ε_1 and ε_2:

$$E_1 = E_p \cos 45° = a_2 \sin\omega t$$
$$E_2 = E_p \sin 45° = a_2 \sin\omega t \tag{3.2}$$

where a_2=0.707a_1. After transmitted through the sample, a phase difference δ between E_1 and E_2 will develop, due to presence of stress in the sample:

$$E_1' = a_2 \sin(\omega t - \delta)$$
$$E_2' = a_2 \sin\omega t \tag{3.3}$$

As E_1' and E_2' reach the quarter wave-plate, they will decompose along the fast axis F and the slow axis S. Since the fast axis F of the quarter wave-plate is parallel to the polarization axis of the polarizer P, thus,

$$E_f = E_1' \cos 45° + E_2' \sin 45° = a_3 \sin(\omega t - \delta) + a_3 \sin\omega t$$
$$E_s = E_1' \sin 45° - E_2' \cos 45° = a_3 \sin(\omega t - \delta) - a_3 \sin\omega t \tag{3.4}$$

After transmitted the quarter wave-plate, a phase difference π/2 will be introduced between E_f and E_s:

$$E_f' = a_3\sin(\omega t-\delta+\pi/2) + a_3\sin(\omega t+\pi/2) = a_3\cos(\omega t-\delta) + a_3\cos\omega t$$

$$E_S' = a_3\sin(\omega t-\delta) - a_3\sin\omega t \qquad (3.5)$$

When E_f' and E_S' reach the analyzer A, only their projections along the polarization axis of analyzer A can pass. The composite light beam E_A coming out of the analyzer A is

$$E_A = E_f'\sin\theta + E_S'\cos\varphi = a\cos(\omega t-\delta/2)\sin(\varphi-\delta/2) \qquad (3.6)$$

Thus, the intensity of the transmitted light is

$$I = k\sin^2(\varphi - \delta/2) \qquad (3.7)$$

When

$$\sin(\varphi - \delta/2) = 0, \qquad (3.8)$$

the transmitted light intensity I=0. By rotating the analyzer, the angle φ may be chosen to satisfy this condition, which is called the *compensation angle*. From (3.8), the birefringence phase difference δ is related to the compensation angle φ by

$$\delta = 2n\pi + 2\varphi \qquad (3.9)$$

where n is an integer, which represents the integer part of the order of isochromatic line.

3.1.3 Analysis of Accuracy

When employing the Senarmont compensation method, the major errors of measuring birefringence phase difference may arise from: the error of the polarization angle of polarizer ξ and the error of the retarding phase of the quarter waveplate ζ. In Figure 3.3, the angle between the polarization axis of polarizer and the principal stress is 45°-ξ and the phase retardation of the quarter waveplate is 90°+ζ. The monochromatic light from the polarizer is given by (3.1). After the polarized light travels into sample, it decomposes into two components along the directions of ε_1 and ε_2:

$$E_1 = E_p\cos45° = a_1\sin\omega t\cos(45°-\xi)$$

$$E_2 = E_p\sin45° = a_1\sin\omega t\cos(45°+\xi) \qquad (3.10)$$

After transmitted through the sample, a phase difference δ between E_1 and E_2 will be developed, due to the presence of stress in the sample. Then,

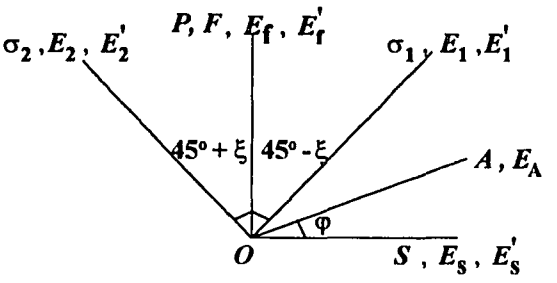

Figure 3.3 Errors of Senarmont compensation.

$$E_1' = a_1 \sin(\omega t + \delta)\cos(45° - \xi)$$

$$E_2' = a_1 \sin\omega t \cos(45° + \xi) \qquad (3.11)$$

As E_1' and E_2' reach the quarter wave-plate, they will decompose along the fast axis F and the slow axis S:

$$E_f = a_1\sin(\omega t + \delta)\cos^2(45° - \xi) + a_1\sin\omega t \cos^2(45° + \xi)$$

$$E_S = a_1\sin\omega t \cos(45° + \xi)\cos(45° - \xi) - a_1 \sin(\omega t + \delta)\cos(45° + \xi)\cos(45° - \xi) \qquad (3.12)$$

After E_f and E_S having passed the quarter wave-plate, a phase difference $\pi/2+\zeta$ is added between E_f and E_S:

$$E_f' = a_1\cos(\omega t + \delta + \zeta)\cos^2(45° - \xi) + a_1\cos(\omega t + \zeta)\cos^2(45° + \xi)$$

$$E_S' = a_1\sin\omega t \cos(45° + \xi)\cos(45° - \xi) - a_1\sin(\omega t + \delta)\cos(45° + \xi)\cos(45° - \xi) \qquad (3.13)$$

When E_f' and E_S' reach the analyzer A, they compose along the polarization axis of the analyzer. The composite light beam E_A coming from analyzer A is

$$E_A = (A_1\sin\varphi + A_2\cos\varphi)\cos\omega t + (B_1\sin\varphi + B_2\cos\varphi)\sin\omega t \qquad (3.14)$$

where,

$$A_1 = a_1[\cos(\delta + \zeta)\cos^2(45° - \xi) + \cos\zeta \cos^2(45° + \xi)]$$

$$B_1 = -a_1[\sin(\delta + \zeta)\cos^2(45° - \xi) + \sin\zeta \cos^2(45° - \xi)]$$

$$A_2 = -a_1\cos\xi \sin\frac{1}{2}\delta \cos\frac{1}{2}\delta$$

$$B_2 = a_1\cos\xi \sin^2\frac{1}{2}\delta \qquad (3.15)$$

The intensity of the transmitted light is

$$I = k^2 [(A_2\cos\varphi + A_1\sin\varphi)^2 + (B_2\cos\varphi + B_1\sin\varphi)^2] \quad (3.16)$$

By letting $dI/d\varphi=0$, it is found that when

$$\tan\varphi = \frac{\cos\zeta\sin\delta + \sin 2\xi\sin\zeta\cos\delta - \sin 2\xi\sin\zeta}{\cos\delta\cos 2\xi + \sin 2\xi\tan 2\xi}, \quad (3.17)$$

the transmitted light intensity reaches its minimum. When there is no error, $\xi=0$, $\zeta=0$, (3.17) becomes

$$\tan\varphi = \tan\delta \quad (3.18)$$

whose solution is the same as (3.9):

$$\delta = 2n\pi + 2\varphi \quad (3.19)$$

If there are errors, $\xi\neq0$ and/or $\zeta\neq0$. By assuming that $\xi=5°$, $\zeta=5°$, and $\varphi=10°$, we can estimate from Eq.(3.17) that the relative error $|\Delta\alpha/\alpha|$ is 2.22%. It is readily shown, from Eq.(3.17), that if $\xi<5°$, $\zeta<5°$, for any value of φ we always have that $|\Delta\delta/\delta|$ is less than 3%; that indicates a high accuracy by employing the Senarmont compensation method to measure birefringence phase difference.

3.2 Fourier Analysis Method

In photoelastic stress analysis of microelectronic materials, we often need to determine fractional order fringe of photoelastic patterns for the whole area of a wafer sample. It is virtually impossible to use the Senarmont compensation method, since the photoelastic parameters $\delta(x,y)$ and $\phi(x,y)$ must be measured through every position (x,y) of the sample. Fourier analysis is a new method developed during this dissertation research. The approach is to use a continuously rotating analyzer to obtain a series of photoelastic patterns of the sample which is followed by Fourier analysis of the measured images to determine photoelastic parameters $\delta(x,y)$ and $\phi(x,y)$. In this section, we discuss the principle of the Fourier analysis method, present an example of its application, and analyze the accuracy.

3.2.1 Linear Retarder

Since a stressed transparent material exhibits a birefringence effect, it is equivalent to a linear retarder. When a polarized light beam with Jones vector $(A_1, B_1)^T$ is incident upon the linear retarder, the two polarized components A_1 and B_1 will decompose along the ξ and η axes, as shown in Figure 3.4. The Jones vector becomes [35]

$$\begin{pmatrix} A_\xi \\ B_\eta \end{pmatrix} = \begin{pmatrix} \cos\phi & \sin\phi \\ -\sin\phi & \cos\phi \end{pmatrix} \begin{pmatrix} A_1 \\ B_1 \end{pmatrix} \tag{3.20}$$

where A_ξ and B_η are the components of the polarized lights along ξ and η axes, respectively. After transmitting through sample, B_η has a retarded phase δ relative to A_ξ,

$$\begin{pmatrix} A'_\xi \\ B'_\eta \end{pmatrix} = \begin{pmatrix} 1 & 0 \\ 0 & e^{i\delta} \end{pmatrix} \begin{pmatrix} A_\xi \\ B\eta \end{pmatrix} \tag{3.21}$$

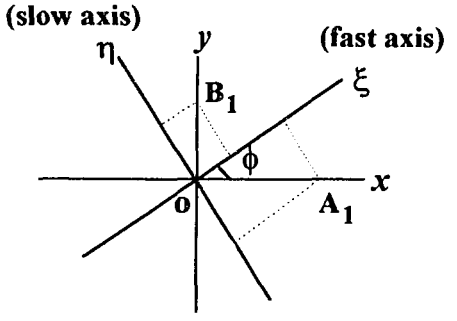

Figure 3.4 Schematic representation of the linear retarder.

The transmitted components of A'_ξ and B'_η can be expressed in terms of components A_2 and B_2 along the reference axes x and y, that is,

$$\begin{pmatrix} A_2 \\ B_2 \end{pmatrix} = \begin{pmatrix} \cos\phi & -\sin\phi \\ \sin\phi & \cos\phi \end{pmatrix} \begin{pmatrix} A'_\xi \\ B'_\eta \end{pmatrix} = R \begin{pmatrix} A_1 \\ B_1 \end{pmatrix} \tag{3.22}$$

where the Jones matrix of the linear retarder is given by

$$R = \begin{bmatrix} a_{11} & a_{12} \\ a_{21} & a_{22} \end{bmatrix} = \begin{pmatrix} e^{i\delta}\cos^2\phi + \sin^2\phi & (e^{i\delta}-1)\sin\phi\cos\phi \\ (e^{i\delta}-1)\sin\phi\cos\phi & e^{i\delta}\sin^2\phi + \cos^2\phi \end{pmatrix} \tag{3.23}$$

Eq.(3.23) is a useful expression for a linear retarder, which describes the stress state at a point of the stressed sample. The parameter δ is related to the magnitude of the difference of the principal stresses by the stress-optic law of (2.78), while the parameter ϕ is related to the direction of the principal refractive index n_1 by (2.79).

3.2.2 Principle of Measurement

After the linearly polarized light P passes through the sample or the retarder R, it transmits through the analyzer A set at angle φ as shown in Figure 3.5. The emerging light, or the signal S to be detected, is [36]

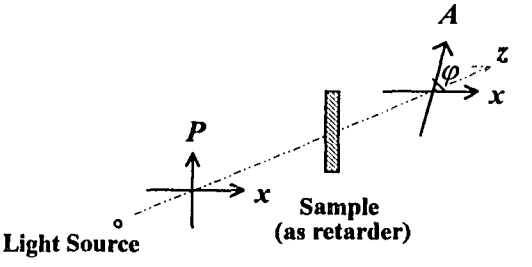

Figure 3.5 Schematic diagram of the optic arrangement for Fourier analysis.

$$S = A(\varphi)\, R\, P \tag{3.24}$$

where the Jones vector P of the transmitted light from polarizer and the Jones matrix $A(\varphi)$ for the analyzer are

$$P = \begin{bmatrix} 0 \\ 1 \end{bmatrix} \tag{3.25}$$

$$A(\varphi) = \begin{bmatrix} \cos^2\varphi & \frac{1}{2}\sin 2\varphi \\ \frac{1}{2}\sin 2\varphi & \sin^2\varphi \end{bmatrix} \tag{3.26}$$

Apparently, the Jones vector S can be rewritten as

$$S=\begin{bmatrix} a_{12}\cos^2\varphi+\frac{1}{2}a_{22}\sin 2\varphi \\ \frac{1}{2}a_{12}\sin 2\varphi+a_{22}\sin^2\varphi \end{bmatrix} \tag{3.27}$$

A detector is provided to measure the intensity I of the transmitted light S,

$$I=S^TS = a(\cos^4\varphi+\frac{1}{4}\sin^2 2\varphi)+\frac{1}{2}e\sin 2\varphi+d(\sin^4\varphi+\frac{1}{4}\sin^2 2\varphi) \tag{3.28}$$

where,

$$a=a_{12}^{*}a_{12}$$
$$e=a_{22}^{*}a_{12}+a_{22}a_{12}^{*}$$
$$d=a_{22}^{*}a_{22} \tag{3.29}$$

By multiplying both sides of (3.28) with cosφ, and integrating them from 0 to 2π, yields

$$\int_0^{2\pi} I\cos 2\varphi d\varphi=\frac{\pi}{2}f \tag{3.30}$$

where f=a-d. Similarly, by multiplying both sides of (3.28) with sin2φ and integrating them from 0 to 2π, we have

$$\int_0^{2\pi} I\sin 2\varphi d\varphi=\frac{\pi}{2}e \tag{3.31}$$

Based on the theory of Fourier transform [37], coefficients e and f can be respectively related to the imaginary part and the real part of the second term of the Fourier transform of I, that is

$$f=4\,Re\{F_2(I)\}$$
$$e=-4\,Im\{F_2(I)\} \tag{3.32}$$

On the other hand, by using Eqs.(3.23), (3.29), the coefficients e and f are expressed as

$$e=\frac{1}{2}\sin 4\phi(\cos\delta-1)$$
$$f=-\frac{1}{2}-\frac{1}{2}\cos 4\phi-\frac{1}{2}\cos\delta(1-\cos 4\phi) \tag{3.33}$$

Once the values of f and e are obtained from (3.32), the photoelastic parameters ϕ and δ can be solved based on (3.33):

$$\phi = 0.5\arctan(-\frac{1+f}{e})$$

$$\delta = \arccos(\frac{\sin 4\phi + 2e}{\sin 4\phi}) \qquad (3.34)$$

3.2.3 Example of Application

A (111) oriented silicon wafer sample is used to illustrate the application of the method. The sample, with size of $8mm \times 10mm$ and thickness of $400\mu m$, is covered with thermally grown SiO_2 thin films of thickness $1\mu m$ on the both surfaces. For simplicity, we measure a point in central region of the sample. Polarized light is incident in the normal direction of the wafer's surface. The intensity of the transmitted light from the analyzer is measured for every 2° of the analyzer azimuth angle φ. A curve of intensity of transmitted light as a function of rotated angle of the analyzer is obtained, as shown in Figure 3.6. The Fourier transform is performed for the measured data. The values of ϕ and δ are obtained as ϕ =16.39° and δ=6.36°.

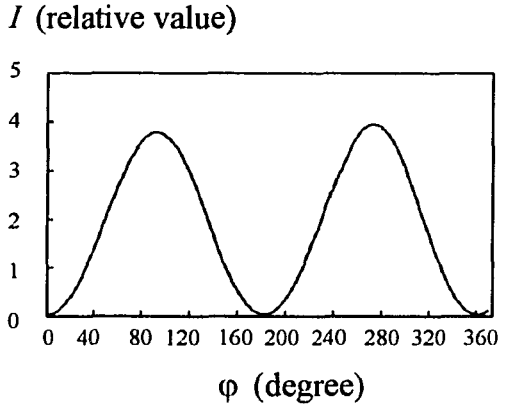

Figure 3.6 Transmitted light intensity as a function of the analyzer azimuth angle.

For the (111) wafer, since light travels in the <111> directions, the refractive index ellipsoid coincides with the stress ellipsoid, and the principal stress directions coincide

with the principal refractive index directions, described by the parameter ϕ, which expresses the angle between the reference axis x and the principal stress σ_1. By using the values of piezo-optic coefficient for silicon in Table 2.1, and putting λ=1.15μm, n_0=3.52, and d=400μm into the stress-optic law given by (2.82), the magnitude of the principal stress difference $(\sigma_1 - \sigma_2)$ is calculated as $3.2\times10^7 dyn/cm^2$.

3.2.4 Analysis of Accuracy

The principal source of error when employing the Fourier analysis method is due to stray light produced by internal reflection [38]. Some of the light reflected in the reverse direction from one surface is again reflected on meeting a second surface such as that of the polarizer, the sample, or other optic elements. The net effect of the two reflections at the two surfaces of an optical element is to return some of the light along its original path. Let the actual intensity I' be the summation of the intensity of stray light I_{stray} and the intensity of polarized light due to the signal I_{signal}:

$$I' = I_{signal} + I_{stray} = I_{signal} + rI_{signal} \tag{3.35}$$

where r is the stray light factor ($0<r<1$). Thus, f and e of (3.34) will become

$$\begin{aligned} f' &= f(1-r) \\ e' &= e(1-r) \end{aligned} \tag{3.36}$$

The measured photoelastic parameters are given by

$$\begin{aligned} \phi' &= 0.5\arctan\left[-\frac{1+(1-r)f}{(1-r)e}\right] \\ \delta' &= \arccos\left[\frac{\sin 4\theta' + 2(1-r)e}{\sin 4\theta'}\right] \end{aligned} \tag{3.37}$$

The errors of ϕ and δ are given by

$$\begin{aligned} \Delta\phi &= \phi' - \phi = 0.5\arctan\left[-\frac{1+(1-r)f}{(1-r)^{-1}e}\right] - 0.5\arctan\left(-\frac{1+f}{e}\right) \\ \Delta\delta &= \delta' - \delta = \arccos\left[\frac{\sin 4\phi' + 2(1-r)e}{\sin 4\phi'}\right] - \arccos\left(\frac{\sin 4\phi + 2e}{\sin 4\phi}\right) \end{aligned} \tag{3.38}$$

For various values of ϕ and δ, the error $\Delta\delta$ is calculated as shown in Figure 3.7, by assuming r=0.01. For a given ϕ, $\Delta\delta$ increases rapidly when δ becomes small. The dash line in the figure indicates where $\Delta\delta=\delta$, that gives the limitation of accuracy of measuring photoelastic parameter δ. From Figure 3.7, it is found for various ϕ that $\Delta\delta=\delta$ occurs at $\delta \approx 4.5°$. For a silicon sample with thickness of 500μm, this represents stress error of about $1.8\times10^7 dyn/cm^2$ which would be acceptable for most applications. Figure 3.8 shows the dependence of minimum detectable birefringence phase difference upon the stray light factor r, assuming ϕ =20°. When r=0.05, $\Delta\delta=\delta$ occurs at $\delta\approx10°$.

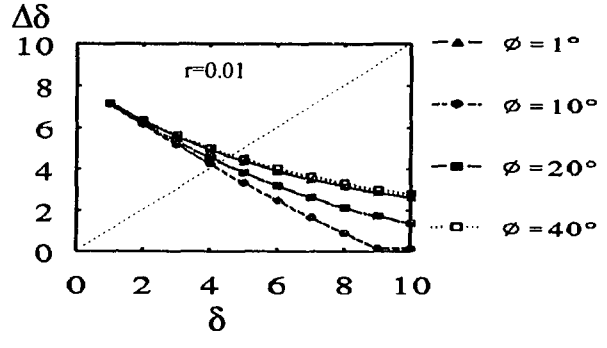

Figure 3.7 Error of δ for different δ and ϕ (the units are degree).

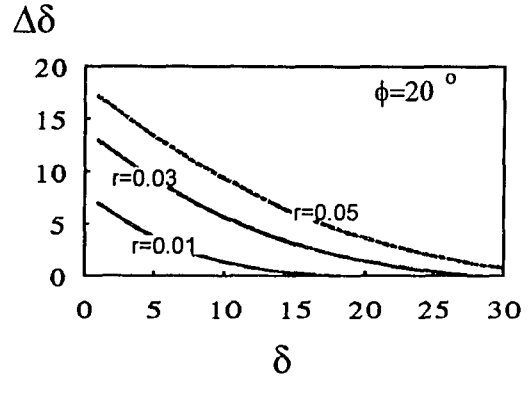

Figure 3.8 Error of δ for different δ and r (the units are degree).

The finite dynamic range of the detector imposes another limitation on the measurement accuracy when employing the Fourier analysis method. To measure the photoelastic parameters effectively, the minimum detectable intensity of the detector should not be higher than the minimum intensity of the light emitting from the analyzer. By using trigonometric identities, (3.28) can be rewritten as

$$I = \left(\frac{a}{2}+\frac{d}{2}\right) + \left(\frac{a}{2}-\frac{d}{2}\right)\cos 2\varphi + \frac{e}{2}\sin 2\varphi \tag{3.39}$$

By letting $\partial I/\partial\varphi=0$, we can solve for the angle φ for which we obtain the minimum emitting light intensity:

$$\tan\varphi = \frac{e}{a-d} \tag{3.40}$$

Thus, the minimum intensity I_{min} is given by

$$I_{min} = \frac{1}{2}(a+d) + \frac{1}{2}\sqrt{e^2+(a-d)^2} \tag{3.41}$$

Based on (3.41), we can calculate the relationship between I_{min} and the photoelastic parameters (δ and ϕ) as shown in Figure 3.9, where I_{min} is normalized to one; transverse axis stands for $\delta = \phi$ (in degree). For $\delta=\phi=5°$, we have $I_{min}=5.73\times10^{-5}$. For $\delta=\phi=10°$, we have $I_{min}=8.83\times10^{-4}$.

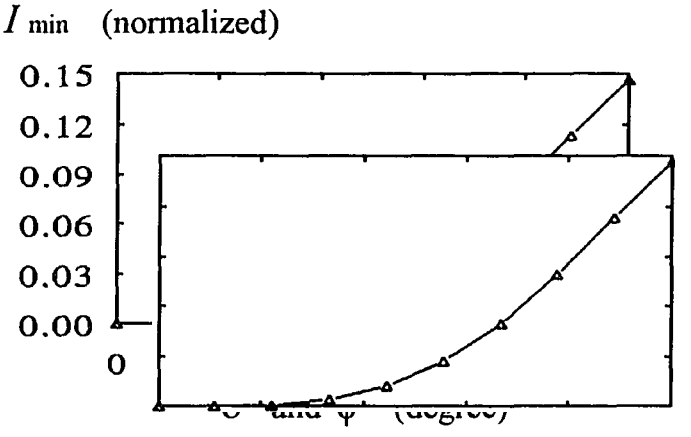

Figure 3.9 Relationship between I_{min} and the photoelastic parameters (δ and ϕ).

To ensure the minimum detectable intensity of the detector lower than the minimum intensity I_{min}, we should choose the detector with a high enough dynamic range. Assume that x is the bits of the digital signals, x should satisfy the following relation:

$$2^{-x} < I_{min} \tag{3.42}$$

Figure 3.10 shows the relationship between the minimum detectable photoelastic parameters (δ and ϕ) and the required bits of the detector. It is obvious that if we wish to detect a minimum photoelastic parameters $\delta=\phi=5°$ (for a silicon sample of thickness 500μ *m*, it corresponds to the stress of about $2.0\times10^7 dyn/cm^2$), the dynamic range of the detector should be higher than 14 bits. For a detector with dynamic range of 8 bits, the minimum detectable photoelastic parameters are about $\delta=\phi=15°$ (for a silicon sample of thickness 500μm, it corresponds to the stress of about $6.0\times10^7 dyn/cm^2$).

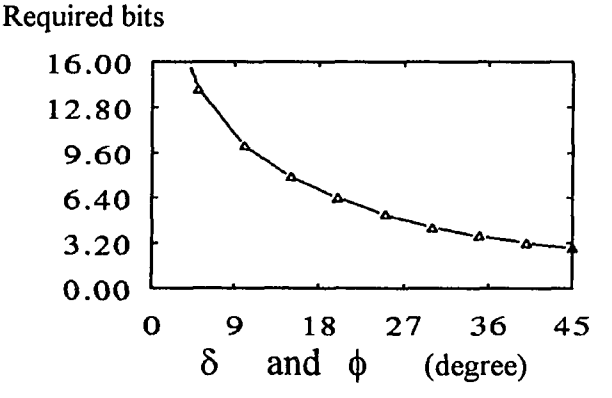

Figure 3.10 Relation between the minimum detectable photoelastic parameters (δ and ϕ) and the required bits of the detector.

The results obtained experimentally illustrate the system's ability to measure accurately the state of polarization of a beam of light. As long as we have a detector with a dynamic range of 16 bits, it is possible to reach the limit of stray light due to internal reflection, (if r=0.01, the minimum detectable stress is about $1.8\times10^7 dyn/cm^2$). Besides, because of the averaging effect of the Fourier transform the method can greatly reduce the

random error when measuring the intensity of the transmitted light. Also since it does not depend on a certain azimuth angle of the analyzer, the method is not related with the error of the azimuth angle of the analyzer. With advanced image sensor and computer techniques, it is possible for this method to become a powerful means to perform automatic analysis of stress distribution for various microelectronic materials and device structures.

3.3 Intensity Analysis Method

3.3.1 Principle of Compensation

Under a dark, linearly polarized field, as shown in Figure 3.11(a), where ϕ is the angle between the direction of the principal refractive index n_1 and the reference axis x, the intensity of light emitted from analyzer is expressed as [39]

$$I_1 = I_0 \sin^2 2\phi \sin^2 \frac{\delta}{2} \tag{3.43}$$

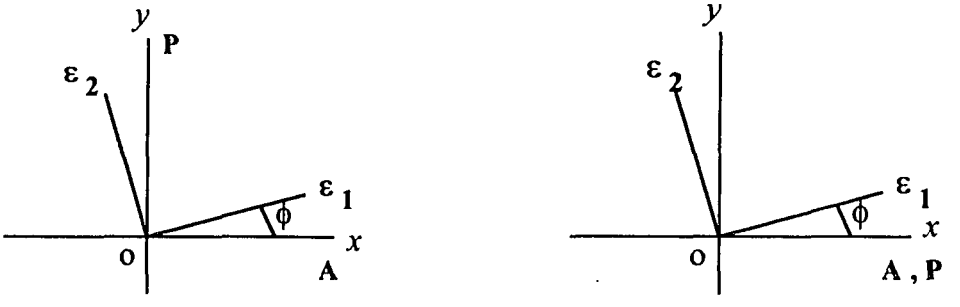

(a) (b)

Figure 3.11 Schematic representation of the intensity analysis method.

where δ is the birefringence phase difference. By rotating the polarizer P such that the polarization axes of the polarizer and the analyzer coincide with each other, we obtain a

bright, linearly polarized field, as shown in Figure 3.11(b). The emitting light from the analyzer is given by [39]

$$I_2 = I_0\,(1\text{-}\sin^2 2\phi\,\sin^2\tfrac{\delta}{2}) \tag{3.44}$$

The constant I_0 in (3.43) and (3.44) is expressed by

$$I_0 = I_1 + I_2 \tag{3.45}$$

Then simultaneously rotating polarizer and analyzer by 45°, the directions of polarization axes of the polarizer and the analyzer are shown in Figure 3.12(a). In a dark, linearly polarized field, as shown in Figure 3.12(a), the transmitted light intensity is

$$I'_1 = I'_0\cos^2 2\phi\,\sin^2\tfrac{\delta}{2} \tag{3.46}$$

Similarly, in a bright, linearly polarized field, as shown in Figure 3.12(b), the transmitted light intensity is

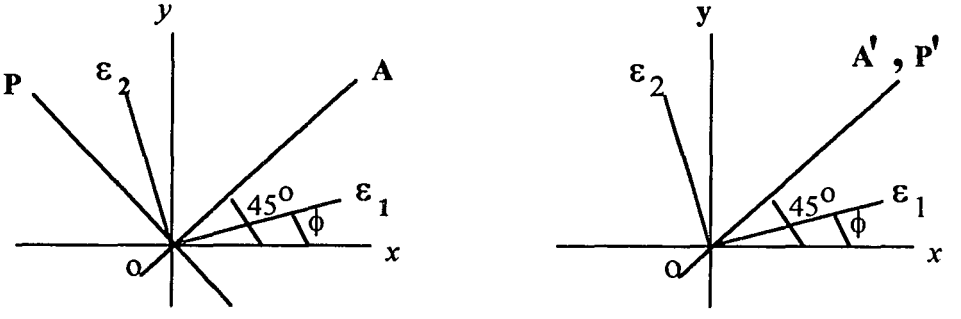

Figure 3.12 Schematic representation of improved photometry compensation after polarized field is rotated by 45°.

$$I'_2 = I'_0(1\text{-}\cos^2 2\phi\,\sin^2\tfrac{\delta}{2}) \tag{3.47}$$

And from (3.46) and (3.47), we have

$$I'_0 = I'_1 + I'_2 \tag{3.48}$$

From (3.43) and (3.46), we can obtain the birefringence phase difference δ,

$$\cos\delta = 1\text{-}\,2\left(\frac{I_1}{I_0}+\frac{I'_1}{I'_0}\right) \tag{3.49}$$

and determine the angle ϕ between principal refractive index n_1 and reference axis x:

$$\tan^2 2\phi = (\frac{I_1}{I_0}) / (\frac{I_1}{I_0}) \tag{3.50}$$

3.3.2 Analysis of Accuracy

There are two principal sources of error when employing the intensity analysis method. The first of these: error of polarization angle of polarizer or analyzer ξ, and non-zero of extinction ratio of polarizers. In dark, linearly polarized light field, as shown in Figure 3.13, due to the two factors above, the angle between polarization axes of polarizer and analyzer is 90°+ξ; the extinction ratio of polarizer and analyzer is ζ.

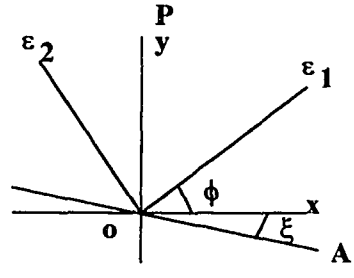

Figure 3.13 Error of the intensity analysis method.

The two components of monochromatic light emitting from the polarizer are

$$E_y = a \sin\omega t$$

$$E_x = a\zeta \sin\omega t \tag{3.51}$$

where a is a constant. After they travel into sample, these two components of light will decompose along the directions of the principal refractive indices:

$$E_1 = E_y \sin\phi + E_x \cos\phi = a \sin \omega t \, (\sin\phi + \zeta\cos\phi)$$

$$E_2 = E_y \cos\phi - E_x \sin\phi = a \sin \omega t \, (\cos\phi - \zeta\sin\phi) \tag{3.52}$$

After they are transmitted through the sample, a phase difference δ between E_1 and E_2 will develop, due to the presence of stress in the sample. Hence,

$$E_1' = a \sin(\omega t + \delta)(\sin\phi + \zeta\cos\phi)$$

$$E_2' = a \sin \omega t (\cos\phi - \zeta\sin\phi) \quad (3.53)$$

As E_1' and E_2' reach analyzer A, they compose along the polarization axis of the analyzer A. The composite light beam E_A coming from analyzer A is

$$\begin{aligned} E_A &= E_1' \cos(\phi + \xi) - E_2' \sin(\phi + \xi) \\ &= a \sin \omega t [\cos\delta (\sin\phi + \zeta\cos\phi)\cos(\phi+ \xi) - (\cos\phi - \zeta\sin\phi)\sin(\phi + \xi)] \\ &\quad + a \cos\omega t \sin\delta (\sin\phi + \zeta\cos\phi)\cos(\phi + \xi) \end{aligned} \quad (3.54)$$

The intensity of light emitting from the analyzer is given by

$$\begin{aligned} I_1 = k^2 \{ & [\cos\delta (\sin\phi + \zeta\cos\phi)\cos(\phi + \xi) - (\cos\phi - \zeta\sin\phi)\sin(\phi + \xi)]^2 \\ & + [\cos\omega t \sin\delta (\sin\phi + \zeta\cos\phi)\cos(\phi + \xi)]^2 \} \end{aligned} \quad (3.55)$$

When $\xi=1°$ and $\zeta=10^{-4}$, $\phi=0$ and $\delta=0$, we obtain

$$I_1 = k^2 (10^{-4}\cos 1° - \sin 1°)^2 = 3.011\times10^{-4} k^2 \quad (3.56)$$

By assuming $I_1' = I_1$ and $I_2' = I_2$, from (3.49) we can estimate the error

$$\cos\Delta\delta = 1 - 4 I_1 = 0.9987965 \quad (3.57)$$

Thus, $\Delta\delta=2.8°$. For a silicon sample of thickness $500\mu m$, this corresponds to a value of stress of about $1.1\times10^7 dyn/cm^2$.

The second major source of error is due to stray light produced by internal reflection, described in previous section. With incident linearly polarized light, extinction conditions exist when $\delta=n\pi$, n being zero or any integer. Let the actual minimum intensity transmitted be rI. The corresponding maximum intensity is $(1-r)I$, hence, the error can be estimated from (3.49):

$$\cos\Delta\delta = 1-2\left(\frac{rI}{rI+(1-r)I} + \frac{rI'}{rI'+(1-r)I'}\right) = 1- 4r \quad (3.58)$$

When $r=0.01$, $\Delta\delta\cong16.3°$. For a silicon sample of thickness $500\mu m$, this corresponds to the minimum detectable stress of about $6.5\times10^7 dyn/cm^2$. The minimum detectable intensity imposes a requirement on the dynamic range of the detector. Since the major limitation on the detection sensitivity is the stray light describe above, the dynamic range of the detector

may be chosen to reach that limit. For r=0.01, the dynamic range is $(1-r)/r$=99, hence, a detector with 8-bit dynamic range could meet this requirement. It is seen that the intensity analysis method has a lower accuracy than the Fourier analysis method. However, since the intensity analysis method is simpler in operation, it will be useful in many applications which do not demand a very high accuracy.

3.4 Three-Direction Observation Method

3.4.1 Principle of Operation

In order to enhance light path difference caused by stress, light incidence and observation from the flank of the wafer sample are adopted. Stresses in a wafer can be considered only within x-y plane, as shown in Figure 3.14(a). However, when a linearly polarized light passes through a three-dimensional sample, the birefringence phase difference δ is proportional to the difference of *secondary principal stresses*, which are the projections of the principal stresses on the sample surface which is perpendicular to the incident light. Therefore, by applying the stress-optic law, we can only obtain the difference of secondary principal stresses. In this dissertation, we propose the *three-direction observation method* to determine the direction and magnitude of principal stresses from three secondary principal stresses measured for a wafer sample. Figure 3.14(b) shows schematic representation of the three observation directions (x, x' and y) for a wafer sample.

For two-dimensional stress state in x-y plane, second-rank stress tensor can be expressed with three components: σ_{xx}, σ_{xy}, and σ_{yy}. When light travels along the x axis, stresses σ_{xx} and σ_{xy} do not cause an optical effect. Stress σ_{yy} can be calculated by [10]

$$\sigma_{yy} = m_1 \frac{\lambda}{C_1 d_1} \tag{3.59}$$

where m_1 is the fringe order of isochromatic line, C_1 the relative stress-optic coefficient in this direction, d_1 the optical path in the x direction, and λ the light wavelength.

Similarly, when observation is made along the y direction, we have

$$\sigma_{xx} = m_2 \frac{\lambda}{C_2 d_2} \tag{3.60}$$

where m_2 is the fringe order of isochromatic line in this case, C_2 the relative stress-optic coefficient in this direction, and d_2 the optical path in y direction.

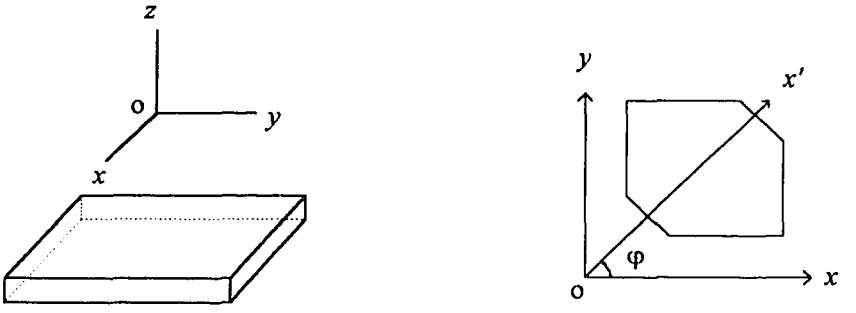

(a) (b)

Figure 3.14 Schematic representation of three observation directions.

To obtain shear stress σ_{xy}, it is necessary to make the third observation in the x' direction, which intersects the x axis with an angle φ. Assuming that the original coordinate system is rotated around the z axis in the x-y plane, it is readily shown that

$$\sigma_{xy} = \frac{\sigma_{xx}}{2}\tan\varphi + \frac{\sigma_{yy}}{2}\cot\varphi - \frac{\sigma'_{yy}}{\sin 2\varphi} \tag{3.61}$$

where the stresses σ_{xx} and σ_{yy} are determined by Eqs.(3.60) and (3.59), and σ'_{yy} can be obtained from an observation along the x' direction:

$$\sigma'_{yy} = m' \frac{\lambda}{C' d'} \tag{3.62}$$

where m' is the fringe order of the isochromatic line observed from the x' direction, C' the relative stress-optic coefficient when observation is made along the x' direction, and d' the optical path in the x' direction. Finally, the magnitudes and directions of the principal stresses σ_1 and σ_2 can be determined by[10]:

$$\sigma_1 = \frac{\sigma_{xx}+\sigma_{yy}}{2} + [(\frac{\sigma_{xx}-\sigma_{yy}}{2})^2 + \sigma_{xy}{}^2]^{1/2}$$
$$\sigma_2 = \frac{\sigma_{xx}+\sigma_{yy}}{2} - [(\frac{\sigma_{xx}-\sigma_{yy}}{2})^2 + \sigma_{xy}{}^2]^{1/2}$$
$$\tan 2\theta = -\frac{2\sigma_{xy}}{\sigma_{xx}-\sigma_{yy}} \tag{3.63}$$

where θ is the angle between the principal stress σ_1 and the positive direction of the x axis.

3.4.2 Application

As the application of the three-direction observation method, we determine the directions of the principal stresses in (001) and (111) silicon wafers with thickness 200~480μm. For a (001) oriented wafer the three observations are [110], [$\bar{1}$10], and [010], as shown in Figure 3.15(a). A (001) wafer is first prepared by cutting it along <110> directions to form a 12mm×12mm square. Then the third pair of parallel observation windows are made in the [010] and [0$\bar{1}$0] orientation, at 45° with respect to the [110] direction. For (111) wafers, in addition to the [1$\bar{1}$0] and [11$\bar{2}$] directions, the third observation direction is at 45° with respect to the [1$\bar{1}$0] axis as shown in Figure 3.15(b). Observations are made along the three directions to obtain three values of fringe order m_1, m_2, and m'. Then the directions and the magnitudes of the principal stresses can be calculated by using Eqs. (3.59)~(3.63).

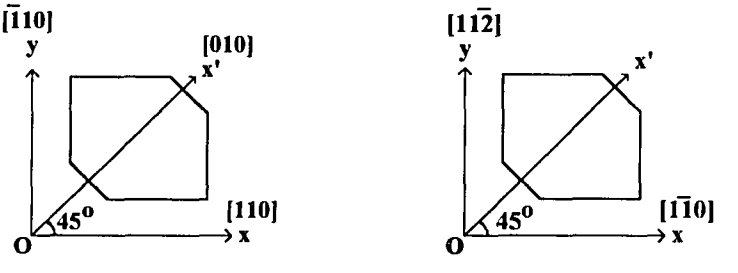

(a) (001) wafer (b) (111) wafer

Figure 3.15 Observation directions for (001) and (111) wafers.

Measurement and analysis indicate that in (001) wafers after oxidation or grinding secondary principal stresses observed along [110] (x-axis positive direction) and along $[\bar{1}10]$ (y-axis direction) are nearly equal, and the principal stress σ_1 orients itself at about 38°~44° with respect to the [110] direction (x-axis positive direction). In other words, the directions of principal stresses are about in the [010] and $[\bar{1}00]$ directions, as shown in Figure 3.16(a). It follows that the orientation of the principal stress is related to the symmetry of silicon wafer's crystal structure. For (111) wafers after grinding or diffusion, the direction of the principal stress σ_1 is at 28°~33° with respect to the x-axis, which is in the $[1\bar{1}0]$ direction. As shown in Figure 3.16(b), the directions of the two principal stresses σ_1 and σ_2 are almost in the $[1\bar{2}1]$ and $[10\bar{1}]$ directions. From results of measurements on the (111) wafers it is found that the secondary principal stresses in the three observation directions are almost equal. The stress ellipse in (111) plane almost becomes a circle. In such case, it is difficult to discriminate the directions of principal stresses. However, the secondary principal stress observed from an arbitrary direction can be considered as an approximation of principal stress.

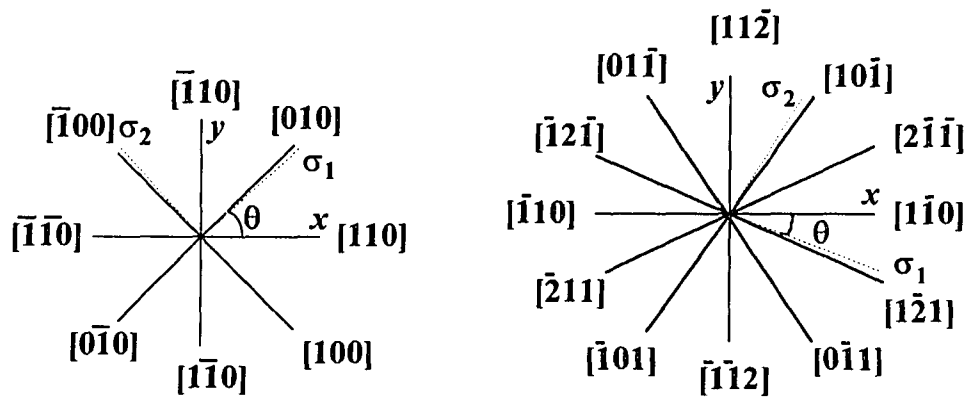

(a) (001) wafer

(b) (111) wafer

Figure 3.16 Orientation of principal stresses determined with three-direction observation.

3.5 Summary

The Senarmont compensation method is effective in precisely determining birefringence phase difference at a measured point of a sample. But it is basically a point-by-point measurement method. It is required to make compensation for each measured point. Therefore, while the Senarmont compensation method is useful to measure birefringence phase difference at certain points of a sample, it is not suitable for automated measurements over the entire area of a wafer sample.

In order to improve efficiency, we explored two methods, the Fourier analysis method and the intensity analysis method. The common advantage of these two methods over the Senarmont compensation method is that they do not require making compensation for each measured point by rotating the analyzer. Hence, we may apply imaging techniques to acquire a photoelastic pattern over the whole sample area at one time. By analyzing the photoelastic patterns, we can determine the stress distribution over the whole sample. By comparison, the Fourier analysis method has a higher accuracy of measuring the birefringence phase difference and better immunity to noise than the intensity analysis method. With a high dynamical range *CCD* camera, the Fourier analysis method is expected to apply in the situation where a high sensitivity and accuracy is required. The intensity analysis method, on the other hand, does not impose a high demand on the performance of a *CCD* camera, and provides us a moderate accuracy.

In a wafer, the stresses normal to its surface are zero. The stresses in a wafer are planar parallel to its surface. When observing from the flank of a wafer, the stresses we measured are not the principal stresses but the secondary principal stresses. We developed the three-direction observation method to determine the directions and the magnitudes of the principal stresses from three secondary principal stresses. This method requires three pairs of parallel observation windows. Three relative stress-optic coefficients along three observation directions must be calculated for the approciate geometrical configurations.

CHAPTER 4

PHOTOELASTIC STRESS MEASUREMENT SYSTEM

On the basis of the theory and methodology of photoelasticity discussed in previous chapters, we will discuss in this chapter the photoelastic systems we have built according to practical requirements. We will discuss the basic considerations of constructing a measurement system and the selection of optical elements, and describe the sensitivity of the measurement system.

4.1 Basic Consideration

4.1.1 System Arrangement

We have set up two types of arrangements of photoelastic stress measurement systems: a *point-by-point measurement system*, which is used to measure one point of the sample at one time; and a *CCD detection system*, which is employed to measure the entire sample. The schematic diagram of the basic point-by-point measurement configuration is shown in Figure 4.1. The system basically consists of an infrared source (typically a 1.15μm HeNe laser), a polarizer (when using a polarized laser source, this polarizer is omitted), an analyzer, and an infrared detector. The system also has a mechanism enabling the sample, the polarizer, and the analyzer to rotate through 360°, individually. A light beam emitting from its source passes through a polarizer and becomes linearly polarized. After transmitted through the sample, it is decomposed into the two components in the principal directions of the refractive index ellipse. Since two components of linearly polarized light pass through the sample with different velocities, a phase difference δ will be accumulated while the two polarized plane waves go through the sample. After these two beams pass through an analyzer, birefringence interference will be detected by a photodetector.

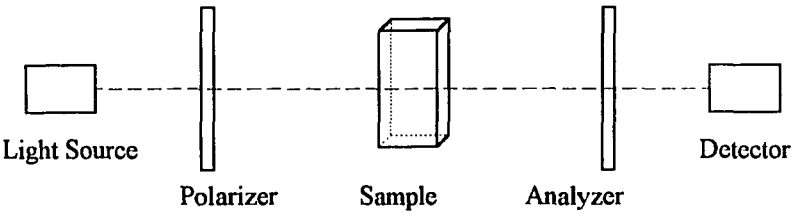

Figure 4.1 Schematic diagram of measurement configuration.

The second part of the system is data acquisition and processing. It detects, samples and digitizes the emerging light intensity at discrete angular positions of the analyzer and passes this information onto a computer. The detector may be a photomultiplier, with a high sensitivity and a wide responsibility from 0.3μm to 1.2μm. A lock-in amplifier is used to amplify the input signal and to generate an output voltage in range of 0 to 5V. A digital voltmeter with 5.5 decimal digits is employed to convert analog signal into digital signal for digital processing. A computer is used to store and to process the acquired data.

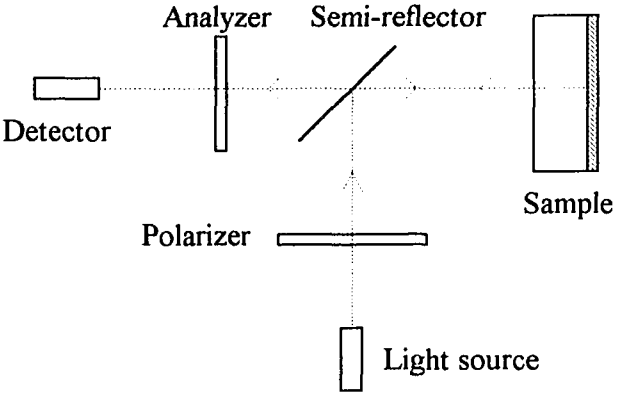

Figure 4.2 Schematical diagram of the reflection photoelastic system.

When measuring the stress in a wafer covered with an opaque, thin metal film on one side, we may employ the reflection photoelastic system, as shown in Figure 4.2. An incident ray transmits through the sample and reflects on the surface of the thin metal film. In this way we can measure the average stress of the light path in the transparent wafer. An additional advantage of the reflection arrangement is that it doubles the measurement sensitivity since the beam travels through the wafer twice and hence the light path is doubled.

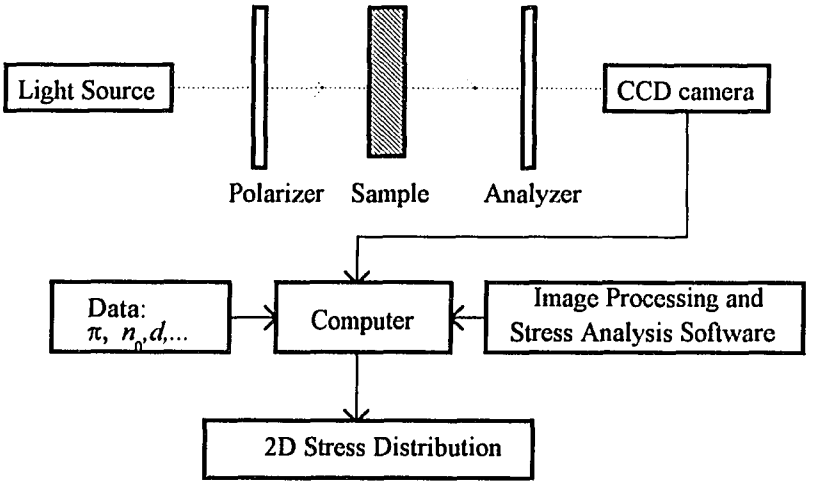

Figure 4.3 Schematic diagram of a *CCD* detection system.

Development of the image sensing and computer techniques makes it possible to automatically survey the stress state over the whole area of a sample in real-time. Instead of using a photomultiplier as detector, in the system shown in Figure 4.3 a sensitive *CCD* camera is employed as detector. Therefore, the system can detect very weak signals, and improve the sensitivity of the system. Images of the photoelastic patterns taken by the *CCD* sensor are transferred to a computer, in which the digital images are processed and the stress states are analyzed with the image processing and stress analysis software we

developed. Finally, the two-dimensional distributions of the stresses over the whole sample are obtained. We call this system the *CCD detection system*.

4.1.2 Operation Wavelength

When measuring the stress in microelectronic materials, the measured samples are directly placed in a polarized light field instead of using the model materials. The first factor we should consider when constructing the photoelastic system is that the polarized light should be able to transmit through the measured samples. Due to the intrinsic absorption, when the energy of photons of incident light is higher than the bandgap energy of measured materials, the materials will become opaque. On the other hand, every detector has a cutoff wavelength due to the intrinsic absorption. The detector could not respond to a radiation with the wavelength longer than its cutoff wavelength. The bandgap energies of several semiconductor materials and the appropriate light sources and detectors are listed in Table 4.1.

With account taken of the transparency of the sample being measured and the responsivity of the detector, there are three cases regarding to the relation between the transparency of the sample and the responsivity of the detector, as shown in Figure 4.4. In case (a) where the two curves overlap each other over a wide range of wavelength, we may be liberal in our choice of an operation wavelength in the range. Case (b) is excluded from application since the two curves do not overlap. As for case (c), since the two curves only overlap in their fall off regions, the system can work in this wavelength range only if the detector has a high sensitivity. For example, transmission through silicon occurs only at wavelengths longer than about $1.11\mu m$. Therefore, to measure a silicon crystal, the wavelength of the light source should be longer than $1.11\mu m$. By taking account of the transparency of the measured samples and the response of the detector, we choose two light sources: Quartz tungsten halogen lamps and a HeNe laser($1.15\mu m$), and two types of detectors: photomultiplier and silicon *CCD* sensor, both of which have a cutoff

wavelength of about 1.16μm. It has been discovered from our experiments that such choices of the light sources and the detectors perform satisfactorily.

Table 4.1 Bandgap energies, threshold wavelengths, appropriate light sources and detectors for some materials

Crystal	Eg	λc	Light Source†	Detector‡
Germanium	0.66eV	1.88μm	①②	❶❷
Silicon	1.12eV	1.11μm	①②③	❶❷❸❹❺
GaAs	1.43eV	0.87μm	①②③	❶❸❹❺
GaP	2.26eV	0.55μm	①②③④	❹❺
SiC	2.99eV	0.41μm	①②③④	❹❺
Diamond	5.47eV	0.23μm	①②③④	❹❺

†①Quartz tungsten halogen lamps ②Arc lamps ③HeNe laser(1.15μm) ④HeNe laser(0.6328μm).
‡❶PbS detector❷PbSe detector ❸InGaAs detector ❹Silicon detector❺Photomultiplier.

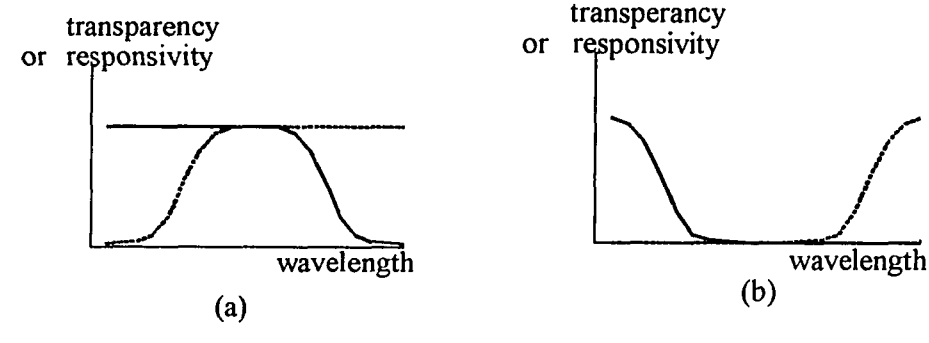

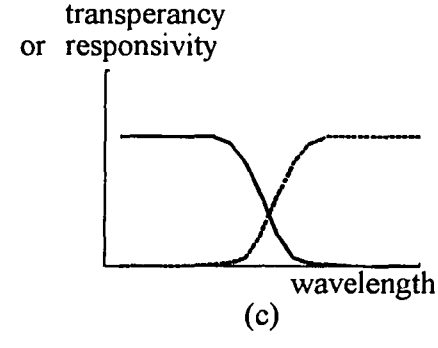

Figure 4.4 Schematic diagrams of the relation between the transparency of the sample and the responsivity of the detector.

(a)overlapping over a wide range, (b)separate, and (c)overlapping at their fall off regions
Dashed line stands for the transparency of sample; Solid line stands for the responsivity of detector.

4.1.3 Spatial Resolution

In our previous experiments the best spatial resolution in stress distribution was $100\mu m$ [20]. The continuous reduction in dimension of integrated circuits and microelectronic devices requires a higher spatial resolution for measuring the stress in a sample. In this section, we discuss the spatial resolutions of our point-by-point system and our *CCD* detection system.

For the point-by-point measurement, in order to reach a high spatial resolution, we adopt the scheme of focusing the optical beam onto the measured sample and moving the sample to scan the stress distribution along a certain section of the sample. The restriction on spatial resolution is the spot size confined by the diffraction limit of a Gaussian beam. The most widely encountered laser beam is one where energy distribution is axially symmetric, that is, field quantities are maximum at the center and decrease rapidly towards periphery. Assuming the z axis is the symmetric axis of the laser beam, the irradiance distribution of the Gaussian TEM_{00} beam is [40],

$$I(r) = I_0 e^{-2(x^2+y^2)/w^2} \tag{4.1}$$

where $(x^2+y^2)^{1/2}$ is the distance from the beam central axis (z axis), w stands for the beam width which is generally a function of z. Even if a Gaussian TEM_{00} laser beam wavefront was made perfectly flat at some plane, with all elements moving in precisely parallel directions, it would quickly acquire curvature and begin spreading in accordance with [40]

$$w(z) = w_0[1+(\frac{\lambda z}{\pi n w_0^2})^2]^{1/2} \tag{4.2}$$

where z is the distance propagated from the plane where the wavefront was flat, λ the wavelength of light, n the refractive index of medium, w_0 the radius of the $1/e^2$ irradiance contour at the plane where wavefront was flat, $w(z)$ the radius of the $1/e^2$ contour after the wave has propagated a distance z. Since there is a finite thickness d of the sample, the beam width w at the surface of the sample will be larger than the waist mean width w_0,

which occurs at the middle of the sample. The relationship among d, w, and w_0 is schematically illustrated in Figure 4.5. From (4.2), we can determine w_0 to obtain minimum beam width at $z=d/2$. By letting $\partial w(z,w_0)/\partial w_0=0$, we can solve for w_0:

$$w_0 = \sqrt{\frac{\lambda z}{\pi n}} \tag{4.3}$$

Considering the wafer sample with d=200μm, n=3.52 (for silicon), and λ=1.15μm, we have w_0=3.2μm. By substituting z=100μm and w_0=3.2μm into (4.2), we have the minimum beam radius $w(z$=100μm, w_0=3.2$\mu m)\approx$5μm. Thus, the diameter of the spot at z=100μm is 10μm. If d=400μm, the diameter of the spot at z=200μm is 13μm. Therefore, due to the divergence of Gaussian beam, the spatial resolution is limited by the finite thickness of sample and may not be better than 10μm.

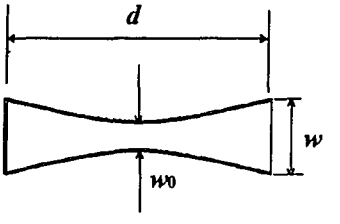

Figure 4.5 Schematical illustration of the relationship among d, w, and w_0.

For a *CCD* detection system, instead of a focused laser beam, we employ a parallel, uniform monochromatic light beam to illuminate the whole sample. The spatial resolution is dependent on many factors, such as the camera pixel size, the camera lens, and package overall size. Since optical microscopes have high *F/#* values, we can utilize high density arrays with small pixels. Usually, spatial resolution can be expressed by modulation transfer function (*MTF*) [41]. This function is measured using a pattern of black and white stripes of equal width. The pattern is considered resolved when the lines are sufficiently

distinct to permit counting them. The limit of spatial resolution of a *CCD* detection system is the diffraction limit of the microscope lenses, which is the upper bound of the *MTF* curves. For a given wavelength of light λ and entrance aperture of microscope objective d, the minimum distinguishable angle is given by [42]:

$$\phi = 1.22 \frac{\lambda}{d} \tag{4.4}$$

and the minimum distinguishable distance is given by

$$l = s \times \phi \tag{4.5}$$

where s is the working distance. For example, if the entrance aperture is $6.1mm$, working distance is $4.3mm$ (microscope objective Model 13580, Oriel®), and wavelength of light is $1.15\mu m$, the minimum distinguishable angle is 2.3×10^{-4} and the minimum distinguishable distance is $1\mu m$. Therefore, for such an optic system with negligible residual aberrations of the optic elements, the spatial resolution may reach $1\mu m$. Although a spatial resolution of $1\sim10\mu m$ is still not very good for device features which are typically less than $1\mu m$, it is much better than that can be done by using other methods and may be acceptable for many applications.

4.2 Optical Elements

4.2.1 Light Sources

In photoelastic experiments, we need a collimated and uniform beam with the desired spectral distribution and desired intensity. When selecting a source, the first factor we should consider is its wavelength range, which has been discussed in Section 4.1.2. After wavelength range, the other factor in choosing a source is usually its output power. For a single wavelength, to find the total output power per *nm* at any wavelength for any lamp, we should read the value of spectral irradiance from the spectral irradiance curve for the lamp, and find the conversion factor for the lamp housing and condenser type, and

multiply this by the value of the spectral irradiance. The conversion factor comes from the fact that a real lamp is not a point source nor truly isotropic. Finally, multiply the result by a modification factor when a rear reflector is used. The rear reflector captures "backwards emitted radiation", and when properly adjusted, reflects it back through the source to contribute to the total output.

In our measurement system, two kinds of light sources are used: quartz tungsten halogen lamp and helium neon laser. Quartz tungsten halogen lamps are popular visible and near infrared source because of their smooth spectral curve and stable output [43]. It uses a doped tungsten filament inside a quartz envelope, which is filled with a rare gas and a small amount of halogen. Current flowing through the filament heats the tungsten to higher than 3000K. The white light produced radiates through the clear quartz envelope. The specifications of the Quartz tungsten halogen lamp are listed below:

Lamp wattage	50 watts
DC voltage	12 volts
Spot size	~11 *mm*
Total output power	1.86 watts (> 780 *nm* 45%, >1000*nm* 28%)

A helium neon laser [44] with wavelength 1.152μ*m* is also employed in our experiments. Bellows are the specifications of Model 125*A* *helium neon laser* (SPECTRA-PHYSICS®):

Output wavelength:	1.152 μ*m*
Output power:	45 milliwatts
Beam diameter:	~3.0 *mm*
Beam polarization:	linear cross component less than 0.03%

4.2.2 Polarization Elements

Radiations from natural and incoherent artificial sources are usually unpolarized. There are several ways to produce polarized light from unpolarized [45]. Polarization may be

produced by reflection, scattering, wire grids, dichroism, and birefringence. When an unpolarized light beam passes through a polarizer, the emerging beam is largely polarized with the E vector parallel to the *transmission axis* of the polarizer. When a linearly polarized beam is incident on a polarizer and the polarizer rotated for maximum transmission, then k_1, the *major principal transmittance* is the ratio of transmitted to incident intensities. k_2, the *minor principal transmittance*, is the ratio when the polarizer is rotated for minimum transmittance. The *extinction ratio* is equal to k_2/k_1 [46]. In our photoelastic system, we use *VIS-NIR* dichroic sheet polarizers with extinction the ratio of 10^{-4}, which are fabricated from sheets of plastic made up of long chain organic molecules. In the manufacturing process, the thin film is "stretched" to orient the molecules, then dyed with an iodine compound to give electron mobility. Electrons can thus move easily only along the chain direction. This is equivalent to a fine grid polarizer. Light with the E vector in a plane perpendicular to the chain is transmitted; light with the E vector parallel to the chain is absorbed. Selected film is cemented between two ground and polished glass plates using an index of refraction matching cement. The low cost, wide acceptance angle, and large apertures make these polarizers of choice for many applications. However, they do not withstand ultraviolet or high power beams, which does not constitute a problem in our experiments, since we use a visible or near infrared light beam with low power.

Sometimes, a *quarter waveplate*, the most familiar retarder, is used to produce a circular polarized field [39]. A quarter wave plate is usually made from crystalline quartz or mica. Designed for single wavelength operation, they change linear polarized light to circularly polarized light or rotate the plane of linear polarization. The plates are generally in the form of discs cut so the optic axis of the crystal lies parallel to the entrance and exit faces. In addition to crystalline quartz or mica retarder, there is also sheet retarder which has the advantage of low cost and large aperture. Stretching plastic sheets induces birefringence. These birefringence sheets operate like crystal quartz retarders, but have lower optical quality and power handling capability.

4.2.3 Detectors

In a typical optical research system the detector measures radiant intensity, the light signals are converted into electrical signals, then typically amplified, processed by signal to noise improving electronics, and displayed. Detection systems are made possible by a few basic types of light-to-electrical conversions, such as photoemissive effect, photoconductive effect, and photodiode. Most detectors are described by certain figures of merit, which are usually functions of wavelength and temperature and may also be affected by detector size, modulating frequency, bias voltage and the gain of any internal amplifier. Some of the most important figures of merit are spectral responsivity, linearity range, noise equivalent power, and detectivity.

In a point-by-point measurement system, we usually employ a photomultiplier as detector. The photomultiplier tube is a photoemissive detector [47], in which light interacts directly with the electrons in the detector material. An absorbed photon frees an electron and the surplus energy gets converted into kinetic energy of the electron. The electrons emitted in this way produce the cathode photocurrent in photomultiplier tube, which amplifies the photocurrent by secondary emission. This is a low noise process that produces currents that are 6 to 8 orders of magnitude larger than the initial photocurrent. The D^* of the photomultiplier is typically 10^{15} $cmHz^{1/2}W^{-1}$, the highest among all photodetectors.

CCD, the acronym of charge-coupled-device, is a metal-oxide-semiconductor (*MOS*) capacitor array [48], which can collect and store minority carrier charge packets in localized potential wells at the Si-SiO_2 interface. The *CCD* can transfer charge packets in discrete-time increments via the controlled movement of potential wells. The charge packets can then be detected at the output via capacitive coupling. Thus a *CCD* acts as an analog shift register composed of three sections. 1) The input section which contains a diffusion, which is the source of minority carriers, and whose potential can be controlled, and an input gate that can be turned on and off to control the flow of charge from the

source diffusion into the first potential well. 2) The transfer section, containing a series of electrodes that control the potential at the Si-SiO_2 interface. When the voltages on the electrodes are properly manipulated, the potential wells are moved toward the output and the charge packets follow. 3) The output section is a reverse-bias p-n junction capacitance whose voltage is changed when a charge packet is transferred into it. The diode is then reset via reset switch to prepare for the next packet to be transferred into it. This node is typically connected to an *MOS* amplifier. The use of *CCD* as detector makes possible an almost instantaneous acquisition of one frame of data sets over certain area. The feature of *CCD* is its extremely low readout noise, a few electrons per pixel, and good separation between signal channels, *i.e.*, no blooming.

As discussed in Chapter 3, the minimum detectable stress is dependent on the dynamic range of the detector. For example, for a silicon sample with thickness 500μm, if we wish to apply the intensity analysis method to measure the stress of $6.5\times10^7 dyn/cm^2$ ($\delta \cong 16.3°$), an 8-bit detector (256 gray levels) is desired. If we hope to measure the stress of $2.0\times10^7 dyn/cm^2$ ($\delta=5°$, for a silicon sample of thickness 500μm), by using Fourier analysis method, from Figure 3.10 we know that the dynamic range of the detection system should not be less than 14 bits.

4.3 Error Analysis

4.3.1 Sources of Error

The general form of the stress-optic law (2.78) may be rewritten as

$$\Delta\beta_1 - \Delta\beta_2 = \pm\frac{\lambda\delta}{\pi d n_0^3}\cos 2\alpha \qquad (4.6)$$

where λ is the wavelength of light, δ is the birefringence phase difference, d is the sample thickness, n_0 is the refractive index of medium without stress. By taking a logarithm of both sides of (4.6), and ignoring the sign of its right hand side, we have

$$\ln(\Delta\beta_1 - \Delta\beta_2) = \ln\lambda + \ln\delta + \ln\cos 2\alpha - \ln d - \ln(\pi n_0^3) \tag{4.7}$$

Differentiate both sides and take absolute values, yields

$$\left|\frac{\Delta(\Delta\beta_1 - \Delta\beta_2)}{\Delta\beta_1 - \Delta\beta_2}\right| \le \left|\frac{\Delta\delta}{\delta}\right| + \left|\frac{\Delta\lambda}{\lambda}\right| + \left|\frac{\Delta d}{d}\right| + \left|\frac{\Delta\cos 2\alpha}{\cos 2\alpha}\right| + \left|\frac{\Delta n_0^3}{n_0^3}\right| \tag{4.8}$$

From (4.8), it is found that the error of birefringence index consists of five terms. In our discussion, the piezo-optic coefficient is assumed as a constant, we shall not consider its error here. Therefore, (4.8) represents the relative error of principal stress difference.

The first error term in (4.8) is the error introduced when measuring birefringence phase difference, which has been discussed in Chapter 3 and will be addressed later. The second term is the error of wavelength of light. If a helium neon laser is used as light source, since it is monochromatic, the error due to this term can be ignored. While a tungsten halogen lamp is employed, a polished silicon wafer is usually used as a filter. Only infrared light with wavelength longer than $1.12\mu m$ can be transmitted. Let us assume the cutoff wavelength of the detector (such as *CCD* camera) is $1.16\mu m$. If a central wavelength $1.14\mu m$ is used in calculation, the error induced will be about 1.8%. The third term of the right hand side of (4.8) comes from the measurement of sample thickness. Conventional thickness measuring techniques ensure that the error is less than 1%. The fourth error term arises from the error of the orientation deviation angle of the stress ellipsoid and the refractive index ellipsoid, which will be analyzed in next section. The fifth term is resulted from the error of the refractive index. If Δn_0=0.002, the error of this term will be less than 1%.

4.3.2 Error of Orientation Deviation Angle

The fourth error term in (4.8) arises from the error in evaluating the orientation deviation angle α of the stress ellipsoid and the refractive index ellipsoid. From the discussion in Chapter 2, we know that the deviation angle α is related to the coordinate system we choose and the directions of principal stresses and the direction of observation.

In the [112][$\bar{1}$10][$\bar{1}\bar{1}$1] coordinate configuration, if the observation is made along the [$\bar{1}\bar{1}$1] direction, the deviation angle α between the principal stresses and the principal refractive indices is equal to zero, and hence no error induced. For a thin (111) wafer, when observation is made along arbitrary direction within the [112]-[$\bar{1}$10] plane, the orientation deviation angle α is given by (2.89):

$$\tan 2\alpha = -2\sqrt{2}\,(\pi_{11} - \pi_{12} - \pi_{44}) \cos 3\varphi\, \sigma_2 / (\pi_{11} - \pi_{12} + 5\pi_{44}) \qquad (2.89)$$

The maximum value of α, 9.944°, is obtained at φ=30°. Since

$$\left|\frac{\Delta \cos 2\alpha}{\cos 2\alpha}\right| = \left|\frac{2 \sin 2\alpha}{\cos 2\alpha}\right| |\Delta\alpha| \qquad (4.9)$$

By assuming that $\Delta\alpha$ is less than 1°, we can estimate the error as:

$$\left|\frac{\Delta \cos 2\alpha}{\cos 2\alpha}\right| = 2\,|\tan 2\alpha|\,|\Delta\alpha| \le 2 \times \tan(2\times 9.944°) \times 1° \times \pi/180° = 1.3\% \qquad (4.10)$$

In the [110][$\bar{1}$10][001] coordinate configuration, while viewing in an arbitrary direction within the [110]-[$\bar{1}$10] plane, the directions of principal stresses coincide with the directions of the principal refractive indices. Thus, the orientation deviation angle α is equal to zero, and no error induced by this term. When the observation direction is [001], the orientation deviation angle α is given by (2.92)

$$\tan 2\alpha = (\pi_{11}-\pi_{12}-\pi_{44}) \sin 4\varphi \times [2\pi_{44} + 2\,(\pi_{11}-\pi_{12}-\pi_{44}) \sin^2 2\varphi]^{-1} \qquad (2.92)$$

from which we can obtain the maximum value of α, *i.e.*, 8.8957°, at φ=18.1°. By assuming that $\Delta\alpha$ is less than 1°, from (4.9), we have

$$\left|\frac{\Delta \cos 2\alpha}{\cos 2\alpha}\right| = 2\,|\tan 2\alpha|\,|\Delta\alpha| \le 1.1\% \qquad (4.11)$$

4.3.3 Measurement Error of Birefringence Phase Difference

The first error term in (4.8) is the error induced when measuring birefringence phase difference. In Chapter 3, we have analyzed the error of this term for several measurement methods adopted. For the Senarmont compensation method, the errors of measuring birefringence phase difference arise from the error of the polarization angle of polarizer ξ,

and the error of the retarding phase of the quarter waveplate ζ. By assuming that $\xi<5°$, $\zeta<5°$, for any value of φ, it has been shown that $|\Delta\delta/\delta|$ will be less than 3%.

For the intensity analysis method, there are two major sources of error in measuring birefringence phase difference: a) The error of the polarization angle of polarizer or analyzer ξ, and the non-zero of extinction ratio of polarizers (the extinction ratio of polarizer and analyzer is ζ). When $\xi=1°$ and $\zeta=10^{-4}$, we have $\Delta\delta=2.8°$. b) The error due to stray light produced by internal reflection, which will introduce a relative larger error of $\Delta\delta\cong16.3°$. Thus, the overall error of birefringence phase difference is 19.1°. For a silicon sample of thickness of $500\mu m$, this corresponds to an error of stress about $7.6\times10^7 dyn/cm^2$. When employing the Fourier analysis method, the principal source of error of measuring birefringence phase difference is due to stray light which is produced by internal reflection. If the stray light factor r is 0.01, we have $\Delta\delta\approx4.5°$. For a silicon sample with thickness $500\mu m$, such a error in measuring birefringence difference corresponds to a error in measuring stress $1.8\times10^7 dyn/cm^2$.

Therefore, of the several factors contributing to the error of measuring principal stress difference, the error of measuring birefringence phase difference is dominant. Each of the others has a relative error of about 1%. When employing the Senarmont compensation, the total relative error is about 8%. For the intensity analysis method and the Fourier analysis method, when the birefringence phase difference measured becomes small, the error will become large. The minimum detectable birefringence phase difference depends on the method adopted. The Fourier analysis method has a better sensitivity (about 5°) than the intensity analysis method (about 20°).

4.4 Summary

This chapter has presented two kinds of arrangements of photoelastic stress measurement systems in terms of point-by-point measurement system and *CCD* detection system. There

is also a special type of system arrangement: the reflection type. We also discussed the selection of optical elements, including light source, polarization element, and detector. For example, when selecting a light source, we should take account of its irradiation spectrum, its effective output power, its beam size and beam polarization. When selecting a detector, we should be concerned about its spectral response, its detectivity and its linear range.

It is shown that our systems have a relatively high spatial resolution. The spatial resolution of the point-by-point measurement system, which is limited by the finite thickness of the sample and the intrinsic property of Gaussian beam, may reach $10\mu m$. In a *CCD* detection system, with the necessary amplifying lenses, the spatial resolution may attain the diffraction limit of that wavelength, *i.e.*, about $1\mu m$. The sensitivity of the system is dependent upon the measurement method adopted. For a silicon sample with thickness $500\mu m$, the minimum measurable stress of the intensity analysis method is about $8\times10^7\ dyn/cm^2$. For a Fourier analysis method, the minimum measurable stress is about $2\times 10^7\ dyn/cm^2$.

CHAPTER 5

APPLICATION IN MICROELECTRONICS

In this chapter we will discuss the application of photoelastic principles and methods in some microelectronic materials. The stress distribution in a synthetic diamond substrate is analyzed, the stress state of the substrate/thin film structures is investigated, and the stress induced in silicon wafers during diffusion processes is studied. In some cases, the formulated models are used to describe the experimental results, which are compared with the modeling results.

5.1 Stress Distribution in a Diamond Substrate

In this section, we analyze stress distribution in a synthetic diamond substrate, with an automatic data acquisition and analysis system. The digital image processing techniques are applied to improve the quality of sensed images, to reduce noise, and to determine the boundary of the sample. The section also illustrates the determination of birefringence phase difference and principal stress directions. The shearing stress difference method is applied to determine the two-dimensional stress distribution over the whole synthetic diamond substrate sample.

5.1.1 Sample and Data Acquisition

The synthesis of diamond crystals is a rather elaborate process; and compared to microelectronic standards only minimum size crystals can be grown. Nevertheless, these synthetic substrates enable the fabrication of high performance devices using homoepitaxial films. These homoepitaxial electronic structures represent therefore the state-of-the-art in achievable electronic performance. High temperature Schottky diodes

with high current rectification ratios and digital high temperature *MISFET* circuits have been demonstrated. However, only very limited information is available on the chemical, mechanical, optical and electronic properties of the diamond single crystal substrates. For example, defect networks and doping inhomogenities can be observed optically. Both may cause internal stress; for example, high doping concentrations cause lattice mismatch to undoped areas and doping inhomogeneities will therefore lead to internal stresses. Various methods have been developed to characterize the stress state in diamond materials, which include measuring the curvature of the substrate by using optical method [49], measuring the lattice mismatch of the materials by using *X*-ray diffraction [50], or analyzing Raman line shape by using Raman spectroscopy [51]. The limitation of the curvature-measuring method is its lack of spatial resolution and non suitability for situations where no curvature occurs. Although the methods of *X*-ray diffraction and Raman spectroscopy have a higher spatial resolution, the complexity of equipment and the low efficiency of measurement prevent them from being widely used. In this section, the internal stress distribution of a commercially available synthetic diamond substrate has been investigated using the photoelastic method and the imaging and data acquisition techniques.

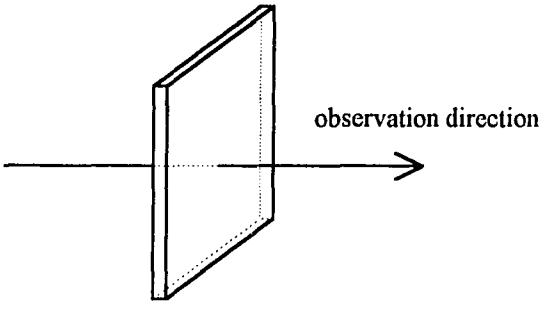

Figure 5.1 Orientation of the sample in measuring.

The sample investigated is a (100) oriented diamond substrate of $3mm \times 3mm$ surface dimension and $1mm$ thickness, which is doped with nitrogen and highly insulated.

Observations normal to the sample surface are made, as shown in Figure 5.1. The measurement configuration is shown in Figure 4.3. The system employs a *CCD* image sensor as detector. An *A/D* converter is used to convert analog photoelastic patterns to digital images, which are transferred to a microcomputer. With the software we developed, the computer automatically performs system control, data acquisition, image processing, data analysis, and stress calculation.

With the sample placed in the experimental system, the starting positions of the polarizer and the analyzer are set in a dark, linearly polarized field. At that time the orthogonal polarization axes are set at 0°, so that the isochromatic and isoclinic lines with 0° are obtained. Figure 5.2(*a*) shows the photoelastic pattern of this position. While two polarization axes are kept orthogonal, the polarizer and the analyzer are rotated by an angle of φ. The isoclinic line with 0° is replaced by that with φ, while the isochromatic line remained intact. Synchronous rotation of two orthogonal polarizers from 0° to 90° will in turn result in a series of isoclinic lines varying gradually from 0° to 90°. Each time the photoelastic pattern is imaged by a *CCD* camera, and the digital image is stored for further processing. Figure 5.2(*b*) shows the photoelastic pattern with φ=45°.

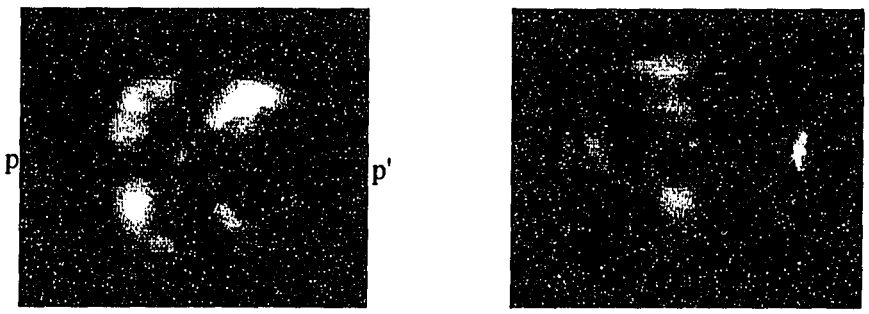

(*a*) φ=0° (*b*) φ=45°

Figure 5.2 Photoelastic patterns in dark planar polarized field.

5.1.2 Image Processing [52]

The digitized photoelastic pattern is transferred through a graphic interface to the memory of a computer. Since there will be distortion and blur during the procedure of image acquisition, conversion, and transfer, before calculating the stress distribution, the photoelastic pattern images must be processed.

The random noise of an image is reduced by the averaging technique. Consider a noisy image $g(x,y)$ formed by the addition of noise $\eta(x,y)$ to an original image $f(x,y)$:

$$g(x,y) = f(x,y) + \eta(x,y) \tag{5.1}$$

where the assumption is that at every point (x,y) the noise is uncorrelated and has zero average value. By averaging M images for the same pattern, we have

$$\bar{g}(x,y) = \frac{1}{M}\sum_{i=1}^{M} g_i(x,y) \tag{5.2}$$

It follows that

$$\bar{g}(x,y) \Rightarrow f(x,y) \tag{5.3}$$

when M increases, and

$$\sigma^2_{\bar{g}(x,y)} = \frac{1}{M}\sigma^2_{\eta(x,y)} \tag{5.4}$$

Here $\sigma^2_{\bar{g}(x,y)}$ and $\sigma^2_{\eta(x,y)}$ are the variances of $\bar{g}$ and η. Eq.(5.4) indicates that, as M increases, the variability of the pixel values at each location (x,y) decreases.

The noisy image with some individual noise pixels can be improved by using smoothing filters. In the experiment, we use a *median filter*, whose principal function is to force points with distinct intensities to be more like their neighbors, actually eliminating intensity spikes that appear isolated in the area of the filter mask. This method is particularly effective when the noise pattern consists of strong, spikelike components. The median m of a set of values is such that half the values in the set are less than m and half are greater than m. In order to perform median filtering in a neighborhood of a pixel, we first sort the values of the pixel and its neighbors, determine the median, and assign this value to the pixel. The gray level of each pixel is replaced by the median of the gray levels

in a neighborhood of that pixel, instead of by the average. Figure 5.3 shows the result of a 3×3 median filter applying on the images shown in Figure 5.2. From Figure 5.3 we can visualize the effect of removing the individual noise pixels in Figure 5.2.

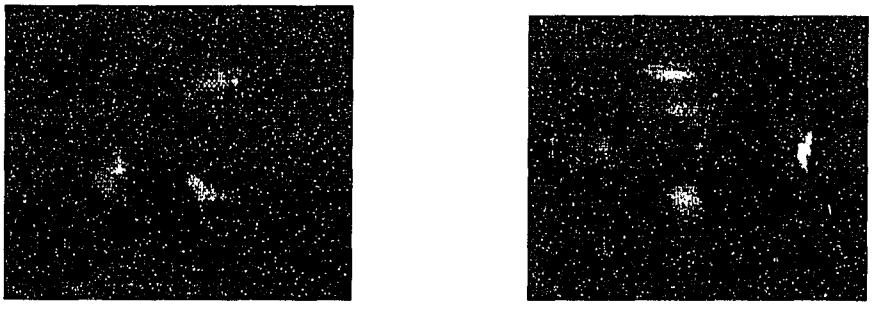

(*a*) φ=0° (*b*) φ=45°

Figure 5.3 Result image after 3×3 median filtering.

In order to determine the boundary of the sample area being measured, the simple global thresholding technique is employed. In our experiment, a two-value image is created to determine the boundary of the sample. With the sample intact, by removing the polarizer and the analyzer, and the probing light beam transmitting through the sample, we can obtain an image such that the sample location is uniformly bright, but the region outside the illuminated area is dark. Segmentation is then accomplished by scanning the image pixel by pixel and label each pixel as object or background, depending on whether the gray level of that pixel is greater or less than a threshold T. Applying the threshold technique to such image, we can obtain a two-value image of which the pixels of the measured area are 1, the pixels of background are 0. Multiplying the two-value image with the photoelastic pattern image, the pixels of the photoelastic pattern are unchanged but the pixels of the background region are set to 0.

5.1.3 Determination of Photoelastic Parameters

After image acquisition and processing, we can calculate the photoelastic parameters, the birefringence phase difference δ and the direction of the principal refractive index ϕ. In our experiments, to obtain these photoelastic parameters, two approaches are in use: the Fourier analysis method and the intensity analysis method. In the intensity analysis method, the relation between the birefringence phase difference and the intensity of transmitted light is given by (3.49), which is rewritten as:

$$\delta = \pm\cos^{-1}[1-2(\frac{I_1}{I_1+I_2}+\frac{I_1'}{I_1'+I_2'})]\pm 2k\pi \qquad (k=0,1,2,...) \tag{5.5}$$

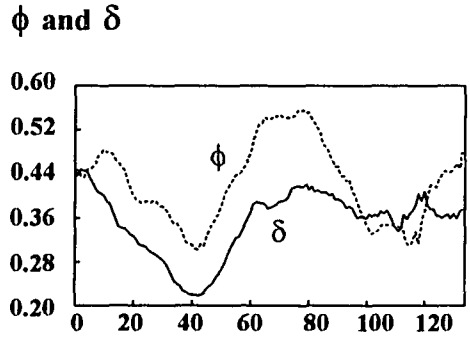

Figure 5.4 Distribution of photoelastic parameters along section the *PP'* of the sample.

where I_1 is the intensity of the transmitted light in the planar cross-polarized light field and I_2 the intensity of the transmitted light in the planar parallel-polarized light field, and I_1' and I_2' the corresponding intensities of the two polarized transmitted lights after the whole polarized light field is rotated by 45° clockwise. The directions of the principal refractive indices at the measured point are determined by (3.50), which is rewritten as:

$$\phi = \pm\frac{1}{2}\tan^{-1}\sqrt{\frac{I_1/(I_1+I_2)}{I_1'/(I_1'+I_2')}}\pm\frac{k'\pi}{2} \qquad (k'=0,1,2,...) \tag{5.6}$$

where ϕ is the angle between the principal refractive index n_1 and the reference axis x. The distribution of these two parameters, δ and ϕ, along the central horizontal line PP' is shown in Figure 5.4.

5.1.4 Calculation of Stress Distribution

From the theory of elasticity, the two-dimensional stress state is determined by the two differential equations [10]:

$$\frac{\partial \sigma_{xx}}{\partial x} + \frac{\partial \sigma_{xy}}{\partial y} = 0$$
$$\frac{\partial \sigma_{xy}}{\partial x} + \frac{\partial \sigma_{yy}}{\partial y} = 0 \qquad (5.7)$$

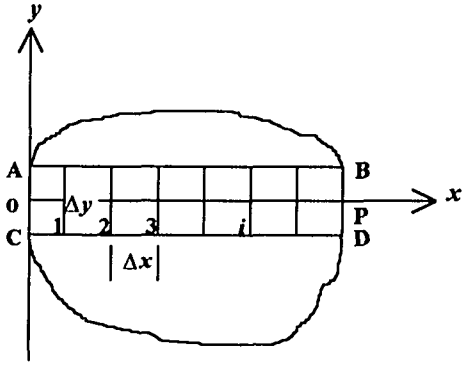

Figure 5.5 Schematic diagram for shearing stress difference method.

Integrating the first equation of (5.7) from point o to point P along ox axis, as shown in Figure 5.5, we have

$$(\sigma_{xx})_P = (\sigma_{xx})_0 - \int_0^P \frac{\partial \sigma_{xy}}{\partial y} dx \qquad (5.8)$$

If the integral is approximately replaced by a finite difference, (5.8) is rewritten as

$$(\sigma_{xx})_P = (\sigma_{xx})_0 - \sum_0^P \frac{\Delta \sigma_{xy}}{\Delta y} \Delta x \qquad (5.9)$$

where the normal stresses $(\sigma_{xx})_p$ and $(\sigma_{xx})_0$ are known beforehand as boundary conditions, $\Delta\sigma_{xy}$ is the shearing stress difference along increment Δy between the two auxiliary cross sections *AB* and *CD*. The shearing stress σ_{xy} is given as

$$\sigma_{xy} = \frac{\sigma_1 - \sigma_2}{2} \sin 2\theta \tag{5.10}$$

where θ is the angle between the principal refractive index n_1 and the reference axis *ox*. If two neighbor points are expressed by *i*-1 and *i*, (5.9) can be replaced by

$$(\sigma_{xx})_i = (\sigma_{xx})_{i-1} - (\Delta\sigma_{xy})cp\Big|_{i-1}^{i} \frac{\Delta x}{\Delta y} \tag{5.11}$$

where,

$$(\Delta\sigma_{xy})cp\Big|_{i-1}^{i} = \frac{(\Delta\sigma_{xy})_{i-1} + (\Delta\sigma_{xy})_i}{2} \qquad (i=1,2,3,...,P) \tag{5.12}$$

Eq.(5.12) represents the average value of shearing stresses of two neighbor points. For *P* points, we can write *P* expressions based on (5.11), whose sum is equal to (5.9). When stress σ_{xx} is known, the other normal stress σ_{yy} can be calculated by [10]

$$\sigma_{yy}=\sigma_{xx} \pm (\sigma_1 - \sigma_2)\cos 2\theta \tag{5.13}$$

Thus, the two principal stresses σ_1 and σ_2 can be calculated from following formulas [10],

$$\sigma_1 = \frac{\sigma_{xx} + \sigma_{yy}}{2} + \frac{\sigma_1 - \sigma_2}{2}$$

$$\sigma_2 = \frac{\sigma_{xx} + \sigma_{yy}}{2} - \frac{\sigma_1 - \sigma_2}{2} \tag{5.14}$$

To eliminate the accumulated error caused from the shearing stress difference method, the correction of error is carried out by considering boundary conditions while calculating normal stress σ_{xx}.

In order to calculate the stress distribution along a cross section *PP'*, we choose two auxiliary sections *AB* and *CD*, as shown in Figure 5.5, where $\Delta x/\Delta y=1$. The boundary condition at $i=0$ can be determined by Eqs.(5.5) and (5.6), as shown in Figure 5.4, *i.e.*, $\delta(i=0)=0.4315$ and $\phi(i=0)=0.4665$. The components of piezo-optic coefficient of a diamond crystal are given in Table 2.1. For a (100) oriented wafer, if the viewing direction is along

[001] and two principal stresses are in the plane of [110][$\bar{1}$10], the stress-optic law takes the form of (2.91), that is

$$[\pi_{44}+ (\pi_{11}-\pi_{12}-\pi_{44}) \sin^2 2\varphi] (\sigma_1 - \sigma_2) = \pm \frac{\lambda\delta}{\pi d n_0^3} \cos 2\alpha \qquad (2.91)$$

where the angle α is related to the direction of principal refractive index ϕ by using (2.92) and (2.79):

$$\tan 2\alpha = (\pi_{11}-\pi_{12}-\pi_{44}) \sin 4\varphi \times [2\pi_{44}+ 2 (\pi_{11}-\pi_{12}-\pi_{44}) \sin^2 2\varphi]^{-1} \qquad (2.92)$$

$$\varphi = \alpha + \phi \qquad (2.79)$$

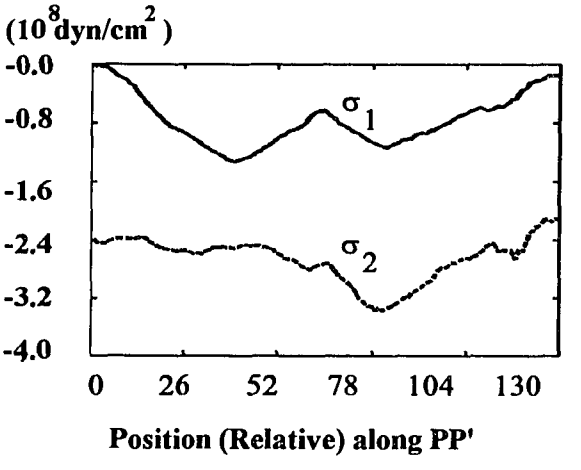

Figure 5.6 Distribution of the principal stresses along the section *PP'* of the sample.

where φ is the direction of the principal stress σ_1. From the known value of ϕ, we can calculate α and φ. By substituting ϕ, α and φ into (2.91) we can determine the principal stress difference $(\sigma_1-\sigma_2)$. Based on Eqs.(5.9)~(5.13), we can calculate the distributions of the principal stresses σ_1 and σ_2 along section *PP'*. Finally, from (5.14), we can determine two principal stresses along section *PP'*. By repeating the above procedure we can calculate the principal stresses over the whole sample. The distributions of the two principal stresses along section *PP'* of the sample in Figure 5.2 are shown in Figure 5.6.

The transverse axis is the relative position coordinate for calculating across the measured section. It is obvious that at the edge of the sample, the principal stress $\sigma_1 = 0$, while the other principal stress σ_2 is negative. In the central region of the sample both principal stresses are compressive, which have the mean values of $-7.8\times10^7 dyn/cm^2$ for σ_1 and $-3.0\times10^8 dyn/cm^2$ for σ_2.

5.2 Thin Film-induced Substrate Stress in Substrate/Thin Film Structure

Almost all microelectronic devices have the basic structure of a semiconductor substrate with thin films of different materials on it. Each thin film layer is comprised of multiply connected or disconnected regions. The thin film layer and its discontinuity will give rise to stress field in the substrate. In this section, we present the application of photoelastic method in studying the film-induced stress in substrate/thin film structures. The stress state induced by an oxide thin film, the localized stress near a groove of thin film on the wafer, and the stress induced by metal film are investigated with the Senarmont compensation method and the Fourier analysis method.

5.2.1 Stress Induced by Oxide Thin Film

(111) and (100) oriented silicon wafers with resistivities greater than $2\Omega cm$ and thickness $250\sim500\mu m$ are prepared by cleaving them to form a rectangle of $8mm\times12mm$. Scribing orientation and observation direction of the samples are shown in Figure 5.7. In order to obtain a uniformly transparent sample, a pair of (110) parallel windows are polished carefully with colloid SiO_2 polishing fluid until the damaged layer is removed and the two windows become parallel, smooth and bright. Infrared light can pass through the polished silicon wafer uniformly, and interference fringes will appear clearly if an external pressure is exerted on the wafer.

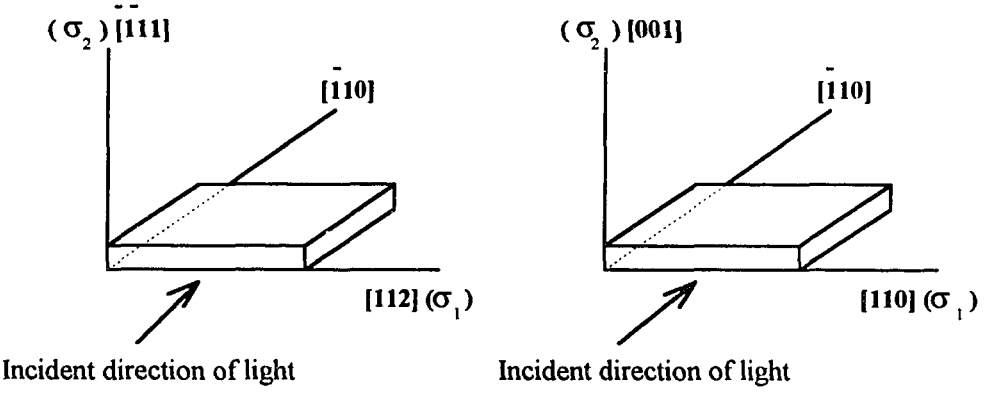

(a) (111) wafer (b) (100) wafer

Figure 5.7 Schematic representation of wafer in the coordinate systems.

After a thin film of oxide is grown at a high temperature of 1180°C for 120 minutes on the surface of a silicon substrate, thermal stress may be induced by the mismatch of thermal expansion coefficient between the substrate and the film when they are cooled from the growth temperature [53]. To determine the directions of principal stresses, the sample is observed while rotating the polarizer and the analyzer synchronously under a dark, linearly polarized dark field. When the sample surface is parallel to one of the polarization axes, isoclinic lines appear except at the edges of the oxide thin film, indicating that the directions of principal stresses are parallel or perpendicular to the sample surface. It is agree with the two-dimension stress theory of elasticity [54] that the principal stress perpendicular to sample surface is equal to zero.

For a (111) oriented wafer, if an observation is made along the [$\bar{1}$10] direction and secondary principal stress σ_1 is in the [112] direction, by substituting φ=90° into (2.89), the birefringence deviation angle α is equal to zero. Eq.(2.88) is rewritten as:

$$\frac{1}{6}(\pi_{11} - \pi_{12} + 5\pi_{44})\,\sigma_1 = \pm\frac{\lambda\delta}{\pi d n_0^3} \tag{5.15}$$

where the values of π_{11} - π_{12} and π_{44} are given in Table 2.1. By substituting n_0=3.53, λ =1.15μm, and d=8mm into (5.15), we can obtain the relation between σ_1 and δ:

$$\sigma_1 = 1.82\times10^7\delta \; dyn/cm^2 \tag{5.16}$$

For a (100) wafer, if an observation is made in the [$\bar{1}$10] direction and stress σ_1 is in the [110] direction, then from (2.94), the birefringence deviation angle α is zero. The stress σ_1 can be determined by using (2.95) with φ=90°:

$$\frac{1}{2}(\pi_{11}-\pi_{12}+\pi_{44})\sigma_1 = \pm\frac{\lambda\delta}{\pi d n_0^3} \tag{5.17}$$

By substituting n_0=3.52, λ=1.15μm, d=8mm into (5.17), we have the relation of σ_1 and δ:

$$\sigma_1 = 1.121\times10^7\delta \; dyn/cm^2 \tag{5.18}$$

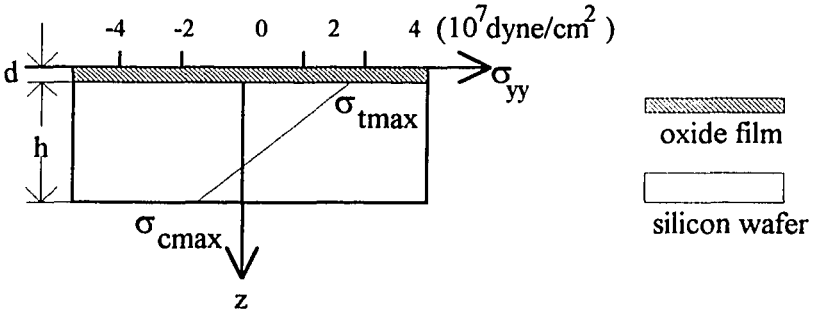

Figure 5.8 Stress distribution across the thickness of an oxidized (100) silicon wafer.

The measurement result for an oxidized (100) silicon wafer is schematically shown in Figure 5.8, where h is the thickness of the substrate, d is the thickness of the oxide layer. From Figure 5.8, a tensile stress is found in the substrate region near SiO_2 layer. It is attributed to the difference of the thermal expansion coefficients of oxide layer (0.55×10^{-6}/ °C) and silicon substrate (3.9×10^{-6}/°C). At growth or deposition temperature, there is no stress in the structure as long as thermal equilibrium is reached. Upon cooling to room temperature, the contraction of silicon substrate region near the SiO_2 layer is constrained

by the SiO_2 layer, which has a smaller thermal expansion coefficient. As a result, tensile stress occurs in this region of the silicon substrate, and a compressive stress appears in the SiO_2 layer. The wafer will curve towards the back surface of substrate without oxide layer. Such a curvature will induce a compressive stress in the substrate region near the back surface. Furthermore, by applying static force balance condition, the stress in the oxidized thin film is estimated to be in the order of 10^9 *dyn/cm*^{2}.

The experimental result may be compared with a theoretical calculation. By the method of minimizing the total Helmholtz-free energy, the stress distribution of the thin film/substrate structure can be calculated. The total Helmholtz free energy of a multilayered plate at temperature T is expressed as follows [55]:

$$F(T) = \sum_{m=1}^{n} \int_{v_m} d^3x F_m^*(T) \qquad (5.19)$$

where $F_m^*(T)$ is the Helmholtz free energy of each layer, with m=1 denoting the substrate, and m=2 the oxide thin film. The integral is over the volume of each layer. By utilizing the variation method, the warping deformation of the thin film/substrate structure due to the difference of thermal expansion coefficients can be calculated [55]. The calculation result is shown in Table 5.1

Table 5.1 Calculated stress distribution across the thickness of silicon substrate and in SiO_2 thin film by minimizing the total Helmholtz-free energy.

Distance from interface	Stress(*dyn/cm*^{2})
SiO_2 Thin film	-3.26×10^9
0 μm	3.70×10^7
83 μm	2.68×10^7
166 μm	1.66×10^7
250 μm	6.54×10^6
330 μm	-3.60×10^6
416 μm	-1.37×10^7
500 μm	-2.39×10^7

where we assume that the thicknesses of substrate and thin film are

$$d = 1\ \mu m, \qquad h = 500\ \mu m, \tag{5.20}$$

respectively, and the temperature difference between growth and measurement is ΔT=-1155°C. From Table 5.1 a good agreement with the photoelastic experimental result in Figure 5.8 is found.

5.2.2 Stress Induced by Discontinuity of Thin Film

In the neighborhoods of discontinuities of the surface films, there exists a very large localized stress field in substrate due to the film "edge forces" [56]. In the case of a concentrated line force F_x tangential to the boundary of a half space, as shown in Figure 5.9, the solutions for the substrate-stress components are given as [57]:

$$\sigma_x = -\frac{2F_x}{\pi}\frac{x^3}{(x^2+z^2)^2} \tag{5.21}$$

$$\sigma_z = -\frac{2F_x}{\pi}\frac{xz^2}{(x^2+z^2)^2} \tag{5.22}$$

$$\tau_{zx} = -\frac{2F_x}{\pi}\frac{x^2z}{(x^2+z^2)^2} \tag{5.23}$$

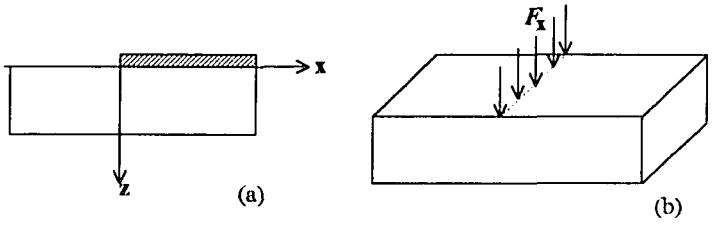

Figure 5.9 Schematic diagram showing
(a) a thin film deposited on a substrate half-space
(b)a concentrated line force on the boundary of half space.

Figure 5.9(b) shows a δ-function-like of force distribution, which has a finite value at x=0, and equals zero everywhere else. However, due to the elasticity of the substrate, the stress in the thin film is distributed, approaching the uniform build-in stress asymptotically.

This distributed stress in turn gives rise to a distributed force. For a distributed force, a force-density function $\partial F_x/\partial x$ is given by [58]

$$\frac{\partial F_x}{\partial x} = d\frac{\partial \sigma_{f,x}}{\partial x} \tag{5.24}$$

where d is the thickness of the thin film, $\sigma_{f,x}$ is the stress in the thin film, which approaches a uniform built-in stress of σ_0 far away from the thin film edge. By convolution of Eqs.(5.21), (5.22) and (5.23), we can obtain these stress components:

$$\sigma_x = -\frac{2d}{\pi}\int_0^\infty \frac{(x-u)^3}{[(x-u)^2+z^2]^2}\frac{\partial \sigma_{f,x}(u)}{\partial u}du \tag{5.25}$$

$$\sigma_z = -\frac{2d}{\pi}\int_0^\infty \frac{(x-u)z^2}{[(x-u)^2+z^2]^2}\frac{\partial \sigma_{f,x}(u)}{\partial u}du \tag{5.26}$$

$$\tau_{zx} = -\frac{2d}{\pi}\int_0^\infty \frac{(x-u)^2 z}{[(x-u)^2+z^2]^2}\frac{\partial \sigma_{f,x}(u)}{\partial u}du \tag{5.27}$$

The stress distribution in thin film $\sigma_{f,x}(x)$ can be determined by the continuity of thin film lattice to substrate-surface lattice.

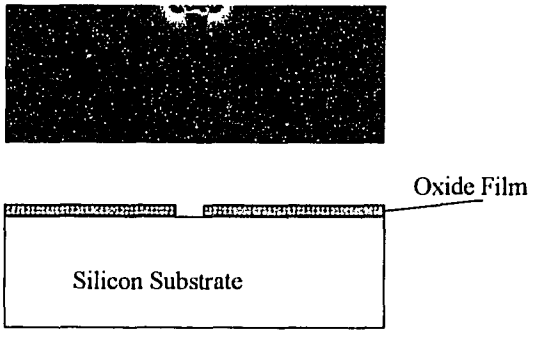

Figure 5.10 Structure of a groove of thin film on substrate and photoelastic pattern.

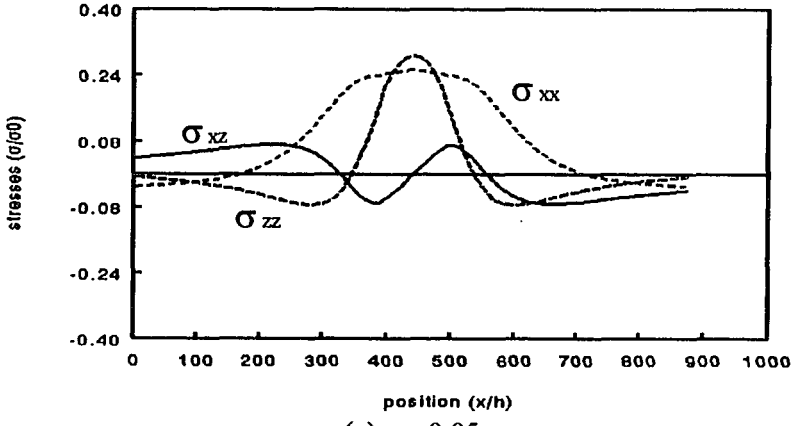

(a) z = 0.05 μm

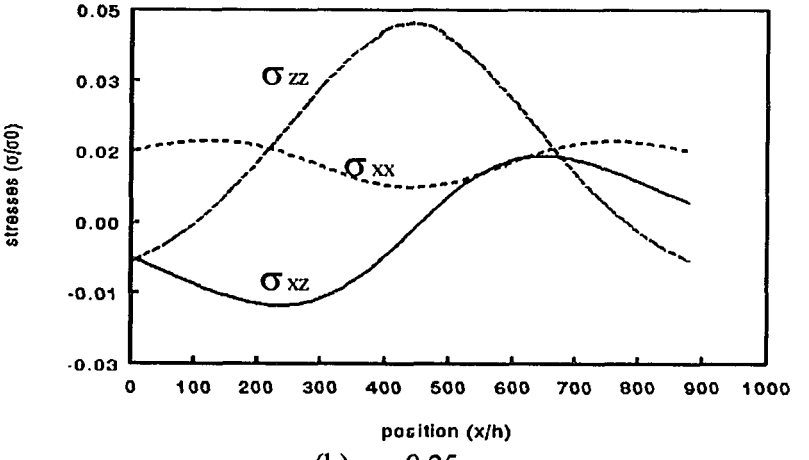

(b) z = 0.25μm

Figure 5.11 Stress distribution in substrate near the groove of the thin film, where h is the thickness of the SiO_2 thin film, and σ_0 is the uniform built-in stress in the SiO_2 thin film far away from the groove.

For many microelectronic device structures, edges and grooves are etched out of the thin film on a substrate wafer. The presence of stress in the substrate is due to such an open groove of the thin film. Figure 5.10 shows the schematics of the structure with an etched groove in SiO_2 thin films, and its corresponding photoelastic pattern. According to

Eqs.(5.25), (5.26) and (5.27) and on the basis of the stress superposition principle, the stress distribution in the substrate of such structure is calculated, as shown in Figure 5.11. Near the thin film/substrate boundary, the localized stress field for the oxide thickness $1\mu m$ and groove wide $5\mu m$ can be as large as the stress in the oxide thin film, which is in the order of $10^9 dyn/cm^2$. At $0.05\mu m$ from the interface, the stress is about 20% of the built-in stress of the thin film. Far from the interface, the stress due to the edge will decrease rapidly. For example, at $0.25\mu m$ from the boundary, the local stresses reduce to 2~5% of the built-in stress in the oxide thin film.

5.2.3 Stress Induced by Metal Films

5.2.3.1 Nickel-Plating on a Diffusion Wafer In this experiment, an n-type (111) oriented silicon wafer with thickness 400 μm is used. At first, boron impurities are diffused to form a *p-n* junction at about $100\mu m$ from the surface of the substrate. Then phosphorus impurities are doped to form the J_3 junction of the thyratron. The surface concentration of phosphorus is about $10^{21} cm^{-3}$ and the junction depth is about $35\mu m$. After boron and phosphorus diffusion, a $3\sim4\mu m$ layer of nickel thin film is chemically plated onto the wafer at 90°C, to improve the solderability. A measurement is performed on the rectangular sample with the dimension of $8mm \times 10mm \times 400\mu m$. The observation is made in the flank sides of the sample. The probing direction is along $[\bar{1}10]$, and the observation windows are on (110) planes, as shown in Figure 5.7(a).

From (2.89), when an observation is made along the $[\bar{1}10]$ direction and the secondary principal stress σ_1 is in [112] direction, with $\varphi=90°$, the birefringence deviation angle α is zero. The Senarmont compensation method or the Fourier analysis method is adopted to measure the birefringence phase difference δ at every point along the thickness of the sample. From (2.88) with $\varphi=90°$, $n_0=3.53$, $\lambda=1.15\mu m$, $d=8mm$, $\pi_{11}-\pi_{12}=-12.22 cm^2/dyn$, and $\pi_{44}=-6.5\ cm^2/dyn$, we may relate the secondary principal stress σ_1 with the birefringence phase difference δ by using (5.16):

$$\sigma_1 = 1.82\times10^7\delta \; dyn/cm^2 \qquad (5.16)$$

Figure 5.12 shows the stress distribution across the thickness of the sample. It is found, from Figure 5.12, that compressive stress is introduced into the substrate region near the interface of the boron diffused layer, and tensile stress is present in the other side of the wafer. The maximum compressive stress induced by the structure of three layers (boron diffused layer, phosphorus diffused layer, and nickel-plating layer) is relative large, about $9.6\times10^7 dyn/cm^2$. Since there is a relative large thermal coefficient difference between nickel and silicon ($\alpha_{Si}=4.2\times10^{-6}/°C$, $\alpha_{Ni}=14\times10^{-6}/°C$), a compressive stress is expected to be induced into silicon substrate. In addition, since the atomic radii of both phosphorus (1.10Å) and boron (0.88Å) are less than that of silicon (1.17Å), the doped phosphorus and boron tends to cause crystal lattice contract and also results in compressive stress in the silicon substrate region near the diffused layer.

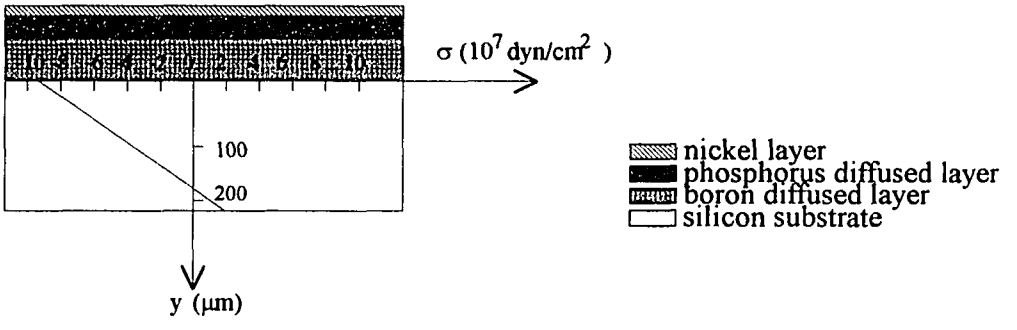

Figure 5.12 Stress variation across the thickness for a sample with boron and phosphorus diffused layer and nickel-plating film on its surface.

5.2.3.2 GaAs Wafer with Thin Gold Film A (100) GaAs wafer with a layer of thin gold film is studied by using photoelastic method. The GaAs substrate is two-side polished and with a thickness of 500μm, and a gold film of 3μm is deposited on the GaAs substrate. The deposition temperature is 650°C. The wafer is cut into the sample of $4mm\times4mm$

rectangles. The sample orientation and the observation direction are the same as those in Figure 5.7(b). A pair of parallel windows are made on (110) surfaces for probing from the flank sides of the sample.

Since the observation is made along the [$\bar{1}$10] direction and the secondary principal stress σ_1 is in the [110] direction, from (2.94) with φ=90°, the birefringence deviation angle α is zero. The photoelasticity method is applied to determine the birefringence phase difference δ at every point along the thickness of the sample. From (2.95) with φ=90°, we may relate the secondary principal stress σ_1 with the birefringence phase difference δ by using (5.17):

$$\frac{1}{2}(\pi_{11}-\pi_{12}+\pi_{44})\sigma_1 = \pm\frac{\lambda\delta}{\pi d n_0^3} \qquad (5.17)$$

By substituting n_0=3.34, λ=1.15μm, d=4mm into (5.17), we have the relation of σ_1 and δ:

$$\sigma_1 = 3.19\times10^7\delta\ dyn/cm^2$$

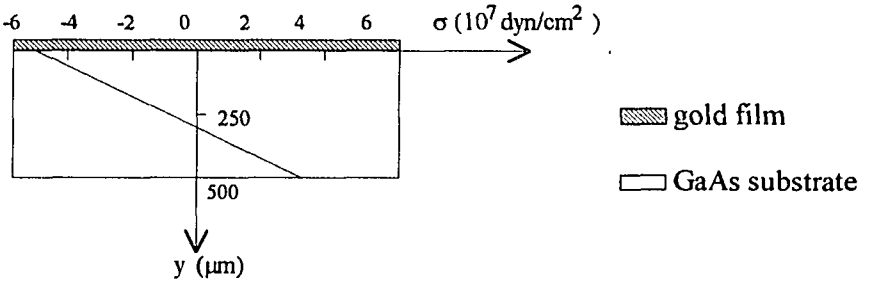

Figure 5.13 Stress distribution across the thickness of the GaAs substrate.

The measured result is shown in Figure 5.13, where we can find a linear distribution of the stress σ_1 across the thickness of the GaAs substrate. It is evident that a compressive stress is present in the upper region of the GaAs substrate near the gold film (the maximum value at the interface is about -5×10^7*dyn/cm*^{2}), and a tensile stress is in reverse

side of the sample (the maximum at the surface is about $3.4\times10^{7}dyn/cm^{2}$). This result is expected since the thermal expansion coefficient of gold ($11.9\times10^{-6}/°C$) is about twice larger than that of GaAs ($6.86\times10^{-6}/°C$).

In conclusion, the stress in the substrate of a thin film/substrate structure may arise from: the difference of the thermal expansion coefficients of substrate and thin film, which induces a stress in the order of $10^{7}dyn/cm^{2}$ and linearly distributed along the thickness of the substrate; another component of stress is due to the discontinuity of the thin films, which is found to be centralized at the region near the edge of thin films, where the stress is about the same order of the stress in the thin film, *i.e.*, in the order of $10^{9}dyn/cm^{2}$. In the case of a wafer diffused with impurity atoms, the difference of atomic radii of substrate and doped atoms contributes to the stress in such structure, which will be discussed in more detail in next section.

5.3 Diffusion-Related Stress in Silicon Wafer

Impurity diffusion is one of the essential process steps for silicon devices. Stress will be introduced into silicon wafer during diffusion process. When the induced stress exceeds the critical yield stress of silicon at diffusion temperature, dislocations and other crystal defects will be introduced into the silicon wafer. In this section, photoelasticity are applied to determine the stress distribution in the wafers after a typical diffusion process of fabricating high power diodes. The stress-relief model is applied to account for the stress relief during diffusion. The stress superposition principle is used to explain the stress state after the double-side diffusion.

5.3.1 Single-Side Diffusion and Stress-Relief Model

Impurity phosphorus is doped into one side of p-type (111) oriented silicon wafer of thickness $400\mu m$ and resistivity about $5\Omega cm$. The diffusion is accomplished by a two-step

process consisting of a prediffusion and a drive-in cycle. The prediffusion is carried out at 1180°C for 14 hours, redistribution is made at 1270°C for 100 hours. The stress distribution in the undoped substrate is examined by the Senarmont compensation method or the Fourier analysis method. The orientation of the sample being measured and the result of stress distribution are shown in Figure 5.14. It is found from the experimental result that, in the case of single-side diffusion, the normal stress σ_{zz} equals zero, and the normal stress σ_{yy} linearly distributes across the thickness of wafer, as shown in Figure 5.14(b). In the undoped region of the wafer, there is a compression stress region in its upper part near the interface, and there is a tensile stress region in its lower part. The compressive stress reaches its maximum σ_{cmax} ($-5\times10^7 dyn/cm^2$) at the boundary of diffused layer and undoped region, and the tensile stress reaches its maximum σ_{tmax} ($2\times10^7 dyn/cm^2$) at the backside of the wafer.

The stress state in the silicon wafer mainly depends on the diameter of the impurity atoms, as well as their distribution. During prediffusion, the maximum phosphorus atom concentration can reach $1.3\times10^{21} cm^{-3}$ at 1180°C. After redistribution, the phosphorus atom concentration at wafer surface is about $2.3\times10^{20} cm^{-3}$, and a p-n junction forms at about $90\mu m$ from the wafer surface. Since the radius of phosphorus atom (1.10Å) is less than that of silicon atom (1.17Å), the doped phosphorus tends to cause the crystal lattice contract and results in compressive stress in the silicon substrate region near the diffused layer. The compressive stress causes the silicon wafer to curve towards the diffused layer. As a result, there exists tensile stress in the opposite region of the silicon substrate. Hence, the stress in the undoped region can be expressed by a linear approximation:

$$\sigma_{yy}(z) = \sigma_{t\max} + (\sigma_{c\max} - \sigma_{t\max})(z-h)/h \tag{5.28}$$

To satisfy the condition of static force balance, the integral of the stress normal $\sigma_{yy}(z)$ along z axis from one surface of the wafer to the another should be zero, that is

$$\int_0^{d+h} \sigma_{yy}(z)dz = 0 \tag{5.29}$$

where, d is the thickness of diffusion doped layer. Eq.(5.29) can be rewritten as

$$\int_0^h \sigma_{yy}(z)dz = \int_d^h \sigma_{yy}(z)dz \tag{5.30}$$

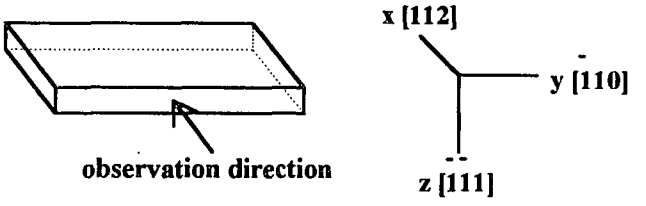

(a)

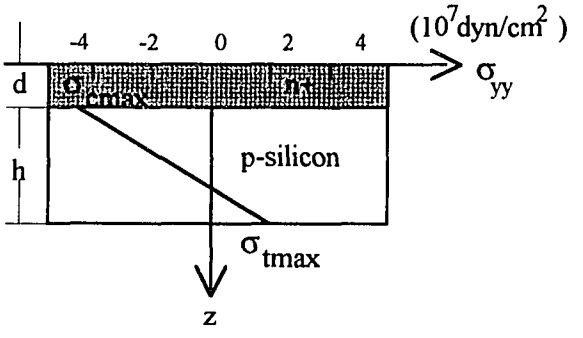

(b)

Figure 5.14 Stress variation across the thickness for a single-side diffusion wafer.

which indicates that the integral of the stress for the diffused layer is equal to that for the undoped layer. Therefore, although the stress distribution in the diffused layer may not be directly measured by using the photoelasticity method, the stress integral for the diffused layer can be estimated by using (5.30). By substituting Eq.(5.28) into Eq.(5.30) and using d=90μm and h=310μm, the stress integral for both the diffused layer and the undoped substrate is calculated as 4.6×10^5 *dyn/cm*.

On the other hand, based on the relationship of the stress σ and the impurity concentration N_i in the elastic region [59], we have

$$\sigma = \frac{E}{1-\nu}\beta N_i \tag{5.31}$$

where E is Young's modulus and ν is Poisson's ratio of the doped layer, β is the lattice strain coefficient expressed as

$$\beta = (1/3)[1-(R_I / R_{Si})^3]N^{-1}\gamma \tag{5.32}$$

where R_I and R_{Si} are atomic radii of the impurity and silicon, respectively, N is the atomic concentration of the silicon crystal ($5\times10^{22} cm^{-3}$), and γ is *the lattice packing factor*, (for silicon, γ=0.34). Eq.(5.31) indicates that the stress distribution has the same profile as the phosphorus impurity distribution. After redistribution diffusion, the phosphorus impurity distribution $N_I(z)$ is described by a Gaussian distribution [60]:

$$N_I(z)=N_S exp\text{-}[z^2/(4Dt)] \tag{5.33}$$

where N_s is the surface concentration ($2.3\times10^{20} cm^{-3}$), D the diffusion coefficient (3×10^{-12} cm^2/s), and t the time after initiation of diffusion (t=100 hours). From (5.30)~(5.33), the integral of stress along the thickness of the diffused layer is calculated as 2.4×10^6 *dyn/cm*.

By comparing the stress integral with photoelasticity experiment, $4.6\times10^5 dyn/cm$, with that obtained from the elastic model, $2.4\times10^6 dyn/cm$, it is found that the latter is about five times greater than the former. The discrepancy is believed to arise from the stress relief during diffusion process. The stress developed by the lattice concentration due to the introduction of impurity atoms is sufficient to cause plastic deformation and thus generate dislocations. The mechanism of stress relief due to the generation of dislocations has been proved by the dislocation arrays observed in the diffused layer with the etch-pit evaluation technique [61]. Therefore, in the case of single-side diffusion, there is a plastic region of diffused layer and a elastic region of undoped substrate. Similar to the analysis made by S. Prussin [62], by taking the stress relief in the diffused region into account, the stress distribution along the thickness of the wafer is expressed as (also see Figure 5.15)

$$\sigma_{yy}(z) = \sigma_M \qquad o<z<a$$

$$\sigma_{yy}(z) = \frac{E}{1-\nu}\beta N_I(z) \qquad a<z<b \tag{5.34}$$

where σ_M is the threshold stress necessary to generate dislocations at the diffusion temperature, $9\times10^7 dyn/cm^2$. Based on (5.34), we recalculate the integral of stress $\sigma_{yy}(z)$ in the diffused layer along the z direction from point o to point b, as $4.6\times10^5 dyn/cm$. By intersecting the stress profiles of the two equations (5.34), we have $a\approx50\mu m$, which is about half of the diffusion junction depth, $90\mu m$. Furthermore, we may predict that during the whole diffusion process, about 80 percent of the stress caused by lattice contraction due to phosphorus diffusion has been released. If no stress is released during the diffusion process, the difference of the results from photoelasticity experiment and from the elastic model should be insignificantly small. Therefore, by comparing the measurement result by using the photoelasticity method with the calculated result based on the elastic model, we can reveal the degree of stress relief during the diffusion process.

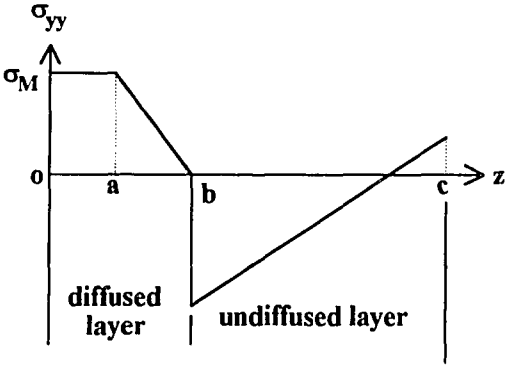

Figure 5.15 Distribution of stress across the wafer.

5.3.2 Double-Side Diffusion and Stress Superposition

Double-side diffusion is accomplished under conditions similar to that used in single-side diffusion. The stress state in the undoped region of silicon wafer after double-side diffusion is measured by the Senarmont compensation method or the Fourier analysis method. It is found that there is a uniform compression stress of about $3\times10^7 dyn/cm^2$ in

the undoped region. No wafer curvature is observed in such case. The uniform stress phenomenon attributes to the approximately linear and symmetrical distribution of stress along the thickness of the sample. If both surfaces of the wafer sample are doped with phosphorus atoms simultaneously under the same conditions, the stress superposition principle will be satisfied. The total stress introduced in the undiffused region of the wafer after a double-side diffusion is the sum of the stress due to the upper doped layer and the stress due to the lower doped layer:

$$\begin{aligned}\sigma_{\text{total}} &= \sigma_{t\max} + (\sigma_{c\max} - \sigma_{t\max})(y-h)/h \\ &\quad + \sigma_{c\max} + (\sigma_{t\max} - \sigma_{c\max})(y-h)/h \\ &= \sigma_{t\max} + \sigma_{c\max} \end{aligned} \tag{5.35}$$

where $\sigma_{t\max}$ and $\sigma_{c\max}$ are the maximum tensile stress and the maximum compressive stress measured in the single-side diffusion case. Eq.(5.35) denotes that the stress in the undoped region of the silicon wafer after double-side diffusion is equal everywhere, whose value is equal to the algebraic sum of the stresses $\sigma_{t\max}$ and $\sigma_{c\max}$, (note that $\sigma_{c\max}<0$ and $\sigma_{t\max}>0$). In this experiment, $|\sigma_{c\max}|>|\sigma_{t\max}|$ indicates that the total stress introduced in double-side diffusion is compressive. Since there is no wafer curvature in a double-side diffusion wafer, it is impossible to determine the stress by measuring curvature radius of the wafer with *X*-ray diffraction or other optical methods. However, photoelasticity method does not measure the curvature radius, and hence exhibits its uniqueness in measuring uncurved wafers.

5.4 Summary

In this chapter, we apply photoelasticity principles and methods to investigate the stress in some microelectronic materials and device structures. Depending on different cases, we employ different measurement schemes and arrangements. For the synthetic diamond substrate, there was sufficient thickness to enable to make an observation normal to the

sample surface. In the cases of thin film/substrate structures and diffused wafers, the limited thickness of the sample prevents us from probing along the normal direction of sample surface. Alternatively, we make observations from flank sides. Since, as shown in the above examples, we are often involved with measuring a fractional order of isochromatic line, suitable compensation methods are needed to determine the photoelastic parameters. We illustrate the application of the intensity analysis method, the Senarmont compensation method and the Fourier analysis method. The shearing stress difference method is used to separate the two principal stresses in synthetic diamond substrate, and obtain the principal stress distribution along any cross section of the sample.

From the illustration above, the stress state in various microelectronic materials and device structures can be quantitatively analyzed by using photoelasticity. This technique provides a high sensitivity of detecting stress. For an 8-bit *CCD* camera presently employed, the minimum detectable stress may be $10^8 dyn/cm^2$. It also provides a high spatial resolution. If the optical parts and the detection system are properly chosen, the spatial resolution may approach the diffraction limit, which is in the order of the wavelength of the light source used.

CHAPTER 6

CONCLUDING REMARKS

In this chapter we summarize the research results that have been presented in this dissertation and discuss some open issues that may serve as the basis for our future research.

6.1 Summary of Research Results

Stress is an important issue in microelectronics. The photoelastic technique is an effective method of characterizing the stress. However, there are some difficulties in applying this technique to microelectronic materials. The solutions to these problems will undoubtedly benefit the effective application of this technique in characterizing the stress, and moreover, will produce a better understanding of and control on stress in microelectronic materials and devices. This dissertation is focused on finding solutions to these problems. In brief, our research projects include following issues:

1) In order to apply the photoelastic principle to measure the stress in crystals, it is essential for us to develop the stress-optic law for crystals, which are always photoelastically anisotropic. Based on the principle of crystal optics, the anisotropic property of photoelasticity for cubic crystals is studied in detail. The matrix forms of the piezo-optic coefficient tensors for arbitrary crystallographic directions and probing directions are derived in light of the fourth-rank tensor transformation law. The relationship between the principal axes of the stress ellipsoid and the principal axes of the refractive index ellipsoid for general circumstances, for arbitrary crystallographic directions and radiation direction is investigated. Finally, suitable forms of the stress-optic law for anisotropic materials are derived in some commonly used coordinate

configurations. The investigation lays a theoretical basis for photoelastic stress analysis of crystal materials.

2) In order to apply the stress-optic law to solve for principal stresses, it is needed to determine the photoelastic parameters, that is, the birefringence phase difference and the birefringence angle. The second important issue in this dissertation is to develop effective methods to determine the photoelastic parameters, which corresponds to the fractional order fringes of photoelastic patterns. The Senarmont compensation is a useful method of determining the birefringence phase difference with fractional order of isochromatic line. However, with this point-by-point method, we only measure one point of the sample at a time. To improve measurement efficiency, we successfully apply the intensity analysis method we developed to measure the whole area of the sample at one time. The Fourier analysis is another method we developed to measure birefringence phase difference. The approach is to use a continuously rotating analyzer followed by Fourier analysis of the measured emerging light intensity to determine photoelastic parameters. The results obtained experimentally illustrate that the Fourier analysis method has a better immunity to random noise and a better sensitivity (the minimum detectable stress is about $1.8\times 10^7 dyn/cm^2$, for a silicon sample with thickness of $500\mu m$) than the intensity analysis method ($7.6\times10^7 dyn/cm^2$). With advanced solid-state image sensing and image processing techniques, there is hope for this method to become a powerful means to perform automatic analysis of stress for various microelectronic materials and device structures. In this dissertation, we also presented the three-direction observation method to determine the directions of principal stresses from the information of secondary principal stresses. The application of this method, for the first time, reveals the relationship between the orientation of the principal stress and the symmetry of crystal structure.

3) A photoelastic measurement system is established, which basically consists of a light source, a polarizer, an analyzer, a quarter waveplate, and a detector. The system can perform qualitative observations of photoelastic patterns and quantitative measurement of

stress distributions. With the software we developed, the system can automatically execute data acquisition, image processing, data analysis and stress calculation. Experimental results illustrate the system's capability of measuring the stress state in a microelectronic material with a high accuracy. The establishment of the system provides us an effective means of studying stress in microelectronic materials with photoelasticity.

4) Photoelastic techniques are applied in studying the stress state in microelectronic materials. Projects include studying the stress distribution in a diamond substrate, studying stress in thin film/substrate structures, and studying diffusion-related stress in silicon wafers. In the first project, the residual stress in a synthetic diamond substrate is analyzed by using the automatic data acquisition and analysis system. The digital image processing techniques are applied to improve the quality of the sensed images, to reduce noise and to determine the boundary of the measured samples. Photoelasticity is used to determine the photoelastic parameters, and shearing stress difference method is applied to calculate the two-dimensional stress distribution in the sample. In the second project, we present the application of photoelastic techniques in measuring film-induced stress of substrate/thin film structures. The Fourier analysis method and the Senarmont compensation method are applied to investigate the stress induced by different mechanisms, including stress induced by a single layer of oxide film, stress induced by edge-force in a groove structure, and stress of multi-layer structures. For each case, a stress model is built and theoretical results are compared to those of photoelastic measurement. In the third project, the Senarmont compensation method is applied to decide the fractional fringe order of isochromatic lines and to determine the stress distribution in silicon wafers after various diffusion processes. The stress in diffused layer is estimated based on the stress data measured for the undoped region. A modified stress model is developed to account for the stress relief during diffusion process in the diffused layer.

In summary, this dissertation presents a systematic study of photoelastic stress analysis in microelectronic materials, ranging from theoretic research, method exploration,

system establishment, and practical application. We extend the stress-optic law from isotropic medium to photoelastically anisotropic materials, and derive the matrix forms of piezo-optic coefficient tensor in two commonly used coordinate systems. Based on photoelastic principal, we build up a photoelastic measurement system which can be used to qualitatively observe the photoelastic pattern and quantitatively measure the stress distribution. To apply the photoelastic method to solve the stress problems in microelectronic materials, we develop a series of effective methods of determining the fractional order of isochromatic lines of photoelastic patterns, determining the principal directions, and calculating the stress distribution of a sample. The experiment and measurement in microelectronic materials show that photoelastic technique has the advantages of having high spatial resolution and high sensitivity, and being automatic and in real-time. There is hope for its application as an on-site monitoring tool in microelectronic industry.

6.2 Directions for Future Research

In this dissertation we have illustrated some applications of photoelasticity method in measuring the stress of microelectronic materials and device structures. It would be very interesting to try to extend this technique to characterize the crystal defects of microelectronic materials. Furthermore, it would also be extremely interesting and useful to apply photoelastic effect in device physics. Through controlling the stress in certain region of a device, we may trim the characteristic of the device.

A very important task in effectively applying the Fourier analysis method we developed is the improvement of the detection system. The approach is to employ a high performance *CCD* sensor (16-bit dynamic range) as detector. A thermoelectrically cooled system is used to provided a low operation temperature of 77°C, to reduce the readout noise and the dark charge noise. As discussed in Chapter 3, such a high dynamic range

allows us to measure a minimum birefringence phase difference of about 5°, which corresponds to a stress of 2.0×10^7 dyn/cm^2 for sample thickness 500μm, or 5.0×10^6 dyn/cm^2 for a silicon sample of thickness $2mm$.

When it is required to measure the stress state of the whole wafer at a time, a simultaneous coverage of the entire sample is needed, at the expense of reducing spatial resolution. If the format of *CCD* array is of 1024×1024, the spatial resolution of the measurement is $150\mu m$ for a 6-inch wafer, and $2\mu m$ or diffraction limit for a sample of $2mm$ dimensions. Another problem in realizing real-time characterization is the speed limitation while transforming and analyzing the photoelastic pattern images. For example, if we need to obtain the measurement result in 10 minutes, it is required to transfer 180 images in about 8 minutes, with 2 minutes to process these images and calculate the stress distribution. Therefore, high speed *CCD* image sensor, high speed readout circuits, high speed *A/D* converter, high speed *I/O* circuit, and high speed computer are essential to realize the purpose. In addition, we must consider the storage capacity of the computer. If we employ a *CCD* sensor of 8 bits and 164×192 pixels, only $32K$ byte storage space is required to store one frame of such image. For 180 frames of such image, the required storage space is about $5.8M$ bytes. It needs $0.5M$ bytes to store an image of 16 bits and 512×512 pixels. Therefore, a total $90M$ byte storage space is required to store 180 frames of such image.

Photoelasticity has been proved to be an effective, non-destructive method to measure the stress in microelectronic materials and device structures. One possible extension of the application is to inspect the crystal defects of a wafer, since the defects in microelectronic materials introduce stress field around the defects. The most commonly used technique for defect characterization in semiconductor materials is *X*-ray topography. However, the relatively long time necessary to characterize a sample by this technique precludes testing of individual samples in a given batch. The photoelastic method is non-destructive, fast and, hence, can permit testing of each wafer in a given batch. As an

example, we discuss the feasibility of measuring an individual dislocation in crystal by using photoelastic method. For edge dislocation, the stress field near the dislocation line is given by [63]:

$$\sigma_{rr} = \sigma_{\theta\theta} = \frac{\mu b}{2\pi(1-\nu)} \frac{\sin\theta}{r}$$

$$\sigma_{r\theta} = -\frac{\mu b}{2\pi(1-\nu)} \frac{\cos\theta}{r} \qquad (6.1)$$

where μ is the shear modulus ($\sim 4\times10^{11} dyn/cm^2$), b is the magnitude of Burgers vector ($\sim 2.5\times10^{-8}$ *cm*), ν is the Poisson's ratio (0.31 for GaAs). Thus, we can calculate the stresses at $1\mu m$ from the dislocation line:

$$\sigma_{rr} = 2.7\times10^{7}\sin\theta \; dyn/cm^2$$

$$\sigma_{r\theta} = 2.7\times10^{7}\cos\theta \; dyn/cm^2 \qquad (6.2)$$

At $10\mu m$ from the dislocation line, the stress reduces to about $2\times10^{6} dyn/cm^2$. Therefore, from the discussion of Chapter 3, it is evident that when the dynamic range of the detection system is 16 bits, it is possible to detect the photoelastic patterns induced by the stress field of the edge dislocations. The approach is first to investigate the photoelastic patterns of stress field for two types of wafer plane orientations [(111) or (100)], for various dislocations (edge dislocation, screw dislocation, and mixed dislocation), for different dislocation directions and Burgers vector orientations. Then, the experimentally observed images on the samples are analyzed with the image recognition technique, and the properties of various dislocations can be abstracted.

Another possible extension of the application of photoelasticity is to improve the device performance by controlling the stress of the device structure. Usually, the stress field in a device affects the performance of the device in an indirect manner. Under certain circumstances, the stress in a device will directly change its performance. For example, in the case of index-guide laser, the stress induced during the fabrication produces a significant waveguide effect. The stress field in the active layer induces a refractive index

change in the plane of the active layer through the photoelastic effect. The dielectric permittivity deformations in the active layer of the laser could be responsible for anomalous emission patterns because modified waveguiding conditions could be present in the laser cavity. The investigation of such a relationship between the stress state and the performance of a device is a very interesting and challenging issue. The significance of such a project is that we may trim the characteristic of a device by controlling the stress in the device. Therefore, we may open a new field of study, *stress engineering*, in microelectronics. It is one of the major objectives of our research activity in the future.

REFERENCES

[1] Peter Singer, "Film Stress and How to Measure It", *Semiconductor International* October (1992): 54-58.

[2] Romain Maciejko, Jan M. Glinski, A. Champagne, Jean Berger, and Luc Samson, "Photoelastic Effects on the Emission Patterns of InGaAsP Ridge-Waveguide Lasers", *IEEE J. Quantum Electronics* **25** (1989): 651-660 .

[3] Naotake Toyama, "Stress Effect in Au-Si Schottky Diode Doped with Cu", *J. Appl. Phys.* **55** (1984): 4398-4403.

[4] David A. Faux, "The Fourier Series Method for the Calculation of Strain Relaxation in Strain-Layer Structure", *J. Appl. Phys.* **75** (1994): 186-192.

[5] Carroll F. Powell, Joseph H. Oxley, and John M. Blocher, *Vapor Deposition*, John Wiley & Sons, New York (1966).

[6] B. G. Cohen and M. W. Focht, "X-Ray Measurement of Elastic Strain and Annealing in Semiconductors", *Solid State Electron.* **13** (1970): 105-112.

[7] W. H. Zachariasen, *Theory of X-ray Diffraction in Crystals*, John Wiley & Sons, New York (1944).

[8] F. J. von Preissig, "Applicability of the Classical Curvature-Stress Relation for Thin Films on Plate Substrates", *J. Appl. Phys.* **66** (1989):4262-4268.

[9] Chaorong Li, Zhenhong Mai, Shufan Cui, Junmin Zhou, and Aiju Ding, "Determination of Stress in GaAs/Si Material", *J. Appl. Phys.* **66** (1989): 4767-4769.

[10] Albrecht Kuske and George Robertson, *Photoelastic Stress Analysis*, John Wiley & Sons, New York (1974).

[11] W. L. Bond and J. Andrus, "Photographs of the Stress Field Around Edge Dislocations", *Phys. Rev.* **101** (1956): 1211.

[12] J. Hornstra and P. Penning, "Birefringence Due to Residual Stress in Silicon", *Philips Res. Repts.* **14** (1959): 237-249.

[13] R. O. DeNicola and R. N. Tauber, "Effect of Growth Parameters on the Residual Stress and Dislocation Density of Czochralski-Grown Silicon Crystal", *J. Appl. Phys.* **42** (1971): 4262-4270.

[14] Shin Takasu, *et al.*, in "*Semiconductor Silicon 1977*", The Electrochem. Soc. Inc., Princeton (1977).

[15] H. Kotake and Shin Takasu, "Quantitative Measurement of Stress in Silicon by Photoelasticity and Its Application", *J. Electrochem. Soc.* **127** (1980): 179-184.

[16] T. Iwaki and T. Koizumi, "Stress-Optic Law in a Single Crystal and Its Application to Photo-Anisotropic Elasticity", *Experimental Mechanics* **29** (September 1989): 295-299.

[17] Albert Feldman and Roy M. Waxler, "Dispersion of the Piezobirefringence of GaAs due to Strain-Dependent Lattice Effects", *J. Appl. Phys.* **53** (1982): 1477-1483.

[18] Aloke K. Dutta, Pratul K. Ajmera, and Burke Huner, "Piezobirefringence Effect in GaAs Disk Subjected to Diametrical Compression", *J. Appl. Phys.* **65** (1989): 5230-5232.

[19] Sadao Adachi and Kunishige Oe, "Internal Strain and Photoelastic Effects in $Ga_{1-x}Al_xAs/GaAs$ and $In_{1-x}Ga_xAs_yP_{1-y}/InP$ Crystals", *J. Appl. Phys.* **54** (1983): 6620-6627.

[20] Hancheng Liang, Ganming Qin, and Shounan Zhao, "An Automatic System for Measuring Stresses in Silicon Crystals", *Chin. J. Scientific Instrument* **10** (1989): 147-150.

[21] Shounan Zhao, Hancheng Liang, Ganming Qin, and Lan Huang, "The Measurement and Study of Stress in Silicon Single Crystal and Wafer with Photoelasticity", *Proceedings of the International Conference of Materials and Process Characterization for VLSI*, Scientific World, Singapore (1988):103-105.

[22] Hancheng Liang, Shounan Zhao, and Honghui Yin, "Effect of Thermal Treatment on Stress States of Silicon Crystals", *J. South China Institute of Technology* **14** (1986): 101-106.

[23] Jiang Liansheng, Zhao Shounan, and Hancheng Liang, "Study and Measurement of Stresses in Ion-Implanted Si Crystals by Means of IR Photoelasticity", *Chin. J. Infrared & Millimeter Waves* **9** (1990): 425-429.

[24] L. D. Landau, E. M. Lifshitz, and L. P. Pitaevskii, *Electrodynamics of Continuous Media*, 2nd ed., Pergamon Press, New York (1981).

[25] J. F. Nye, *Physical Properties of Crystals*, Oxford University Press, Oxford (1960).

[26] C.W. Higginbotham, Manuel Cardona, and F. H. Pollak, "Intrinsic Oiezobirefringence of Ge, Si, and GaAs", *Phys. Rev.* **184** (1969):821-829.

[27] A. Feldman, R. M. Waxler, and D. Horowitz, "Photoelastic Constants of Germanium", *J. Appl. Phys.* **49** (1978): 2589-2590.

[28] A. Feldman and D. Horowitz, "Dispersion of the Piezobirefringence of GaAs", *J. Appl. Phys.* **39** (1968): 5597-5599.

[29] American Institute of Physics, *American Institute of Physics Handbook*, 3rd ed., McGraw-Hill Book Company, NewYork (1972).

[30] A. E. H. Love, *Mathematical Theory of Elasticity*, 4th ed., Cambridge (1927).

[31] T. Iwaki and T. Koizumi, "Stress-Optic Law in a Single Crystal and Its Application to Photo-Anisotropic Elasticity", *Exp. Mech.* **29** (September 1989): 295-299.

[32] R. B. Heywood, *Photoelasticity for Designers*, Pergamon Press, New York (1969).

[33] Zhao Shounan, Huang Lan, Huang Xiaohong, Hancheng Liang, and Jiang Liansheng, "Characterizing Stress for Device Process with Infrared Photoelasticity", *The Proceedings of the Second International Conference on Solid State and Integrated Circuit Technology*, International Academic Publishers, Beijing (1989):84-86.

[34] Jiang Liansheng, Zhao Shounan, and Hancheng Liang, "Measurement and Study of Stress in Ion-Implanted Silicon Wafer by Infrared Photoelastic Method", *Chin. J. Infrared and Millimeter Waves* **9** (1990): 425-429.

[35] A. Gerrard and J. M. Burch, *Introduction to Matrix Methods in Optics*, John Wiley & Sons, London (1975).

[36] M. Born and E. Wolf, *Principles of Optics*, Pergamon, Oxford (1980).

[37] A. Papoulis, *The Fourier Integral and its Applications*, McGraw-Hill, New York (1962).

[38] G. Robertson, "An Intensity Method for Photoelastic Birefringence Measurement", *Brit. J. Appl. Phys.* **16** (1965): 207-218.

[39] M. M. Frocht, *Photoelasticity*, Vol.1, John Wiley & Sons, New York (1941).

[40] Amnon Yariv, *Optical Electronics*, California Institute of Technology (1985).

[41] K. R. Barnes, *The Optical Transfer Function*, American Elsevier Publishing Company, New York (1971).

[42] Francis W. Sears, *Optics*, 3rd Ed., Addison-Wesley Publishing Company, Massachusetts (1958).

[43] J. F. Nye, *Physical Properties of Crystals*, Oxford University Press, Oxford (1960).

[44] Bela A. Lengyel, *Laser*, 2nd ed., Wiley-Interscience, New York (1971).

[45] D. W. Tenquist, R. M. Whittle, and J. Yarwood, *University Optics*, Vol. 2, Iliffe Book, London (1970).

[46] Francis A. Jenkins and Harvey E. White, *Fundamentals of Optics*, 3rd ed., McGraw-Hill Book Company, New York (1957).

[47] Leo Levi, *Applied Optics*, Vol. 2, John Wiley & Sons, New York (1980).

[48] David F. Barbe, "Imaging Devices using the Charge-Coupled Concept", *Proceedings of the IEEE* **63** (1975):38-67.

[49] F. J. von Preissig, "Applicability of the Classical Curvature-Stress Relation for Thin Films on Plate Substrate", *J. Appl. Phys.* **66** (1989):4262-4268.

[50] H. Windischmann and K.J. Gray, "Stress Measurement of *CVD* Diamond Films", *Diamond and Related Materials*, **4** (1995):837-842.

[51] K. H. Chen, Y. L. Lai, J. C. Lin, K. J. Song, L. C. Chen, and C. Y. Huang, "Micro-Raman for Diamond Film Stress Analysis", *Diamond and Related Materials*, **4** (1995):460-463.

[52] R. C. Gonzalez and R. E. Woods, *Digital Image Processing*, Addison-Wesley Publishing Company, New York (1992).

[53] R. J. Jaccodine and W.A.Schlegel, "Measurement of Stress at Si-SiO_2 Interface", *J. Appl. Phys.* **37** (1966): 2429-2434.

[54] Ganming Qin, Hancheng Liang, and Zhao Shounan, "Measurement of Stresses in Silicon Wafer with Infrared Photoelastic Method", *Chin. J. Infrared and Millimeter Waves* **7** (1988): 109-112.

[55] Hiroshi Yamada-Kaneta, and Kunihiko Wada, "Elastic Calculation of the Thermal Strains and Stresses of Multilayer Plate", *J. Appl. Phys.* **62** (1987): 62-74.

[56] S. M. Hu, "Film-Edge-Induced Stress in Silicon Substrate", *Appl. Phys. Lett.* **32**(1978): 5-7.

[57] S. P. Timoshenko and J. N. Goodier, *Theory of Elasticity*, 2nd. ed., McGraw-Hill, New York (1970).

[58] S. M. Hu, "Film-Edge-Induced Stress in Substrates", *J. Appl. Phys.* **50** (1979): 4661-4666.

[59] Adel S. Saada, *Elasticity: Theory and Application*, Robert E. Krieger Publishing Company, Malabar, Florida (1983).

[60] J. Crank, *The Mathematics of Diffusion*, Oxford University Press, London (1957).

[61] J. M. Fairfield and G. H. Schwuttke, "Strain Effects Around Planar Diffused Structures", *J. Electrochem. Soc.* **115** (1968): 415-422 .

[62] S. Prussin, "Generation and Distribution of Dislocations by Solute Diffusion", *J. Appl. Phys.* **32** (1961): 1876-1881.

[63] W. T. Read, *Dislocations in Crystals*, McGraw-Hill Book Co., New York (1953).